DISSERTATION

Quantum Field Machines with Cold Atoms

ausgeführt zum Zwecke der Erlangung des akademischen Grades eines Doktors der
technischen Wissenschaften

unter der Leitung von
Univ. Prof. Dipl.-Ing. Dr. techn. Hannes-Jörg Schmiedmayer
E141 Atominstitut

eingereicht an der
Technischen Universität Wien
Fakultät für Physik von

João David Ventura Sabino
Matrikelnr. 11731410

Wien, xx October 2022

J. Sabino

Gutachter:

H.-J. Schmiedmayer

Hans-Christoph Näger

Selim Jochim

Nunca se sabe que abraço será o último.

Acknowledgements

I would like to start by thanking my supervisors Prof. Jörg Scmiedmayer and Prof. Yasser Omar for the opportunity of working on an exciting subject with all the means necessary for it. I would also like to acknowledge the institutions that hosted me during my PhD: the Atominstitut, as part of TUWien (in Vienna); and the Physics of Information and Quantum Technologies group, at the Portuguese Quantum Institut (PQI) and CeFEMA, at Instituto Superior Técnico.

A very special thanks to the team that worked with me all these five years. Starting with the previous PhD students, Bernhard Rauer and Thomas Schweigler, for all the very useful insights, tips and discussions (an extra thank you to Thomas, for all the climbing and mountaineering adventures, I know the beauty of Austria thanks to you). My friends and colleagues, Frederick, always available for productive discussions, beers and football. Federica Cataldini for all the support, hours spent in the lab and pictures that generated gossip. SiCong, a post-doc that revealed to me many secrets about the experiment. And Amin (or Aritza kazi), with whom I gladly worked closely and spent a lot of time in the lab, on discussions and having fun. Had my PhD been a war, you would have been the captain in my team. More recently, Philipp, a fast learner and a partner for dark jokes. On the theory side, thank you Sebastian for all the interesting discussions (mainly physics and linux related) and for reading my thesis countless times. Still on the theory team, many thanks to Igor for helping me with math, physics and peculiar world views. I hope to talk to you again, if nothing happens.

Thanks to Andreas for being a helpful and peaceful office mate. Wherever you are, I hope someone hugs you a lot. Thanks to Filippo who is a power house of energy and has the ability of annoying and making you laugh with the same sentence. I'm also greatful I met Camille, I had nice discussions with you, amazing hikes and leraned that there's salvation for chemists. I have to thank Pradyumna as well, for all the fun times inside and outside ATI. I've never known such a kind prince. I should also mention the Lithium team (RuGway, Chen, Qi and Pra) who were always eager to help and are an example of resilience. A big high (not to high. . .) five to Tiantian for being a partner to share our PhD frustrations. To Kjeld, a big thank you for the nice memories created in Vienna. A "viva!" to Wenzel and Nico for being living proof that Autrians can be nice and fun (ah!). Thanks Max for the interesting discussions.

A hug to my friend Andrew. You destroyed my futures savings. On the other hand I will have great watches and fountain pen collections. Thanks for your positivity and genuineness. Sometimes you speak with gestures, it is very beautiful to see they say as much, maybe even more, than words. A kind word to Benedikt for keeping me in touch with music, even with a pandemic in the middle.

Thanks Fritz for all the climbing adventures, jam sessions and diverse conversations and dumb jokes that kept us sane in a very surprising world. Also, thanks for showing me that we don't need to be special to do great things.

Last but not the least, my family. My parents for the constant loving support and cheering in the bad days. My brother for showing me that no matter what you do, you can enjoy life. And my girlfriend, for having my back, for her sweetness and patience. You definitely make me a better man.

Por fim, agradecer ao meu avô, que me fez ver que a preserverança é um bom caminho para o sucesso, que a tradição se pode conciliar com o progresso e que a idade não está no corpo, mas no espírito.

Abstract

This thesis dives into the topic of quantum thermodynamics by exploring the new concept of Quantum Field Machine, a device designed to perform a task in the quantum realm. Such device requires quantum mechanics for its full description, while, at the same time, it is unfeasible to account for each and every degree of freedom, making statistical considerations crucial to describe its behaviour. These two requirements make it a genuine quantum heat engine operating at the intersection of thermodynamics and quantum mechanics. In the context of this work, a QFM is an ultra-cold atomic system consisting of three components. The main task of this machine is to cool down one of its components, using two basic operations (primitives), which have an equivalent counterpart in classical thermodynamics: The first operation is compression or expansion of one of the components (corresponding to a piston); the second operation consists of coupling pairs of components for energy exchange (resembling a valve). In this work, we carry out a numerical study of each primitive as well as several refrigeration cycles performed with the machine. We also demonstrate the experimental proof-of-concept implementation of each primitive. To that purpose, we use one dimensional Bose-Einstein condensates generated in the Atomchip platform. Furthermore, we look in detail at the consequences of driving two uncorrelated components of the machine in the strong coupling regime, where interesting phenomena, such as an anomalous flow of heat, can be observed. This work paves the way to further studies in quantum thermodynamics and provides tools for studying thermodynamics with quantum, finite systems, far from the usually assumed thermodynamic limit.

Resumo

Esta tese leva a cabo estudos no campo da termodinâmica quântica, propondo o conceito novo de Máquina de Campo Quântico, desenhada para executar tarefas específicas no domínio quântico. Para descrever completamente o comportamento desta máquina, são necessários conceitos de mecânica quântica e, ao mesmo tempo, ferramentas de física estatística, uma vez que não é viável descrever cada grau de liberdade do sistema individualmente. Tais requerimentos fazem da Máquina de Campo Quântico uma genuina máquina térmica quântica que opera na intersecção da mecânica quântica e da termodinâmica. No contexto deste trabalho, a Máquina de Campo Quântico é um sistema de átomos frios constituído por três componentes. O propósito da MCQ é arrefecer uma destas componentes, usando duas operações básicas (designadas de primitivas) que encontram equivalência na termodinâmica clássica: A primeira operação é a compressão/expansão de uma das componentes (assemelhando-se a um pistão); a segunda operação consiste em acoplar um par de componentes para transferência de energia (assemelhando-se a uma válvula). Neste trabalho, estudamos numericamente cada primitiva, bem como vários ciclos de arrefecimento, resultantes da operação da máquina. Também demonstramos a implementação experimental da prova-de-conceito de cada primitiva. Para isso, usamos condensados de Bose-Einstein unidimensionais gerados na plataforma Atomchip. Além disso, avaliamos ainda as consequências de migrar duas componentes independentes para o regime de acoplamento forte, onde fenómenos como fluxo de calor anómalo podem ser observados. Este trabalho abre caminho para futuras investigações em termodinâmica quântica e oferece ferramentas para estudar termodinâmica com sistemas quânticos e finitos, fora do usual limite termodinâmico.

Zusammenfassung

Diese Dissertation behandelt das Thema der Quanten-Thermodynamik. Sie widmet sich der Erforschung des neuen Konzepts der Quantenfeldmaschine (QFM), ein Apparat zur Verrichtung von Arbeit im Quantenregime. So ein Apparat benötigt für seine vollständige Beschreibung einerseits die Gesetze der Quantenmechanik, andererseits ist es aufgrund der schieren Anzahl unmöglich jeden seiner Freiheitsgrade zu berücksichtigen, eine Tatsache die statistische Methoden für die Modellierung des Verhaltens unabdinglich macht. Diese beiden Vorraussetzungen führen dazu, dass es sich dabei um eine wahrhaftige Quanten-Wärmekraftmaschine handelt, die am Schnittpunkt von Thermodynamik und Quantenmechanik arbeitet.

Im Kontext dieser Arbeit besteht die QFM aus einer ultrakalten Atomwolke, die in drei Bestandteile gegliedert ist, wobei sie zum Ziel hat einen davon zu kühlen. Dafür stehen zwei grundlegende Operationen zur Verfügung, welchen jeweils eine Entsprechung aus der klassischen Thermodynamik gegenübersteht: Bei der ersten Operation handelt es sich um die Kompression oder Ausdehnung einer der Komponenten (gemäß eines Kolbens); die zweite Operation ist die Kopplung von jeweils zwei der drei Teile, um einen Wärmeaustausch zu erreichen (ähnlich eines Ventils). Zur Beschreibung der Funktionsweise werden in dieser Arbeit numerische Simulationen der grundlegenden Operationen, sowie mehrerer Arbeitszyklen gezeigt. Weiters stellen wir experimentelle Ergebnisse für einen konzeptionellen Beweis der einzelnen Arbeitsschritte der QFM vor. Für diesen Zweck verwenden wir eindimensionale Bose-Einstein-Kondensate, die mithilfe eines Atomchips erzeugt werden. Schlussendlich werfen wir einen detaillierten Blick auf die Dynamik zweier stark gekoppelter unkorrelierter Bestandteile der QFM bei Anregung des Systems. Dabei können interessante Phänomene, wie etwa ein irregulärer Wärmefluss, beobachtet werden. Diese Arbeit steht am Anfang weiterführender Untersuchungen über die Quanten-Thermodynamik und liefert eine Toolbox zum Studium finiter Quantensysteme, weit entfernt vom üblicherweise angenommenen thermodynamischen Gleichgewicht.

Contents

Chapter 1

Introduction

The field of Thermodynamics was born two centuries ago back with the invention of the steam machine. Since then, the development of the field revealed to be extremely useful to study macroscopic systems whose behavior was to be understood from properties that characterize the state of a system without accounting for the individual dynamics of its constituents. Its resilience is to be noted, since it resisted major revolutions in physics like the appearance of General Relativity [1] and Quantum Mechanics [2]. Indeed, the applicability of the laws of thermodynamics [3] ranges from big systems such as black-holes [4, 5], to small quantum systems through the lens of information theory [6]. The applicability of thermodynamics to the latter is, however, very challenging. In this chapter, we briefly review the current status of the quantum thermodynamics field and introduce the work presented in this thesis as a new approach on how to tackle thermodynamic properties of finite quantum systems, using cold atoms described by Quantum Field Theory.

1.1 Thermodynamics and Quantum Mechanics

Thermodynamics and quantum mechanics are related since the birth of the latter. The assumption that light is quantized [7, 8] was introduced by Planck and developed by Einstein to explain the radiation emitted by a thermal black body. Since then, quantum mechanics and thermodynamics have taken different and independent paths. However, the increasing interest in systems (such as quantum many-body systems) whose physics can be addressed by both fields, makes it necessary to bring these together [9].

There is a fundamental problem when trying to bring these two fields under the same wing. On one hand, Thermodynamics provides tools to study large systems by ignoring individual motion and characterizing the global state of a system with a handful of parameters, e.g. temperature, volume and pressure. Furthermore, the time evolution of a system is not time-reversible, as demonstrated by Boltzmann when he derived the H-theorem [10] under the assumption of molecular chaos. An equivalent theorem for an isolated system is impossible to formulate due to the non-varying entropy of an isolated system [11]. Quantum Thermodynamics is then the field that tries to study how the tools and concepts of thermodynamics can be applied in the quantum realm [3]. The best efforts at this enterprise have been attempted by the Open Quantum Systems community. Usually the quantum system of interest is analyzed together with a 'bath' system with which there is an interaction. This approach yielded important results such as the Lindbald operator [12], and made possible describing the dynamics of a wide range of systems [13]. In this context, it is usually assumed that the system is Markovian and that the interaction between system and bath is weak [14]. Under these approximations, the calculations are fairly simple. However, several works have proposed solutions to go beyond these approximations, in pursuit of a universal non-equilibrium thermodynamic framework [15, 16].

Quantum thermodynamics, heavily influenced by the developments on open quantum systems, attempts at solving some of the open questions by applying the tools of thermodynamics to the quantum realm. Its ideal object of study is thus a system whose properties are of interest to both subjects. A quantum many-body system requires quantum mechanics to be described (by definition), while at the same time, it is infeasible to consider each and every of its degrees of freedom, making it suitable for statistical predictions using concepts from thermodynamics. In particular, the many-body system implemented by cold atom clouds, provide a flexible and interesting platform to explore some of the problems raised by quantum thermodynamics. The work presented in this thesis intends to do exactly that: using a cold atoms platform to explore thermodynamics with finite, isolated quantum systems.

The field of experimental cold atoms was born in 1995 when Anderson *et al* [17] achieved Bose-Einstein condensation of rubidium atoms. Since then, cold atoms experiments proved to be a very useful platform to explore many different topics [18]. Almost perfect isolation from the environment combined with a multiplicity of trap geometries and regimes of interactions, make cold atoms a very suitable tool for the implementation of quantum simulators [19] or the study of many-body physics. Regarding the latter, important contributions have been made in the subjects of pre-thermalization, recurrence of correlations, and gaussianity [20–24].

In this work, we use one dimensional BECs in the weakly interacting regime to study quantum thermodynamics in a goal-driven approach. We start by introducing the concept of Quantum Field Machine, laying out the general building blocks of a device that performs a task with a quantum system. Up until now, a diversity of heat machines working in the quantum regime have been proposed [25–28] . However, most of these proposals consider quantum systems whose degrees of freedom can be controlled, leaving aside the contributions from thermodynamics. The novelty of the machine proposed here is not only its very clear purpose but also the genuine quantum and thermal nature of its functioning [29]. The machine is conceived to be implemented with one dimensional BECs trapped with an atom-chip [30]. We start by describing each of the primitive operations that are necessary for the machine to perform work. Each of these basic operations is then investigated numerically using the standard models to decribe one-dimensional cold gases. Furthermore, the basic primitives are used to explore simple procedures such as energy transfer between two initially thermal clouds and more complex ones, namely, a cooling cycle which decreases the energy in one of the system components. The proof-of-concept of the QFM's building blocks is then demonstrated experimentally. Moreover, the experimental investigation goes further by exploring the energy dynamics of two atom clouds that are initially uncoupled and are merged into the storng coupling regime. The evolution of the system after this procedure is studied further, and phenomena such as heat flow is observed. This provides one of the first results regarding the thermodynamics of a many-body system far from the thermodynamic limit.

1.2 Thesis outline

- **Chapter 2:** The theoretical basis for working with cold atoms is provided. It starts by showing a very common model used to describe 1D cold atom clouds and then focuses on low-energy effective models, more suited to make prediction based on the measurable observables.

- **Chapter 3:** The experimental apparatus is described. The general working scheme of the experiment is provided. Since a lot of details have been carefully explained in other works, this chapter focus solely on the most relevant experimental parts needed for the work presented here. Namely, the procedure used to create arbitrary 1D potentials and the different possibilities to measure the atom cloud.

- **Chapter 4:** The concept of Quantum Field Machine is introduced. The different working parts of the machine are described and studied numerically. Afterwards, these working parts are used to build a numerical simulation of a refrigeration cycle. The chapter ends with a proof-of-concept experimental implementation of each primitive.

- **Chapter 5:** The local thermometry method is presented. The novelty brought by this new method is the ability of performing thermometry in specific regions of space, ignoring the remaining system. The method is exemplified and compared to previously standard methods (density ripples). This is followed by an example of how different temperatures in different regions of space can be measured and a subsequent discussion on the limitations on this method's applicability.

- **Chapter 6**: This chapter discusses the observation of heat flow in 1D Bose-Einstein Condensates. Initially, the motivation for studying such phenomena is justified. The notions of heat flow and anomalous heat flow in the context of 1D cold gases are introduced. Then, the experimental implementation and preparation of the initial state is described in detail. A theoretical description of this procedure is provided, comparing the quadratic Bogoliubov model with the results from the Stochastic Gross-Pitaevskii equation. Finally, the experimental results are presented, showing that both heat flow and anomalous heat flow are observed.

Chapter 2

Theoretical basis

This chapter covers the theoretical tools needed to understand the cold atom systems used in our experimental setup. We start by briefly looking at some peculiarities of working in one dimension. Afterwards, the Lieb-Liniger model is presented as the basis to derive the effective models used to describe the atom clouds in the different trap configurations allowed by the experiment. Then, the transition from 3D to 1D is discussed, clarifying the meaning of having a one-dimensional atom cloud and how that influences the properties of the system. Finally, we provide a description of the numerical methods used to simulate the relevant physical processes studied in this work.

2.1 The 1D interacting Bose gas

One-dimensional quantum physics is proof that low dimensionality is not a synonym of simplicity and uninteresting systems. On the contrary, 1D physics has proved to be an ideal platform to study fundamental physics and provides a plethora of models, some of them exactly solvable, others absolutely incalculable [31].

As an example, we can take a look at the free boson gas. At low enough temperatures, the phenomena of Bose-Einstein condensation starts taking place. While in 3D low temperatures or high densities lead to the condensation of the atoms in the ground state, in 1D such phenomena is not possible due to the density of states dependence on the energy. In 3D the density of states $\mathcal{D}(\epsilon) \propto \sqrt{\epsilon}$, where ϵ is the energy of the system. In 1D however the dependence is $\mathcal{D}(\epsilon) \propto 1/\sqrt{\epsilon}$, which means that for temperatures closer to zero, the number of states goes to infinity. For this reason, a macroscopic occupation of the lowest state is not possible in one dimension [32, 33].

For the case of an interacting gas of bosons, if ultracold temperatures are considered, the interaction between the different particles reduces to s-wave scattering. This is usually described with a pseudo-potential $U_{\text{int}} = g_{\text{3D}}\delta(\mathbf{r} - \mathbf{r}')$ [34], where the interaction constant g_{3D} is given by

$$g_{\text{3D}} = \frac{4\pi\hbar^2 a_s}{m}. \tag{2.1}$$

Here, m is the mass of the atoms and a_s the s-wave scattering length. The sign of a_s defines whether the interactions are repulsive ($a_s > 0$) or attractive ($a_s < 0$). We will focus our analysis on repulsive interactions, since for the ^{87}Rb [35] atoms used in our experiment we find $a_s = 5.2$nm. These interactions are inherited when the problem becomes one-dimensional. however, the interacting potential becomes approximately $U_{\text{int}} = g_{\text{1D}}\delta(z - z')$, with g_{1D} the one-dimensional interacting constant, and z the position along the axis of movement. The transition from 3D to 1D is discussed in section 2.3. For now, we can look at some other peculiarities of interacting gases in one dimension. When two particles collide in one dimension, the restrictions of energy and momentum conservation allow only for a swap of the latter, leaving the whole momentum distribution unchanged. Such a system is said to be integrable [36], in other words, the constraints on the system lead to many conserved quantities, which effectively reduces the dimension of its phase-space. This prevents phenomena such as thermalization. An experimental demonstration of a quantum Newton's cradle implemented with an integrable system was provided in [37].

In this section we will look at a 1D-model for interacting bosons introduced by Lieb and Liniger [38] and derive an effective description for a 1D atom cloud using an extension of the Bogoliubov theory for quasi-condensates.

2.1.1 Lieb-Liniger model

Bosons with a repulsive contact interaction can be described with the Hamiltonian [38]

$$H = \int dz \hat{\psi}^\dagger(z) \left[-\frac{\hbar^2}{2m}\partial_z^2 + U(z) - \mu + \frac{g_{1D}}{2}\hat{\psi}^\dagger(z)\hat{\psi}(z) \right] \hat{\psi}(z), \tag{2.2}$$

where $\hat{\psi}(z)$ is the field operator, $U(z)$ is the external potential, μ is the chemical potential, and g_{1D} is the 1D coupling constant. If the external and chemical potentials are not considered, the previous equation is known as the Lieb-Liniger (LL) Hamiltonian. This model has known solutions for the ground state and excitation spectrum [38, 39] .

We can construct two parameters that span the different regimes of the Lieb-Liniger model. Assuming that the gas has a linear density n_{1D}, then the well known Lieb-Liniger parameter γ can be defined as

$$\gamma = \frac{m g_{1D}}{\hbar^2 n_{1D}} \tag{2.3}$$

and defines the interaction strength. Note that the parameter (counter-intuitively) increases when the density decreases.

If we consider thermal systems, a second parameter depending on temperature can be defined as

$$t = \frac{2\hbar^2 k_B T}{m g_{1D}^2}, \tag{2.4}$$

where T is the temperature of the gas.

Combinations of different values of γ and t span the distinct phases of the LL model (see fig. 2.1). If $\gamma \gg 1$ and the temperatures are low, the system approaches the Tonks-Girardeau regime. There, the strong repulsion between particles mimics the Pauli exclusion principle and the bosonic wavefunction can be mapped onto one of spinless fermions [31]. In regimes with higher temperatures, the role of the interactions start to decrease, compared to the

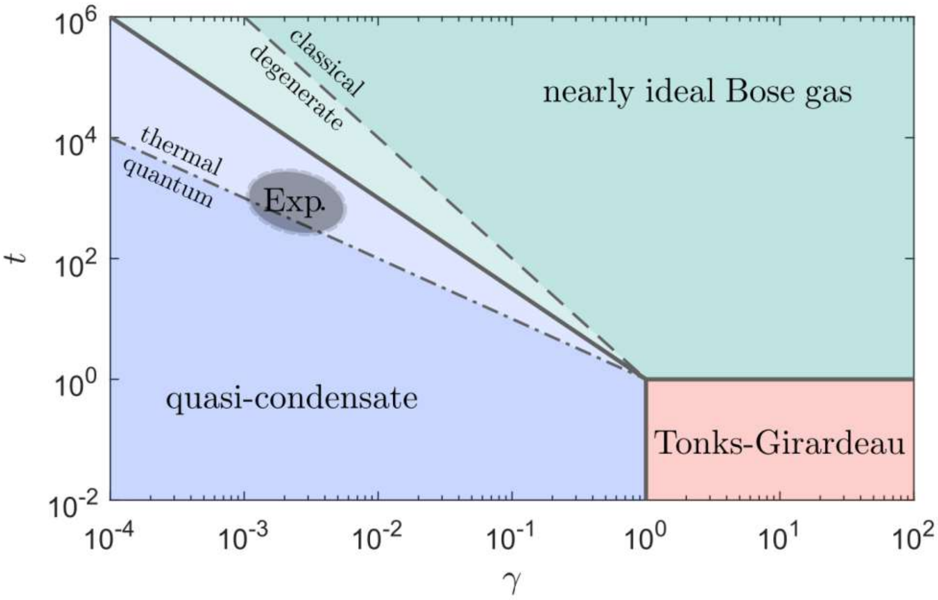

Figure 2.1: Phases of the Lieb-Lieniger model. Image adapted from [40].

thermal energy, and the system can be described as an ideal Bose gas. The crossover to the quasi-condensate regime happens when $t\gamma^{3/2} = 1$, where the interactions start to become important again and suppress the fluctuations in density [40].

On the other hand, when temperatures and interactions are both small ($\gamma, t \ll 1$), the system is in the quasi-condensate regime, where density fluctuations are suppressed but phase fluctuations prevail.

In the cross-over between the ideal Bose Gas and the quasi-condensate regime, there are two sub-regimes worth mentioning. When the de Broglie wavelength $\lambda_{dB} = \sqrt{2\pi\hbar^2 m k_b T}$ is of the order of the interparticle distance ($n_{1D}\lambda_{dB} \simeq 1$), the gas becomes degenerate and can no longer be described as a classical gas. This happens when $t\gamma^2 = 1$. Moreover, in the region between the ideal Bose gas and the quasi-condensate, the gas is dominated by thermal fluctuations. Only when $t\gamma \ll 1$, the quantum fluctuations become important.

The experiment described in this work operates in temperatures between 10-100nK with $n_{1D} \simeq 50\mu m^{-1}$. This translates to approximately $1 \cdot 10^{-3} \leq \gamma \leq 5 \cdot 10^{-3}$ and $2 \cdot 10^2 \leq t \leq 2.5 \cdot 10^3$, which places it in the quasi-condensate regime, dominated by thermal fluctuations.

2.1.2 Effective low energy models

There exist several analytical solutions for 1D systems cite{analytic solutions} but their utility is rather limited when it comes to calculate the dynamics of the system. To overcome this practicability problem, we use effective models which focus on the low-energy spectrum of the system and allow the predictions of observables accessible in the experiment.

In this work, we follow reference [41], which proposes an extension of the Bogoliubov theory to describe 1D quasi-condensates. The main idea is to do a perturbative expansion of the system's Hamiltonian and consider the relevant terms to describe our system.

In [41] the authors present a discretized version of the hamiltonian (2.2).

$$\hat{H} = \sum_z l\hat{\psi}^\dagger(z)\left[-\frac{\hbar^2}{2m}\Delta + U(z) - \mu + \frac{g_{1D}}{2}\hat{\psi}^\dagger(z)\hat{\psi}(z)\right]\hat{\psi}(z). \tag{2.5}$$

The differential operators are given by

$$\Delta f(z) = \frac{f(z+l) + f(z-l) - 2f(z)}{l^2}, \quad \nabla f(z) = \frac{f(z+l) - f(z-l)}{2l}. \tag{2.6}$$

The bosonic operator $\hat{\psi}$ ($\hat{\psi}^\dagger$) annihilates (creates) a particle in a cell of size l located at z. The commutation relation is

$$[\hat{\psi}, \hat{\psi}^\dagger] = \frac{\delta_{z,z'}}{l}. \tag{2.7}$$

These operators can be written in terms of other pairs of operators which connect to the experimental observables

$$\hat{\psi} = e^{i\hat{\theta}(z,t)}\sqrt{\rho_0(z) + \delta\hat{\rho}(z,t)}, \tag{2.8}$$

where $\hat{\theta}(z,t)$ describes the fluctuating phase and $\delta\hat{\rho}(z,t)$ the density fluctuations relative to the average density $\rho(z)$. These two new operators are also bosonic and inherit the commutation relation $[\delta\hat{\rho}(z), \hat{\theta}(z')] = i\delta(z-z')$. It is important to mention that this definition for the hermitian phase operator requires the space discretization mentioned above and that each box is not empty. More details can be found in [41].

Now, considering $\delta\hat{\rho}/\rho_0 \ll 1$ and $|l\nabla\hat{\theta}| \ll 1$ (density fluctuations and phase gradient are small), we expand equation (2.8) in these parameters and sort the expansion terms by their order [1] such that $H = H_0 + H_1 + H_2 + \ldots$.

The zeroth order is independent of both parameters and depends only on $\rho_0(z)$. It is minimized for a density profile $\rho_0(z)$ such that $\sqrt{\rho_0}$ is the solution of the discretized Gross-Pitaevskii equation (GPE):

$$H_0 = \left[\frac{\hbar^2}{2m}\Delta + U(z) - \mu + g_{1D}\rho_0(z)\right]\sqrt{\rho_0(z)} = 0. \tag{2.9}$$

For a density profile obtained from (2.9), H_1 always vanishes, and H_2 becomes the next leading order contribution describing the fluctuations

$$\begin{aligned} H_2 = \sum_z l\Bigg[&-\frac{\hbar^2}{2m}\frac{\delta\hat{\rho}}{2\sqrt{\rho_0}}\Delta\left(\frac{\delta\hat{\rho}}{2\sqrt{\rho_0}}\right) + \frac{\hbar^2\delta\hat{\rho}^2}{8m\rho_0^{3/2}}\Delta\sqrt{\rho_0} + \\ &+ \frac{g_{1D}}{2}\hat{\rho}^2 + \frac{\hbar^2}{2m}\sqrt{\rho_0(z)\rho_0(z+l)}\frac{[\hat{\theta}(z+l) - \hat{\theta}(z)]^2}{l^2}\Bigg] \end{aligned} \tag{2.10}$$

Although the space discretization is essential for the above description, in the coming discussions we will always use the notation of the continuum limit for the sake of clarity. In that context we can express equation (2.10) as

---

[1] We also assume both parameters to be of the same order.

$$H_2^{cont.} = \int dz \left[\frac{g_{1D}}{2} \delta\hat{\rho}^2(z) + \frac{\hbar^2}{2m}\rho_0(z) \left(\frac{\partial \hat{\theta}(z)}{\partial z} \right)^2 - \frac{\hbar^2}{2m} \frac{\delta\hat{\rho}(z)}{\rho_0} \left(\frac{\partial \delta\hat{\rho}(z)}{\partial z} \right)^2 \right]. \tag{2.11}$$

The last term in the previous equation is the so called quantum pressure term. Neglecting this term leads to a simpler Hamiltonian, known as the Tomonaga-Lutinger liquid (TLL) model [42, 43]. This is a relevant simplification, since the TLL model provides a linear dispersion relation, important for the observation of recurrent phenomena [22].

The Hamiltonian (2.11) can be diagonalized by a Bogoluibov transformation [44]. We define the creation and anihilation operators $\hat{b}_k^\dagger, \hat{b}_k$ for each mode and the basis functions $f_k^\pm(z)$, we can write the fields in the new basis as

$$\begin{aligned} \hat{\rho}(z) &= \sqrt{\frac{n_{1\mathrm{D}}}{2}} \sum_k \Big(f_k^+(z) \hat{b}_k e^{-i\omega_k t} + \mathrm{H.\ c.} \Big), \\ \hat{\theta}(z) &= \sqrt{\frac{1}{2n_{1\mathrm{D}}}} \sum_k \Big(-i f_k^-(z) \hat{b}_k e^{-i\omega_k t} + \mathrm{H.\ c.} \Big). \end{aligned} \tag{2.12}$$

In this work, we are mainly interested in the case where the atom trap has a box-shaped potential. For this reason (see chapter 3 for implementation details), we model the effective potential as a box with infinite walls and length L. For such a confinement, the particle flux is zero at the boundaries. Thus, the phase field, whose spatial derivative is proportional to the flux, has to fulfill Neumann boundary conditions

$$\frac{\partial \hat{\theta}(z)}{\partial z} \Big|_{z=0,L} = 0. \tag{2.13}$$

For this specific geometry, a box of length L has the following basis functions $f_k^\pm(z)$

$$f_k^\pm(z) = \frac{1}{\sqrt{L}} \left(\frac{\epsilon_k}{E_k} \right)^{\mp\frac{1}{2}} \cos(kz), \tag{2.14}$$

where the wavenumber k, the free particle energy E_k and the quasi-particle energy ϵ_k are given by

$$k = \frac{\pi}{L} n, \qquad E_k = \frac{\hbar^2 k^2}{2m}, \qquad \epsilon_k = \sqrt{E_k(E_k + 2n_{1\mathrm{D}} g_{1\mathrm{D}})}. \tag{2.15}$$

By plugging equation (2.12) into (2.11), we obtain a diagonal hamiltonian in terms of the newly defined operators $\hat{b}_n$ and $\hat{b}_n^\dagger$

$$\hat{H}_{LL} = \sum_n \hbar\omega_n \hat{b}_n^\dagger \hat{b}_n. \tag{2.16}$$

In the limit of low energies ($\epsilon_k/E_k \ll 1$), the energy of the quasiparticles can be approximated by

$$\epsilon_k \simeq \hbar c k = \hbar \omega_n, \tag{2.17}$$

where $c = \sqrt{g_{1\mathrm{D}} n_{1\mathrm{D}}/m}$ is the speed of sound and $\omega_k = \pi c n/L$ is the angular frequency of the n^{th} mode. This is the linear and commensurate spectrum of the TLL model mentioned above.

2.2 The double well

In our experimental setup, we can manipulate the Radio-Frequency fields to transform the single harmonic trap in a double well (DW) potential along one of the tightly confined dimensions (see Chapter 3). Thus, it is possible to have two parallel gases separated by a tunable barrier. By changing this barrier, it is possible to tune the interaction between the two gases. Assuming that we remain in the regime of low energy scales, we can apply the same model used in the case of the single gas ((2.2)). Now we consider this Hamiltonian for each cloud and an extra coupling term [45]:

$$\hat{H}_{\mathrm{DW}} = \hat{H}_1 + \hat{H}_2 + \hat{H}_t, \tag{2.18}$$

where

$$\hat{H}_{1,2} = \int dz \hat{\psi}^{\dagger}_{1,2}(z) \left[-\frac{\hbar^2}{2m}\partial_z^2 + U(z) - \mu + \frac{g_{1D}}{2}\hat{\psi}^{\dagger}_{1,2}(z)\hat{\psi}_{1,2}(z) \right] \hat{\psi}_{1,2}(z), \tag{2.19}$$

$$\hat{H}_t = -\hbar J \int dz \left[\hat{\psi}_1^{\dagger}\hat{\psi}_2 + \hat{\psi}_2^{\dagger}\hat{\psi}_1 \right]. \tag{2.20}$$

Here J is the tunneling rate and sets how strong the transversal wavefunctions overlap. Notice that $\hat{H}_t$ considers linear tunnel coupling. We consider a regime where the barrier is high enough and higher order coupling terms can be neglected.

The DW configuration features the measurement of phase differences between the two gases (see section 2.2.1). Since this is one of the main observables, the next subsection describes in detail the mathematical framework to treat it. In the context of this work, we will only analyze the case for $J = 0$, for all the measurements were done with completely decoupled gases. For the case where $J \neq 0$ the reader is referred to the PhD thesis mentioned in the beginning of this chapter as well as [20, 21].

2.2.1 Uncoupled double well

In case the two adjacent gases are uncoupled ($\hat{H}_t = 0$), each of them behaves as an independent condensate and the $\hat{H}_{\mathrm{DW}}$ is simply the sum of the Hamiltonians in equation (2.19). It is then possible to treat each of them as a gas in a single well, as discussed in section 2.1.2. If this is the case, then the equation(2.11) describes each gas and the effective hamiltonian for the DW reads [2] (we are neglecting the quantum pressure term)

---

[2] We have assumed the same density profile for both atom clouds.

$$H_{LL}^{DW} = \sum_i \int dz \left[\frac{g_{1D}}{2} \delta\hat{\rho}_i^2(z) + \frac{\hbar^2}{2m} \rho_0(z) \left(\frac{\partial \hat{\theta}_i(z)}{\partial z} \right)^2 \right]. \tag{2.21}$$

with $i = 1, 2$. It is now convenient to introduce the relative (r) and common (c) degrees of freedom

$$\delta\hat{\rho}_c(z) = \delta\hat{\rho}_1(z) + \delta\hat{\rho}_2(z), \qquad \phi_c(z) = \frac{1}{2}[\hat{\theta}_1(z) + \hat{\theta}_2(z)] \tag{2.22}$$

$$\delta\hat{\rho}_r(z) = \frac{1}{2}[\delta\hat{\rho}_1(z) + \delta\hat{\rho}_2(z)], \qquad \phi_r(z) = \hat{\theta}_1(z) + \hat{\theta}_2(z) \tag{2.23}$$

Using this definition, it is possible to rewrite Hamiltonian (2.21) in terms of the new degrees of freedom as

$$H_{LL}^{i} = \sum_i \int dz \left[g_{1D} \frac{\delta\hat{\rho}_i^2(z)}{\sqrt{\zeta}} + \frac{\hbar^2}{4m} \rho_0(z) \left(\sqrt{\zeta} \frac{\partial \hat{\phi}_i(z)}{\partial z} \right)^2 \right], \tag{2.24}$$

where $i = r, c$ and ζ rescales the terms in the hamiltonian for different i. We have $\zeta_r = 1$ and $\zeta_c = 4$ [46]. Note however that to do this, it is crucial that the density profile is the same for both clouds. In [47], it is described how to treat the problem if this is not the case.

For an ideal box confinement, the boundary conditions are inherited from the individual gas. It is also possible to define the co-sine modes for the new degrees of freedom as before by scaling the expansion coefficients accordingly

$$\hat{\rho}_k^i = \sqrt{\zeta} \sqrt{\frac{n_{1\mathrm{D}}}{2} \frac{\mu}{\epsilon_k}} \left(\hat{b}_k e^{-i\omega_k t} + \hat{b}_k^\dagger e^{i\omega_k t} \right), \tag{2.25}$$

$$\phi_k^i = -i \frac{1}{\sqrt{\zeta}} \sqrt{\frac{1}{2n_{1\mathrm{D}}} \frac{\epsilon_k}{\mu}} \left(\hat{b}_k e^{-i\omega_k t} - \hat{b}_k^\dagger e^{i\omega_k t} \right), \tag{2.26}$$

where $\mu = g_{1\mathrm{D}} n_{1\mathrm{D}}$ is the chemical potential

2.2.2 Phase correlation function

When the double well configuration is used, it is possible to measure the interference pattern formed by the two parallel clouds (see chapter 3). From this interference pattern we can extract the relative phase profile introduced in equation (2.23). Here we lay out how we can use this degree of freedom to compute important spatial correlation functions which provide information about the system. For the sake of simplicity, we will from now on drop the subscript from ϕ_r, using simply ϕ to refer to the relative phase.

The second order correlation function of the fields is given by

$$\frac{\langle \psi_1(z) \psi_2^\dagger(z) \psi_1^\dagger(z') \psi_2(z') \rangle}{\langle |\psi_1(z)|^2 \rangle \langle |\psi_2(z')|^2 \rangle} \simeq \langle e^{i[\phi(z) - \phi(z')]} \rangle, \tag{2.27}$$

assuming density fluctuations to be negligible. For systems invariant under the transformation $z \to -z$ we can take the real part of equation (2.27), which yields

$$C(z, z') = \langle \cos(\phi(z) - \phi(z')) \rangle = e^{-\frac{1}{2}\langle(\phi(z)-\phi(z'))^2\rangle}. \tag{2.28}$$

The second equality is valid under the quadratic approximation only.

We will refer to this quantity as the phase correlation function (PCF). It measures how correlated the field ϕ is in two different points in space. It returns 1 if the points are totally correlated and zero for uncorrelated ones. As we will see, it can be used to estimate the temperature of the system and can also be used to probe local properties of it (see chapter 5).

If translational invariance can be assumed, the PCF depends only on the distance between the two points

$$C(\bar{z} = |z - z'|) = \exp\big[-\frac{1}{2}\langle[\phi(z) - \phi(z')]^2\rangle\big] \tag{2.29}$$

$$= \exp\big[-\int_0^\infty \frac{\mathrm{d}k}{\pi}\langle|\phi_k|^2\rangle[1 - \cos(k\bar{z})]\big]. \tag{2.30}$$

If thermal, the bosonic fields follow the Bose-Einstein (BE) distribution [48], given by

$$n_{\mathrm{BE}}(\epsilon_k) = \frac{1}{\exp\left(\frac{\epsilon_k}{k_B T}\right) - 1} \tag{2.31}$$

where ϵ_k is the energy of mode k. Given that the we work in the regime where $\epsilon_k / k_B T \ll 1$, we can approximate equation (2.31) with the Raylkeigh-Jeans approximation

$$n_{\mathrm{BE}}(\epsilon_k) \simeq \frac{k_B T}{\epsilon_k}. \tag{2.32}$$

By inserting the expectation values of $\langle|\phi_k|^2\rangle$ given by equation (2.32) and performing the integration, we arrive at

$$C(\bar{z}) = \exp\left[-\frac{2\bar{z}}{\lambda_T}\right], \tag{2.33}$$

where $\lambda_T = 2\hbar^2 n_{1\mathrm{D}} / m k_B T$ is the thermal coherence wavelength of the two gases (the factor of two accounts for the double well configuration [49]).

Since the results presented in this thesis concern the box potential, the PCF for an atom cloud in a box-like potential is exemplified in figure 2.2. Notice that the diagonal (where $\bar{z} = 0$) is always one, while for points away from the diagonal the value of the PCF decreases. The PCF decreases faster for higher temperatures.

2.3 3D to 1D crossover

So far, we've looked only at 1D models without providing any argument for the fact that our system is effectively one-dimensional. This section justifies why this is the case.

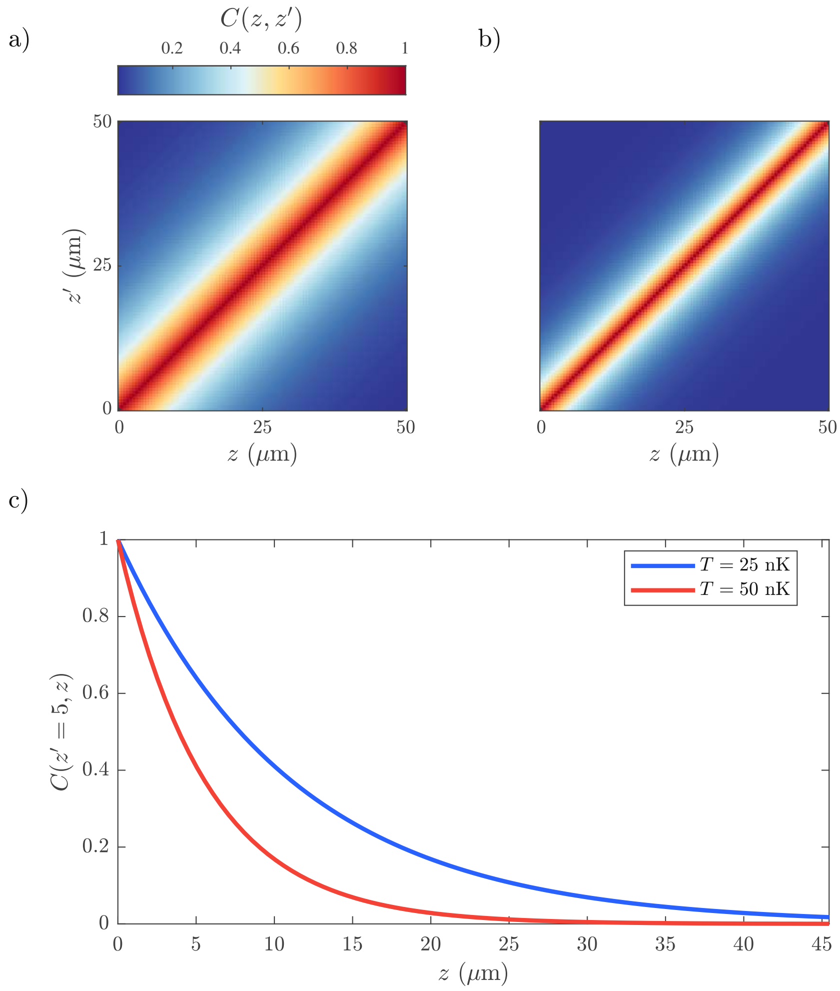

Figure 2.2: **Phase correlation function for two quasi-condensates at different temperatures.** The phase correlation functtions were computed for atom clouds exhibiting temperatures of a) 25 nK and b) 50 nK. In c) a cut for $z = 5\,\mu\text{m}$ is shown. As expected the phase correlations decay faster for the hotter condensate. Both atom clouds are 50 µm long and have a density of $50\,\mu\text{m}^{-1}$.

As any other physical system, the cold gases used in our experiment are three dimensional. However, the effective dimensionality of the system can be lowered by using tight confinement in some directions, as it is common practice in the field of cold atoms [50]. If this confinement is such that the energy level spacing is much larger than the remaining energy scales, then the surpressed dimensions can be integrated out. In our experiment, two of the directions (called the transverse directions) are confined in a harmonic potential with trap frequency $\omega_\perp$ such that

$$\hbar\omega_\perp \gg k_B T, \mu. \tag{2.34}$$

This ensures that any thermal energy and the interaction energy per particle is much smaller than the trapping frequency of the trap and thus no excitations in these directions are possible.

In the next subsections, we dive deeper into how this affects our system.

2.3.1 Transverse broadening

To better understand the influence of the transverse directions and its consequences when the condition given by (2.34) is not completely fulfilled, we follow references [51, 52]. The Hamiltonian for Bosons in 3D with contact interaction under the influence of a potential $U(z)$ is

$$H = \int dz \Psi^*(r) \left[-\frac{\hbar^2}{2m}\partial_r^2 + \frac{m\omega_\perp^2(x^2+y^2)}{2} + U(z) + g_{3D}|\Psi(r)|^2 \right] \Psi(r), \tag{2.35}$$

where g_{3D} is given by (2.1). We want to look only to the dynamics along z. Assuming the separability of the wavefunction $\Psi(r) = \phi(x,y)\cdot\psi(z)$, we can integrate out the other two directions. As it was mentioned before, the transverse directions are restricted to the ground state of the harmonic confinement. Thus we can assume that ϕ is given by a Gaussian whose standard deviation is the harmonic oscillator length $a_\perp = \sqrt{\hbar/m\omega}$

$$\phi(x,y) = \frac{1}{a_\perp^2\sqrt{\pi}} e^{-\frac{x^2+y^2}{2a_\perp^2}} \tag{2.36}$$

Integrating the x and y components of (2.35) yields a constant (and unimportant) energy shift and a renormalization of the interaction constant

$$g_{1D} = g_{3D} \int \mathrm{d}x\mathrm{d}y |\phi(x,y))|^4, \tag{2.37}$$

recovering eq. (2.38). Notice that, contrary to g_{3D}, g_{1D} depends on the trapping frequency.

If $a_\perp$ is of the order of a_s a more meticulous analysis is necessary. Reference [53] presents a relation between the 3D scattering length a_s and the 1D interaction constant g_{1D} when this is the case:

$$g_{1D} = 2\hbar\omega_\perp a_s \left(1 - \gamma\frac{a_s}{a_\perp}\right)^{-1}, \tag{2.38}$$

where $\gamma \simeq 1.03$ is a numerical factor and $a_\perp = \sqrt{\hbar/(m\omega_\perp)}$ accounting for a confinement induced resonance [54] . In the experiment, we have $a_s/a_\perp \simeq 0.02$, which is well approximated by (2.37). Given the context of this work, we have $\omega_\perp = 1.4$ kHz, $T = 40$ nK and a linear density of $\rho_0 = 50\ \mu\text{m}^{-1}$ and $a_s = 5.2$ nm. Thus we find that $k_B T/(2\pi\hbar) \simeq 1041$ Hz and $\mu/(2\pi\hbar) = g_{1D}\rho_0/(2\pi\hbar) \simeq 750$ Hz, from where we conclude that condition (2.34) is only partially fullfilled.

To investigate the consequences thereof, we consider that all atoms are in the transverse ground state and that the interactions between them can be neglected only if the system is dilute, i.e., $n_{1D}a_s \ll 1$. If this is not the case, then the interactions start to play a role and are expected to broaden the transverse wavefunction ϕ. It is thus natural to consider an ansatz where ϕ is a gaussian of variable width $\sigma(z,t)$

$$\phi(x, y, \sigma(z,t)) = \frac{1}{\sigma^2(z,t)\sqrt{\pi}} e^{-\frac{x^2+y^2}{2\sigma^2(z,t)}}. \tag{2.39}$$

Inserting this ansatz in eq. (2.35) and minimizing with respect to σ(z,t), we get

$$\sigma^2(z,t) = a_\perp^2 \sqrt{1 + 2a_s|\psi(z)|^2}, \tag{2.40}$$

and the chemical potential

$$\mu = \hbar\omega_\perp \frac{1 + 3a_s n_{1\text{D}}}{\sqrt{1 + 2a_s n_{1\text{D}}}}. \tag{2.41}$$

Using these results and inserting them in equations (2.39) and (2.35) and integrating over the xy plane, we arrive at

$$H = \int dz \psi^*(z) \left[-\frac{\hbar^2}{2m}\partial_z^2 + U(z) + \hbar\omega_\perp \sqrt{1 + 2a_s|\psi(z)|^2} \right] \psi(z). \tag{2.42}$$

Note that for $a_s|\psi(z)|^2 \ll 1$ (weak interaction regime), we recover eq. (2.2).

Using eq. (2.42) and applying the same method used in section 2.1.2 we get a new version of the GPE equation which accounts for the effects of the transverse directions, also known as the Non-Polynomial Schödinger Equation (NPSE) [51]

$$\left[-\frac{\hbar^2}{2m}\Delta + U(z) - \mu + \hbar\omega_\perp \frac{1 + 3a_s\rho_0}{\sqrt{1 + 2a_s\rho_0}} \right] \sqrt{\rho_0} = 0. \tag{2.43}$$

The interactions broaden the longitudinal wavefunction as shown in [55]. The broadening of the longitudinal profile depends on its anisotropy along this direction [56]. In this work we will be mainly concerned with a box-like potential, where the density is constant across space. For this reason, the effects of the transverse broadening will not change the density profile considerably [40], but will change other physical quantities.

The speed of sound, introduced in (2.17), can be written as [57, 58]

$$c = \sqrt{\frac{n_{1\text{D}}}{m} \frac{\partial\mu}{\partial n_{1\text{D}}}} = c_0 \sqrt{\frac{1}{2} \frac{2 + 3a_s n_{1\text{D}}}{(1 + 2a_s n_{1\text{D}})^{3/2}}} = \sqrt{\frac{g_n n_{1\text{D}}}{m}}, \tag{2.44}$$

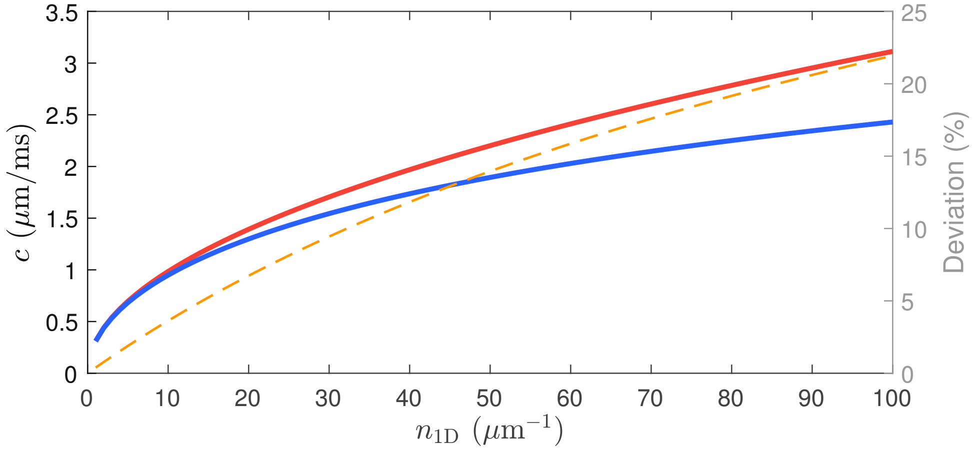

Figure 2.3: **Speed of sound in 1D:** Comparison of the bare speed of sound from Bogoliubov theory (red curve) and speed of sound from eq. (2.44), considering broadening of the longitudinal profile (blue curve). The yellow curve indicates the deviation between the two in percentage (right axis).

where $c_0 = \sqrt{g_{1\mathrm{D}} n_{1\mathrm{D}}/m}$ is the bare speed of sound introduced before and g_n is the effective density-dependent interaction energy, which was obtained considering the second order description of fluctuations.

For typical densities $n_{1\mathrm{D}} \simeq 60\ \mu\mathrm{m}^{-1}$, we have differences on the order of 20 % (see fig. 2.3) which has deep implications when computing the rephasing times of the modes or calculating the position of perturbations in the system [22].

2.4 Numerical methods

Part of this work concerns the introduction of a new model for a Quantum Field Machine (see chapter 4) and which primitive procedures are needed to operate it. To study the building blocks of such machine and what kind of processes can emerge from them, we need different numerical tools that simulate their dynamics. Not only is it important to perform this simulations to study in detail the properties of the machine and its processes, but also to have the theoretical predictions to compare with experimental results. For both these purposes, we use two different software packages, briefly described in the following sections.

2.4.1 Tomonaga-Lutinger Liquid simulations

The code used to simulate the primitive operations needed to operate the QFM implements the Tomonaga-Lutinger liquid Hamiltonian, the same as the one in equation. (2.11), when the quantum pressure term is ignored. It reads

$$H_{TLL} = \int dz \left[\frac{g_{1D}}{2} \delta\hat{\rho}^2(z) + \frac{\hbar^2}{2m} \rho_0(z) \left(\frac{\partial \hat{\theta}(z)}{\partial z} \right)^2 \right]. \tag{2.45}$$

In addition, we introduce an interaction term to regularize the zero mode [29]. This allows us to simulate the dynamics of phonons and to calculate corresponding energy changes in the system. As the model is quadratic, our simulations are done within the Gaussian framework and are computationally efficient. The code also provides tools for the calculation of quantities related to quantum information, e.g., relative entropy. This is the only information-theoretic related quantity discussed in this thesis and is defined as

$$S(\hat{\rho}, \hat{\gamma}) = \mathrm{Tr}(\hat{\rho}(\log(\hat{\rho}) - \log(\hat{\gamma}))). \tag{2.46}$$

It quantifies the distance between two states with density matrices $\hat{\rho}$ and $\hat{\gamma}$. If $\hat{\rho} = \hat{\gamma}$, then $S(\hat{\rho}, \hat{\gamma}) = 0$. In the context of this work, we compute S between the state of the system we study and a thermal state at temperature T. This is used to quantify how far from thermality the system under study is.

The details about this simulation package can be found in section IV and appendix C of [29]. The base code was written by Marek Gluza and was extended with contributions from the collaborators.

2.4.2 SGPE method

To compare the experimental results with the predictions from theory, we use a code that implements the Stochastic Gross-Pitaevskii equation (SGPE) and is tailored to match the specifics of our experimental apparatus.

The SGPE method allows the simulation of thermal states by modeling incoherent scattering with a thermal background. This is done by adding a dissipative term in the equation of motion and noise term proportional to the temperature. The evolution of the field (for a single gas) is given by the Langevin equation

$$i\hbar\partial_t\psi = (1 + i\gamma)H_{GP}\psi + \eta, \tag{2.47}$$

where H_{GP} is the non-polynomial GPE operator (see eq. (2.43)) and η is a complex Gaussian white-noise with zero mean and variance [46]

$$\langle \eta(z,t)\eta(z't') \rangle = 2\gamma(z,t)k_BT\delta(z - z')\delta(t - t'). \tag{2.48}$$

The term γ merely defines the speed with which convergence to a thermal state is achieved. If one is interested only in the final thermal state and not the evolution, then this is an arbitrary term. The code was written by Sebastian Erne (I adapted the code to extend its functionalities. Namely, a double-box potential was added to allow compressing and merging procedures, as discussed in chapter 6).

Chapter 3

Experimental setup

In this chapter, we will describe the experimental apparatus used to study thermodynamics with one dimensional quasi-condensates. The description won't be extensive, since very thorough descriptions are available in previous works. This introduction serves as a general overview. For more specific and detailed descriptions of the experiment, the reader is referred to [40, 49, 59–61].

In section 3.1, we provide a general description of the experimental cycle, which is executed before each measurement is performed. In general, the experiment relies on laser cooling techniques [34, 62, 63] to reduce the temperature of the trapped ^{87}Rb [35] atoms before these get under the influence of the atomchip. The atomchip is a device that allows experimentation with one-dimensional atom clouds and lies at the core of the experimental procedures described in this thesis. In section 3.2 we describe the magnetic harmonic traps generated by this device. In sections 3.3 and 3.4 we overview the physics of dipole traps and relevant details about light manipulation for the creation of arbitrary 1D potentials, respectively. Regarding the latter, the box-shaped potential is crucial for the scope of this work. For that reason, specific examples and particular details for this potential are mentioned throughout the chapter.

3.1 Experimental cycle overview

In this section, we provide a short walk-through over the cycle that produces the quasi-BECs. The experiment consists of two vacuum chambers as show in figure 3.1 .

The lower vacuum chamber holds Rubidium dispensers. The dispensers release ^{87}Rb into this chamber and these atoms are trapped in a standard six-beam 3D Magneto-Optical Trap (MOT). This chamber is connected to an upper chamber, which we shall denote by "Science Chamber".

These two are connected through a nearly resonant laser beam which transports the atoms from one chamber to the other. In the Science chamber there is another 3D MOT which collects and cools the atoms coming from below. We name this MOT as the "upper MOT".

The Science Chamber houses the atomchip, which is hanging upside down as shown in figure 3.1 a). This prevents access from the top of the chamber. This is the reason why two beams are reflected on the gold surface of the atom chip together with four incoming beams

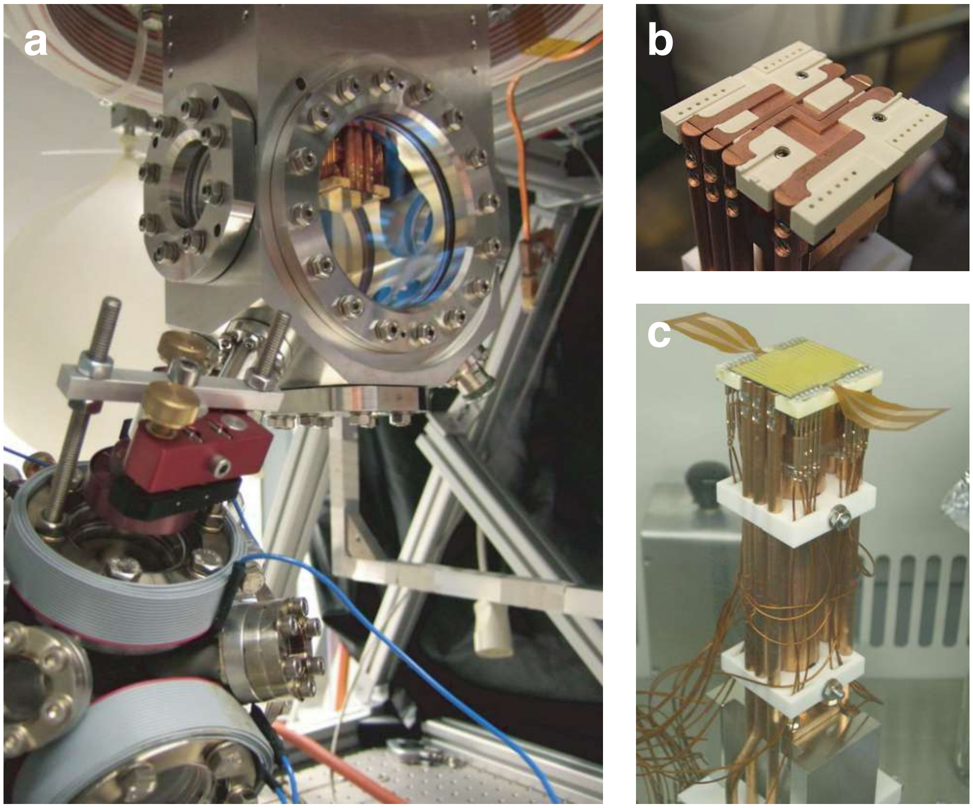

Figure 3.1: **Experimental apparatus:** the atoms are cooled down in the a) Vacuum chambers which hold the b) copper wire structures that help the manipulation of the magnetic. On top of these copper wire structures lies the c) the atomchip. Note that the orientation of the atomchip inside the vacuum chamber is the opposite of that found in c). The hanging atomchip is visible through the vacuum chamber's glass window in a). Figure adapted from [40]

to create the upper MOT. Both MOTs are on for an approximate time of 10 seconds in total (this is called the MOT phase). By tuning the intensities and frequencies of the laser and increasing the magnetic fields, the upper MOT is compressed and shifted to move the atoms closer to the atomchip.

In the next stage, further cooling of the atoms is performed through the process of optical molasses. This method allows to achieve sub-doppler cooling [64] and is followed by optical pumping which consists of a short laser pulse to populate the $|F = 2, m_F = 2\rangle$ spin state, which can be magnetically trapped. At the end of this process, the atoms are loaded into a magnetic trap which we will refer to as "Z-trap".

Above the chip [1], there are macroscopic copper structures whose main purpose is to generate a cigar-shape magnetic trap to hold the atoms before they are transfered to the atomchip trap. The Z-trap is generated by the Z-shaped copper wire together with a bias field generated by one of the Helmholtz coils around the vacuum chamber. At the end of this cooling stage, we end up with a cloud of approximately 2 million atoms at a temperature

---

[1] To avoid confusion, we use figure 3.1 a) as a reference. Here, a "above" mean farther away from the ground.

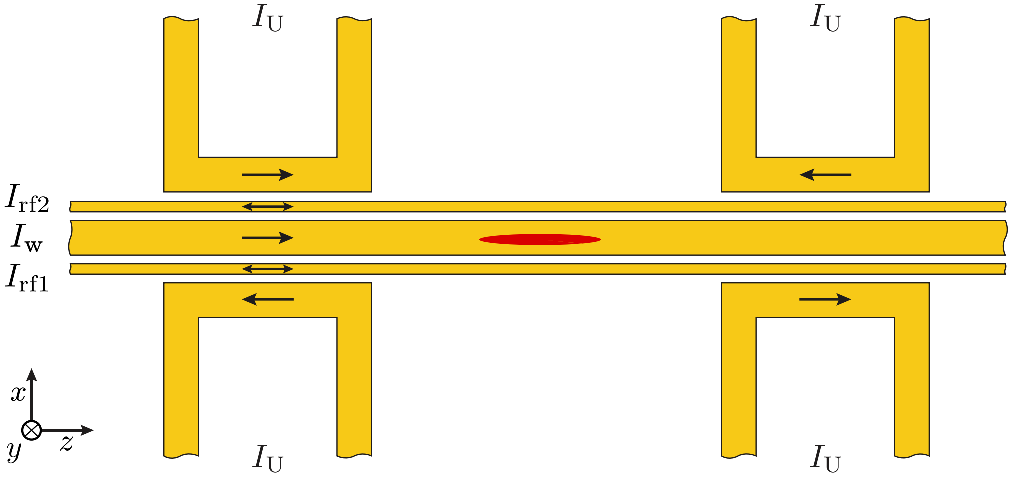

Figure 3.2: **Atom chip wire structure:** The arrows indicate the direction of current flow and the red elipse in the center represents the atomcloud. Although all the wires used in the experiment are represented here, this is not the complete structure; for a complete description of the atomchip see [60]. Figure adapted from [40].

of 1 – 3µK. While in this magnetic trap, the technique of evaporative cooling [65, 66] is employed using radio frequency (RF). The RF fields are also generated by one of the copper structures right above the chip.

While this process is carried on, the atoms are transfered to the chip, where the 1D harmonic potential is created through the currents in the chip wires. The process of evaporative cooling continues, leading to the preparation of the one-dimensional quasi-condensates. At the end, we have a 1D atom cloud with around 10000 atoms with temperatures ranging from 15 – 50nK (it depends on whether the dipole trap is used; usage of the dipole trap leads to higher temperatures).

The atoms can be held in the chip trap for different amounts of time. Typically, experimental investigations in the chip last up until 150ms. At the same time that the atoms are being held in the chip and the evaporative cooling is carried on, the blue-detuned light which creates the dipole trap is ramped. Ramping up the dipole light intensity instead of turning it in a sudden fashion prevents atom loss and minimizes the energy introduced by atom-light interaction.

The cycle ends with the imaging of the cloud. The atomchip trap is turned off and absorption imaging takes place after time of flight (TOF) expansion. Some of the details of the imaging and trapping geometries are discussed in the following sections.

3.2 The atomchip trap

The atomchip [30] is made of a single gold layer isolated from a silicon substrate by a thin layer of silicon dioxide. A scheme of the atomchip wire structure is shown in figure 3.2. Having the areas between the wires covered in gold, helps to increase the reflectivity on the chip, which is important for the MOT phase (as discussed in section 3.1).

The main wire has a current I_W going through, which generates a circular magnetic field.

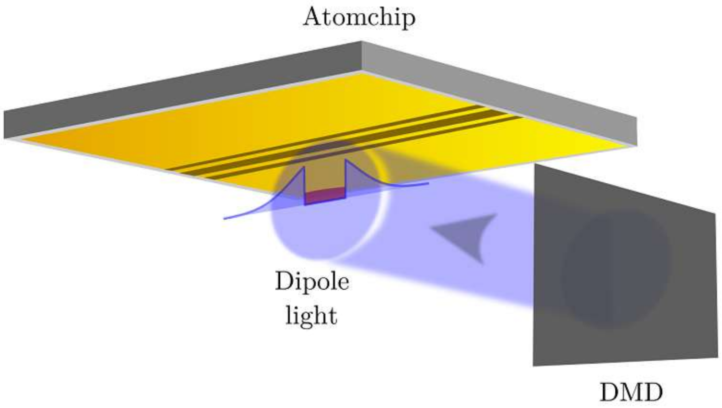

Figure 3.3: **Atom chip and dipole trap:** the atoms are subject to the superposition of the magnetic trap generated by the Atomchip and the light field shaped by the DMD (section 3.4). The DMD has the ability to shape the light in time, allowing the implementation of time dependent potentials. When used in the double well configuration, the light affects both clouds in the same way. Image adapted from [40].

Together with the bias field in the x and y directions, these fields generate a very confined trap in these directions. With the usual configurations, the minimum of the trap sits 100µm below the chip [40]. The longitudinal confinement is generated by the U-wires shown in figure 3.2. An additional bias field in the z direction lifts the frequency of the Zeeman energy splitting in the trap center to 390kHz. The typical frequencies of trap are $\omega_\perp = 2\pi \cdot 2.1$kHz for the very tightly confined directions and $\omega_z = 2\pi \cdot 10$Hz in the weakly confined direction.

As already mentioned in chapter 2, it is possible to create a dressed trap which provides a double well 1D harmonic configuration 3.3. This is possible by applying RF currents to the 30 µm wires on each side of the wider wire in the center of the atomchip. The oscillating field pointing along y (here the vertical direction) creates a double well along x (perpendicular to gravity). This specific orientation of the double well is achieved by setting a relative phase shift of π between the currents in each wire (for more details consult [67, 68]). Tipically, each well in this configuration has trapping frequencies $\omega_\perp = 2\pi \cdot 1.45$kHz and $\omega_z = 2\pi \cdot 7$Hz. Changing the current magnitude allows the control of the coupling between the two wells. In this thesis all the experiments were done in the uncoupled double well (see figure 3.3 for an illustration).

Corrugations in the main trapping wire lead to imperfections on the current distribution which then generate unwanted spatial modulations of the magnetic potential [69–71]. Besides this, the harmonic potential (single or double well) is the only geometry achievable with the atomchip. Other types of potentials can be achieved with a dipole trap. That is the topic of the next section.

3.3 Optical traps in a nutshell

Optical dipole traps make use of the electric-dipole interaction with far-detuned light. One of the biggest advantages of this kind of traps is the fact that the optical excitation can be kept extremely low and it allows for a wide range of trap geometries. In this section, we will provide a brief description of the underlying mechanisms of dipole traps. We follow reference [72], where a complete description can be found.

Considering the electric-dipole interaction between a two-level atom and an electric field E, we can use second order perturbation theory to calculate the energy shift of the ground state due to this interaction:

$$\delta\epsilon = \frac{|\langle e|\, V\, |g\rangle\,|^2}{\epsilon_g - \epsilon_e}, \tag{3.1}$$

where $V = -\mu_e E$ is the interaction term with the electric field, $\epsilon_{\mathrm{g,e}}$ are the energies of the ground state $|g\rangle$ and $|e\rangle$, respectively. Considering the system "field and atom", we can write explicitly the energies $\epsilon_{g,e}$. When the atom is in the ground state (internal energy is zero) we have $\epsilon_g = n\hbar\omega$, where n is the number of photons and ω the frequency of the field; if the atom is excited, a photon is absorbed, which leads to $\epsilon_e = \hbar\omega_0 + (n-1)\hbar\omega$, with $\hbar\omega_0$ the energy of the atomic transition.

We can rewrite the energy shift of the ground state as

$$\delta\epsilon = \frac{|\langle e|\, \mu\, |g\rangle\,|^2}{\hbar\Delta} = \frac{3\pi c^2}{2\omega_0^3}\frac{\Gamma}{\Delta} I \tag{3.2}$$

where we have used the linewidth Γ

$$\Gamma = \frac{\omega_0^3}{3\pi\epsilon_0\hbar c^3}|\,\langle e|\, \mu\, |g\rangle\,|^2 \tag{3.3}$$

and the intensity $I = 2\epsilon_0 c|E|^2$. Now it becomes clear that Stark shift on the ground state is proportional to the detuning Δ. In a regime where the saturation is low, the atom spends most of the time in the ground state and the light-shift can be interpreted as the relevant potential for the atom. For the excited state, the shift has the opposite sign. Notice that for blue-detuned light ($\Delta > 0$) the potential created by the light becomes repulsive, while for red-detuned light ($\Delta < 0$) we get an attractive potential.

For multi-level atoms, the energy shift is calculated by summing the contributions from all the electronically excited states. In particular for alkali atoms such as ^{87}Rb, the fine structure splitting of the D line leads to the dipole potential

$$U_{dip}(r) = \frac{\pi c^2\Gamma}{2\omega_0^3}\left(\frac{1}{\Delta_{D_1}} + \frac{2}{\Delta_{D_2}}\right) I(r), \tag{3.4}$$

where Δ_{D_1} and Δ_{D_2} are the individual detunings to the $D_1(^2S_{1/2} \rightarrow ^2 P_{1/2})$ and $D_2(^2S_{1/2} \rightarrow ^2 P_{3/2})$ lines. Here we assume all detunings are much larger than the excited state hyperfine splitting. In equation 3.4, linearly polarized light was also assumed. The case for circularly polarized light is discussed in [72].

Under the same assumptions, we can also write an expression for the scattering rate of dipole light photons by the atoms

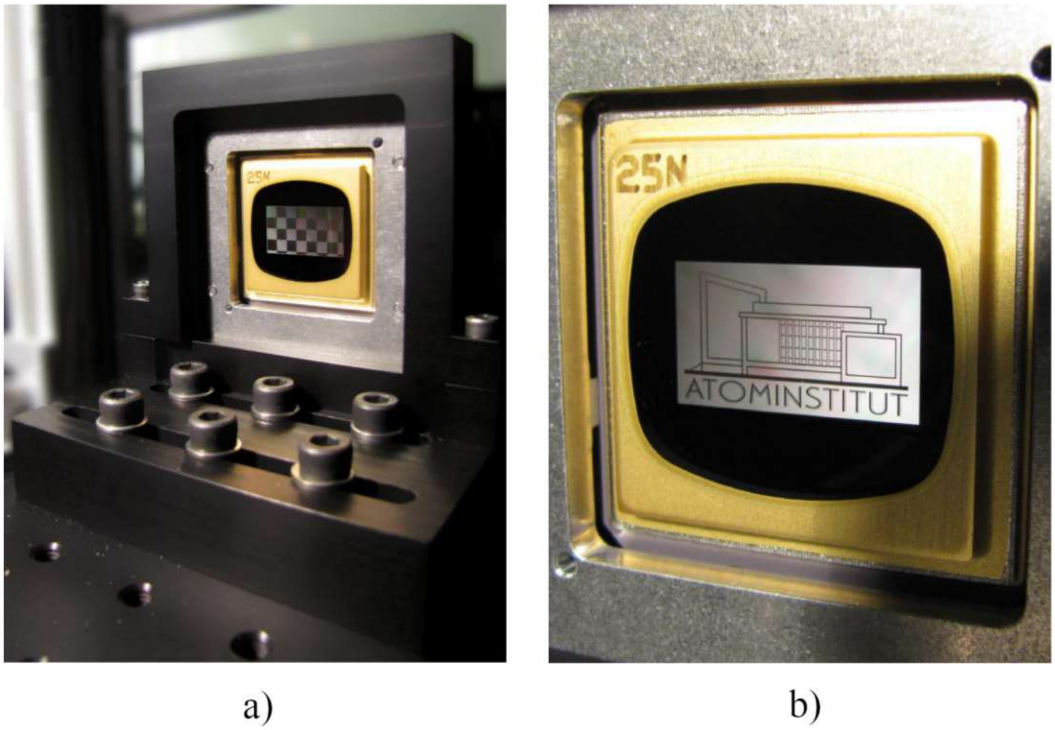

a) b)

Figure 3.4: **Digital Micromirror Device (DMD):** An example of the DMD showing a) a checkers pattern and b) the logo of the Atominstitut. The reflected light intensity will have the shape of the ON pixels (white in the figure). Figure adapted from [63]

$$\Gamma_{sc}(r) = \frac{\pi c^2 \Gamma^2}{2\hbar\omega_0^3}\left(\frac{1}{\Delta_{D_1}^2} + \frac{2}{\Delta_{D_2}^2}\right) I(r). \tag{3.5}$$

It is now clear that $\Gamma_{sc}/U_{dip} \propto \Delta^{-1}$, meaning that larger detunings (together with high intensities) reduce scattering. In our experiment, we use blue-detuned 660nm light which has the additional advantage of reducing scattering further, since in blue-detuned traps the atoms tend to sit in regions of reduced intensity. Being far detuned leads to $U_{dip}/\hbar \sim 2\pi \times 1\,\text{kHz}$, making the scattering length $\sim 2\pi \times 0.1\,\text{mHz}$. This results in one spontaneous scattering per second, for an ensamble of 10^4 atoms, causing negligible atom loss and heating [73] .

3.4 Arbitrary 1D potentials

3.4.1 Digital Micromirror Device (DMD)

To create box-like potentials and implement the operations described in chapter 4, we need to spatially shape the light used in the dipole trap. For this kind of task, devices known as Spatial Light Modulators (SLM) are used. There are several categories of these devices, in our case we use a Digital Micromirror Device (DMD).

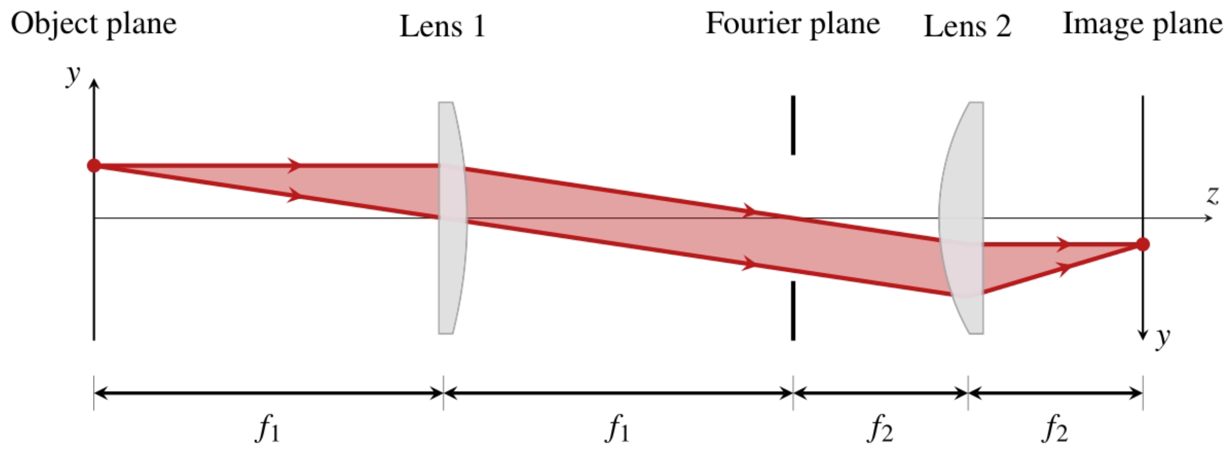

Figure 3.5: **Scheme of a 4f-lens system.** Since $f_1 > f_2$, it is a demagnifying system. The slit, represented by the two vertical black lines, is placed in the Fourrier plane and is used to filter Fourier modes. The second lens does the inverse Fourier transform and builds back the inverted image in the image plane. The propagation plane are x (not shown) and y, while the beam's propagation direction is z.

A DMD is a two-dimensional array of individual pixels where each pixel is an addressable micromirror. Every and each pixel has two possible stable mechanical states, "ON" and "OFF". When in the ON state, the pixel reflects the incident light to a pre-designed path, while in the OFF state, the pixel reflects the light out of the path towards an irrelevant direction. Specifically in our experiment, we use a DLP9500 DMD from Texas Instruments. This device (see figure 3.4) has a resolution of 1920 × 1080 pixels (FullHD), each pixel with an area of $10.8 \times 10.8\,\mu\mathrm{m}^2$. It offers full controllability, meaning that displayed images that use the whole array of pixels, can be changed at a rate of 18 kHz. Instead of using the total amount of available pixels, we use an area of interest (AOI) of 1920 × 200 pixels, which enables a refresh rate of 46 kHz. Since this refresh rate is much faster than the time scale of the atoms (in the order of milliseconds), the DMD delivers enough time resolution for the implementation of time-dependent potentials.

Because the pixels have only two states, the patterns produced by the DMD are binary, which makes impossible the creation of grayscale patterns. However, these can be achieved by applying spatial filtering. The DMD is part of an optical setup which is divided in three different parts. The first part prepares the beam's shape and polarization before being modulated by the DMD. The second part serves as the first demagnification stage and a spatial filter. The third part comprises a second demagnification stage which sets the beam in the path to the atoms inside the vacuum chamber. We will focus on the details about the second part only, to describe how grayscales are achieved with the DMD. The details about the remaining parts are available in [63].

The fact that the DMD mirrors only have binary states allows the generation of binary patterns only, if used alone. However, grayscales can be achieved by filtering some modes in Fourier space. This is done in the experiment with a 4-f imaging system (see figure 3.5).

After being reflected by the DMD, the beam goes through a 4-f imaging system. It consists of two-lens focused imaging system, where the distance between the two lenses is the sum of their focal lengths. Given that the focal lengths are f_1 and f_2, the magnification of the beam going through this system is $m = f_2/f_1$ (see figure 3.5). The biggest advantage of such a setup is that we can select Fourier components by using a mask in the Fourier plane. This mask consists of a simple slit whose opening can be controlled in both x and y directions. By leaving the slit completely open in the x direction and leaving only a small (3 mm) opening on the y direction, we extend the contribution range of the pixels in this direction. The pixels further away from the center of the DMD contribute less while the ones closer to it have a more substantial contribution.

It is also worth mentioning that coherent light is used for the dipole trap. As a consequence of that, interference between the light reflected by each micromirror in the DMD creates interference patterns. Such interference might create unwanted features in the potential. To correct these and other sources of error, an optimization cycle is used to achieve the desired potential. The optimization cycle is described in the next section.

3.4.2 Pattern generation

To determine the effects of the dipole light on the atom cloud, we need to probe the density (see section 3.5) to check what is the effect of the dipole light in the density profile. Since it is not known *a priori* what potential landscape a DMD pattern will create, we need an optimization cycle that consecutively adapts the current patterns, until the effective potential cast upon the atoms is close enough to the desired potential. The feedback information for such an optimization cycle is thus provided by the density profiles obtained from the experiment.

Before starting the optimization procedure, we need to set a target potential V_T. This potential is then used to calculate a target density ρ_T, using the NPSE equation (see equation 2.43). By the end of the optimization process, the measured density profile should match ρ_T up to an error ϵ.

The optimization procedure starts [2] by setting an initial pattern p^0 in the DMD, typically two blocks of pixels playing the role of the box walls. For the i^{th} iteration of the cycle, we measure the density $\rho^i(z_k)$ N times. The average of these profiles $\bar{\rho}^i$ is then compared to the target density $\rho_T(z_k)$ by computing the root mean square error

$$\epsilon^i_{RMS} = \sqrt{\frac{1}{j-l}\sum_{k=j}^{l}\left(\frac{\rho_T(z_k) - \bar{\rho}^i}{\rho_T(z_k)}\right)^2}, \tag{3.6}$$

for a specific region between z_j and z_l.

For each point z_k the optimization algorithm compares the measured density to the target density. If the former is larger than the latter, it will turn on pixels in the DMD column that affects that point in space; if the measured density is lower than $\rho_T(z_k)$, then a pixel is turned off at that position. The details about which and how many pixels are turned on or off to correct the density at a specific point in space vary depending on the optimization stage and won't be discussed here. For a detailed explanation see [73]

---

[2] There is a calibration process taking place before the procedure described here. The details can be found in [73]

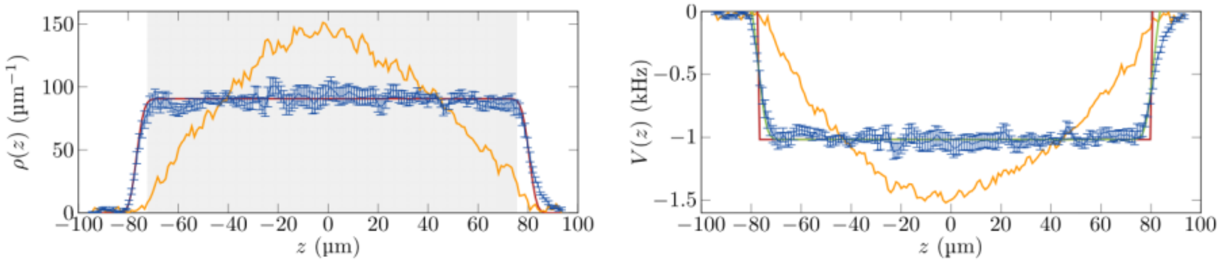

Figure 3.6: **Optimization result for a box with a length $L = 160$µm.** The atomic density and the potential shapes are shown on the right and left figures, respectively. The yellow curve represents the starting point, the red curve indicates the target potential and the blue dots are the final result. The $\epsilon_{\mathrm{RMS}} = 4.4\%$, calculated over the region shaded with gray. Figure adapted from [73].

The procedure described above is repeated until the error of the current cycle is smaller than ϵ_{RMS}. An example of an optimized potential and the correspondent density profile is shown in figure 3.6. Typically, a full optimization procedure whose $\epsilon_{RMS} < 10\%$ lasts about two hours.

The optimization of time-dependent potentials is technically possible, however infeasible. It would require optimizing a potential for each time instant for a procedure that could take up to 50ms. Instead, we take a simpler approach which interpolates intermediate patterns by linearly changing a parameter of the potential (length of a box, for example). This process is explained in more detail in chapter 4.

However, there's an alternative approach which might be more efficient. Using Optimal Control Theory (OCT), it might be possible not only to optimize a single potential more efficient, but also to generate dynamic potentials using less resources and finding shortcuts to adiabaticity [74, 75]. This approach is still under development.

3.4.3 Longitudinal double well

Shaping the potential landscape as described in this section applies only to the longitudinal (enlongated) direction. The remaining directions are frozen and are not to be meddled with. In chapters 5 and 6 we will present experimental results that rely on the use of the double well potential in the longitudinal direction. This potential double well is not to be mistaken with the atomchip double well described in section 2.2.

Figure 3.7 illustrates clearly each of the trap geometries separately and together. The atomchip double well introduced in section 2.2 is generated by manipulating the current sent to the atom chip wires. Its purpose is to create two identical atom clouds to allow the probing of the relative phase field. The phase field is extracted through the matter-wave interference resulting from the expanding clouds during the free fall (section 3.5).

The double well in the longitudinal direction, mainly described in chapters 5 and 6, is created with the DMD by shining light at the center of a box potential (similar to the one in figure 3.6) to create a local barrier that separates the two halves of the bigger box. This manipulation of the longitudinal potential will be crucial to study some of the processes described in the following chapters.

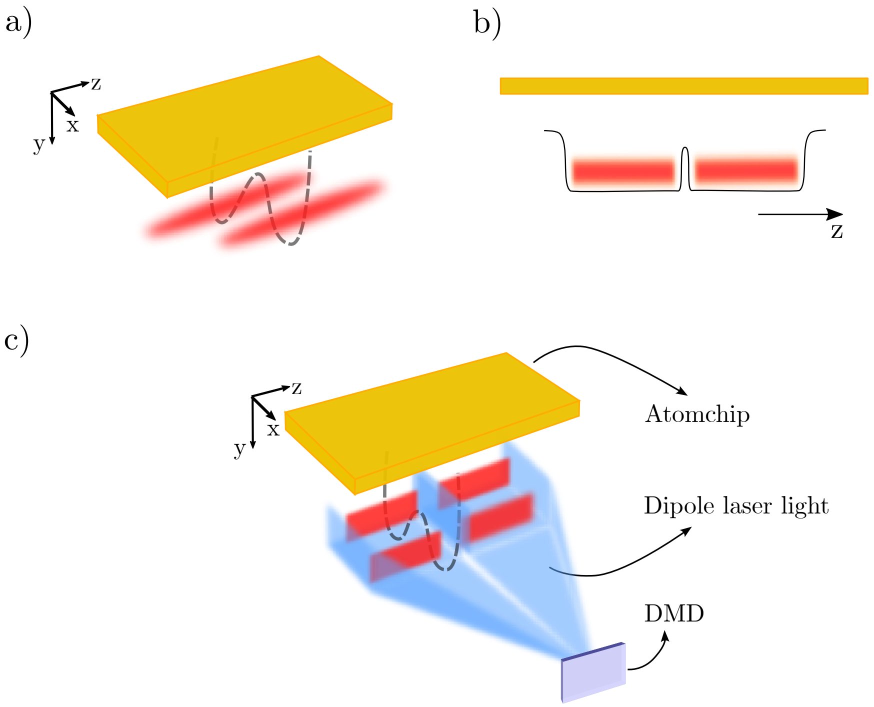

Figure 3.7: **Trap geometries from the atomchip and dipole trap:** The atomchip produces a magnetic trap which can take the shape of a double well as shown in a). The longitudinal potential can be shaped arbitrarily as shown in b). In this example, we created a barrier to separate the two halves of the big box. The scheme in c) shows both traps used simultaneously. Each cigar shaped cloud is independent and the dipole light influences them in the same way. The experiments are performed in the atomchip double well to allow the measurement of the relative phase.

To summarize, the two different kinds of double wells are used simultaneously but with independent and distinct purposes. The atomchip double well is needed to extract the relative phase field. The two atom clouds are independent and are affected by the dipole trap light in the same way. The double well described in the next chapters results from a manipulation of the longitudinal direction performed with the DMD-shaped light from the dipole trap. It aims at inducing dynamics to study the evolution of an out-of-equilibrium system. For simplicity, we refer only the longitudinal potential landscape from chapter 4.

3.5 Probing

There are a plethora of techniques to probe atom densities in cold atoms systems [76]. In our experiment we chose absorption imaging because of its easier and straight forward implementation. As discussed in section 3.5.2, this method uses resonant light which is absorbed by the atoms. Counting the number of absorbed photons gives a measure of the cloud's density distribution. In our experiment, probing is done by releasing the atoms from all the active traps. After the traps are turned off, the atom cloud falls with gravity and expands mainly in the confined directions. After a certain falling time, called time of flight, the resonant imaging light is shined on the atoms and the absorption signal is recorded with a CCD camera. The rest of the section will be dedicated to explain the details of this probing method along with its undesirable effects.

In section 3.5.1, we take a look at how the time of flight expansion affects the wavefunction of the falling cloud. In section 3.5.2, we explain the basics of absorption imaging and characterize each imaging system available in the experiment. The last three sections overview the most used measurement methods for the results presented in this thesis.

3.5.1 Expansion in time of flight (TOF)

When the traps are turned off, the atoms fall with gravity. When a cloud falls, it expands rapidly in the tightly confined directions before being imaged, during a period called the Time of Flight (TOF).

We use different TOFs for different imaging systems. For different TOFs, the imaged density will have expanded different amounts. Thus, it is important to understand how the TOF affects the wavefunction of the system. We can start by assuming that the condensates in well 1 and 2 after TOF t are described by the fields

$$\Psi_{1,2}(\vec{r},t) = \phi_{1,2}(x,y,t)\psi_{1,2}(z,t). \tag{3.7}$$

Due to the very tightly confined directions, the relevant expansion takes place in the transverse directions [77], we focus on the radial part of the wavefunction $\phi_{1,2}(x,y,t)$ and assume it to be the ground state of the harmonic oscillator [49]

$$\phi_{1,2}(x,y,t) = \exp\left(-\frac{(x^2+y^2)}{2a_\perp^2 - i\frac{2\hbar}{m}t}\right) = \exp\left(-\frac{(x^2+y^2)}{2\sigma_t^2}\right)\cdot\exp\left(i\frac{\hbar t(x^2+y^2)}{2ma_\perp^2\sigma_t^2}\right) \tag{3.8}$$

where $a_\perp$ is the harmonic oscillator length, introduced above and $\sigma_t^2 = a_\perp^2 + \left(\frac{\hbar t}{ma_\perp}\right)$.

Notice that this calculations don't consider interactions, which can be important (see section 2.3.1). To understand the role of interactions, a numerical study of the GPE was done in [40]. All the energy from interactions is transformed in kinetic energy in about 0.5 ms, meaning that even for the smallest time of flight used in the experiment ($t = 2$ ms) the transverse direction is much larger than what it was *in situ*.

To model the expansion considering the interactions, we assume that the wavefunction has a Gaussian shape at all times and reformulate the time dependent width σ_t to explicitly include the broadening,

$$\sigma_{t,n}^2 = \left[a_\perp^2 + \left(\frac{\hbar t}{ma_\perp}\right)\right]\sqrt{1+2a_\perp n_{1D}}. \tag{3.9}$$

Regarding the non-confined direction, we can consider the expansion to be negligible longitudinally. The hydrodynamic expansion takes place in time scales of $1/\omega_\perp$, too short to affect dynamics in length scales we can measure. Thus, interactions can be neglected and expansion considered ballistic. As a consequence, features present in the measured density can be connected to properties of the trapped system. For the box trap, if $t_{\mathrm{TOF}} \ll L/c\pi$ then there are no significant changes from the in situ density distribution. For typical box traps used in this thesis $L/c\pi \simeq 16$ ms, much longer than the 2 ms TOF used to probe densities "in situ" [3].

Finally, let us look at the case where we have two parallel condensates in the double well. As we will see, the expansion of two parallel clouds leads to matter-wave interference, producing interference patterns which can be used to extract information about the system (see section 2.2.2). Taking the $\Psi_i(\vec{r}, t)$ operators introduced above, we can write the density of both clouds as

$$\begin{aligned} n(\vec{r}) &= |\Psi_1(\vec{r}) + \Psi_2(\vec{r})|^2 \\ &= |\psi_1(z)|^2 |\phi_1(x,y)|^2 + |\psi_2(z)|^2 |\phi_2(x,y)|^2 + 2\,\mathrm{Re}[\psi_1^*(z)\psi_2(z)\phi_1^*(x,y)\phi_2(x,y)] \\ &\propto e^{\frac{x^2+y^2}{\sigma_t^2}} \left[|\psi_1(z)|^2 + |\psi_2(z)|^2 + 2\,\mathrm{Re}[\psi_1^*(z)\psi_2(z) e^{-i\frac{md}{\hbar t_{\mathrm{TOF}}}x} \right] \\ &\propto e^{\frac{x^2+y^2}{\sigma_t^2}} \left[n_1(\vec{r}) + n_2(\vec{r}) + \sqrt{n_1(z) n_2(z)} \cos\left(\theta_1(z) - \theta_2(z) + \frac{md}{\hbar t_{\mathrm{TOF}}} x \right) \right]. \end{aligned} \tag{3.10}$$

The cross terms in equation 3.10 leads to an interference along the x-direction whose phase depends on the distance d between the condensates and their phase difference $\phi(z) = \theta_1(z) - \theta_2(z)$. We took the limit of $\sigma_t \gg a_\perp$ such that $\sigma_t \simeq \frac{\hbar t}{m a_\perp}$. For this approximation to be valid, we need a big time of flight, typically $t_{\mathrm{TOF}} = 15.6$ ms is used. The fringe spacing λ_{fs} is given by the second term in the cosine

$$\lambda_{fs} = \frac{2\pi\hbar t_{\mathrm{TOF}}}{md} \tag{3.11}$$

This interference pattern allows for the measurement of the *in situ* phase field, which is crucial to characterize the dynamic processes presented in this work (see chapter 6). Notice that the broadening from interactions affects the size of the entire pattern but not the interference itself.

3.5.2 Absorption imaging

Absorption imaging [76, 78] consists in illuminating the atoms with a resonant laser beam and imaging the shadow cast by the atoms onto a CCD camera. From the picture collected by the camera, it is possible to measure the distribution of the atomic density. This is done by comparing the intensity I_0 of the incoming beam and the (lower) intensity I measured when the light is absorbed by the atoms. Considering, without loss of generality, that the atoms are imaged along the z direction, we have, for a two level system,

$$\ln\left(\frac{I_0(x,y)}{I(x,y)}\right) + \frac{I_0(x,y) - I(x,y)}{I_{sat}} = \sigma\tilde{\rho}(x,y), \tag{3.12}$$

---

[3] The densities we image are never really *in situ*. We make this abuse of language by calling *in situ* pictures the ones we image with 2 ms (very small) time of flight

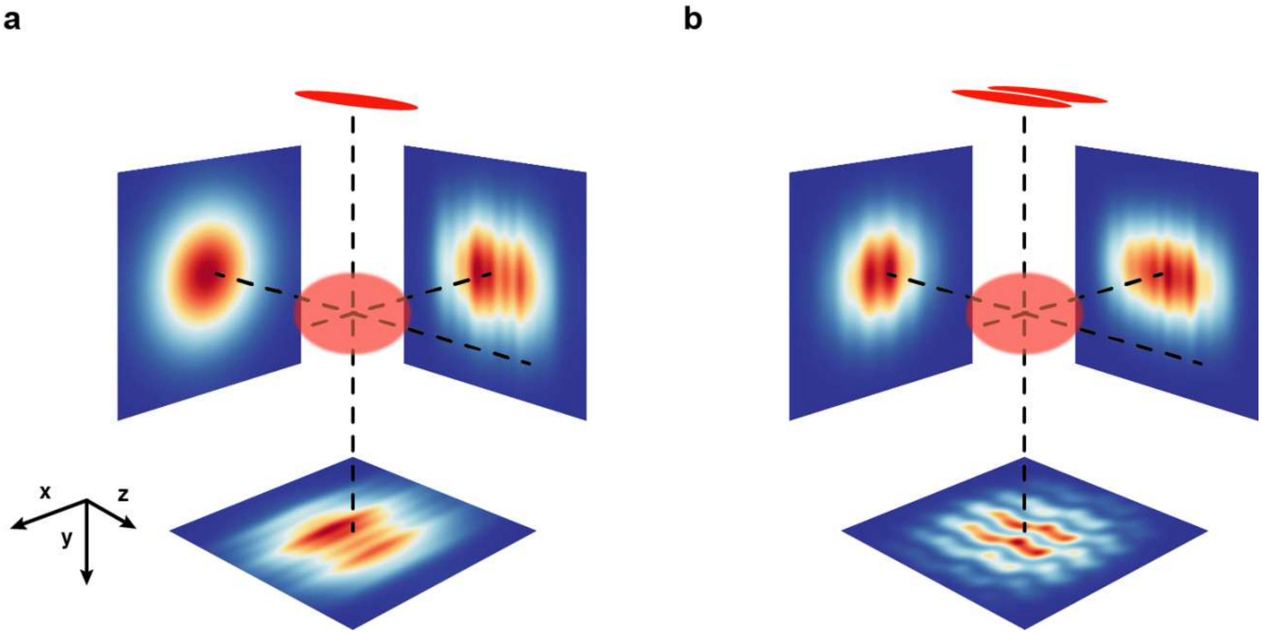

Figure 3.8: **Scheme of the three imaging systems:** a) single well and b) double well configuration. the thin and red shapes at the top represent the atom cloud in situ, while the light red oval below represents the expanded cloud after time of flight. For each imaging direction, we see the integrated density profile captured by the cameras. In the double well configuration, imaging in the vertical direction allows the probing of the interfered density pattern. Figure reproduced with permission from [40].

where σ is the absorption cross-section, $\tilde{\rho}(x, y)$ is the atomic density integrated in the z direction and I_{sat} denotes the saturation intensity. Notice that we assumed that the populations of the ground and excited state are in equilibrium and that the beam intensity doesn't change, otherwise equation 3.12 is not valid. The intensity $I_0(x, y)$ is obtained by taking a picture without the atoms.

In our experiment we have absorption imaging systems for each and every spatial dimension as depicted in figure 3.8.

Each imaging system aims to obtain different information from the atom cloud. For example, the longitudinal imaging system is used to check the atom number balance in the double well, the transversal imaging system can probe the density *in situ* and the vertical imaging system is used to access the interference pattern of the two expanding clouds, from where the relative phase of the two can be extracted. A more detailed description for the imaging system in each direction is provided below. For an even deeper analysis check [59,79].

It is necessary to point out that there will be many undesired effects preventing a perfect image. Besides the typical limitations due to diffraction, we have the fact that the atom cloud is often larger than the depth of field of the imaging system used. On top of that, inhomogeinities on the imaging intensity reduce the cross section between the laser beam and the atoms up to 20%. Recoil blurring, the phenomena of the image getting blurred due to absorbed imaging photons that are re-emmited, has to be considered as well when characterizing each imaging system. All unwanted effects are discussed in [79]. The values used in the next section to describe the imaging systems should then be taken as effective, considering most of the effects mentioned above.

Transverse imaging system

The transverse imaging system images the atoms in the x direction, perpendicular to gravity's direction and the enlogated direction of the atom cloud (check figure 3.8). It uses 30% of the resonance saturation intensity I^0_{sat}, from equation 3.12. The typical TOFs used are 2 ms and 11.2 ms. The former is used to image the density *in situ*, while the latter is mainly used to perform Density Ripples thermometry (see section 3.5.3 and [80, 81]). It should be pointed out that this imaging system has a high resolution objective with a numerical apperture (NA) of 0.20 and a two lens telephoto on the image side. Together, these magnify the image of the atom cloud by a factor of 12.4 onto a CCD camera (Andor DV435-BV-958). The pixel size in object space is 1.05 µm and the field of view ranges an area of 1.07mm × 0.72mm, which allows TOFs up to 12 ms. For typical densities and cloud geometries, and standard imaging parameters, we measure a spot size of $\sigma_{\mathrm{psf}} \simeq 2.8\mu\mathrm{m}$.

For 2ms TOF, the imaging beam is reflected on the atomchip, under an angle of two degrees [49]. The reflection of the beam on the chip creates a standing wave where the atom cloud is located. Besides this, it also creates an additional virtual image. Both of this effects have to be accounted for and make the analysis of the image more complex [78].

Longitudinal imaging system

The longitudinal imaging system is aligned with the weakly confined trap axis. Therefore, the enlongated direction is integrated out and the resulting picture shows the density of the condensate in the xy-plane. If the double-well trap is used, the interference of the clouds in the longitudinal direction can be observed (see figure 3.8).

This imaging system consists of two doublet lenses and a CCD camera (Andor DV 435-BV-958). The magnification of 5.3 leads to a pixel size of 2.45mm in object space. The field of view spans 2.5mm × 1.67mm which allows up to ∼ 18ms for time of flight.

This kind of measurement is not particularly relevant for the results presented in this thesis. It is mainly used to make sure that the two clouds in the double well have an equal number of atoms. This is important to avoid coupling between the relative and common degrees of freedom as discussed in section 2.2.1 .

Vertical imaging system

The vertical imaging system is (nearly) aligned with gravity's direction, imaging the atoms below the chip (y-axis). As with the Transverse imaging system, the imaging beam used here has to be reflected on the chip. However, if the imaging beam is perfectly aligned with gravity, then the unfocused virtual image will obstruct the real image. To avoid this, we focus the imaging light close to the atomcloud and make sure that the atoms only interact with the beam which is reflected from the chip. This way we can have access to the real image of the atoms while maintaining an almost perfect alignment with the y direction.

When the single well is used, we obtain a picture similar to the one measured with the vertical imaging system (see figure 3.8), where the density ripples can be observed. However, if we use the double well configuration, this imaging system allows the measurement of the interference patterns created by the parallel expanding clouds.

We use a single doublet objective lens and a two lens telephoto combination that prepare the imaging light to be captured by the CCD camera (Andor iXon DV887DCS-BV). The magnification of 8.22 provides a pixel size in object space of 1.95µm, while the field of view spans an area of 1mm × 1mm. Due to the vertical fall of the atoms, the focus needs to be adjusted to the chosen time-of-flight. This has aditional complications due to the astigmatism caused by the small misalignement of the beam with respect to the optical axis. This aberration can, however, be compensated for [40]

3.5.3 Density ripples thermometry

The phase fluctuations *in situ* can be mapped to the density fluctuations of the gas in TOF

The density fluctuations measured in TOF encode the the original thermal or quantum phase fluctuations existing in the cloud before it was released from the trap [80, 81]. To measure these fluctuations, we image the atom cloud with the transverse imaging system in 11.2 ms TOF (see section 3.5.2).

The values for the temperature are obtained by computing and analyzing the two-point density correlation function, frequently called the g_2 function

$$g_2(\delta z) = \frac{\int \langle n(z+\delta z) n(z) \rangle}{\int \langle n(z+\delta z) \rangle \langle n(z) \rangle}, \tag{3.13}$$

where $n(z)$ is the atomic density measured in TOF, integrated over the transversal directions. The average is taken over the experimental realizations of the measurement. Tipically, 100 samples provide reliable results.

To extract a temperature from the g_2 function, reference [80] provides an analytical expression that can be compared directly to the experiment. However, in our calculations we use an alternative method that allows us to account for inhomogeneities in the density profiles and the broadening of the cloud. It consists of producing simulated thermal wavefunctions using the Luttinger Liquid model and propagate them freely for the expansion time t_{TOF}. From these numerically generated wavefunctions, we sample the ripple profiles and convolve them with an effectively gaussian [3] point spread function (PSF). Afterwards, we compute the g_2 using these profiles. Figure 3.9 shows some examples for different temperatures and PSFs. Doing this procedure for different temperatures and values of σ_{PSF}, we can compare them to the experimental profile and find out which "guess" is the best one. Following references [40, 82], we extract λ_T as a fitting parameter, using the contrast (the difference between the maximum and minimum of $g2$).

The experimental shot noise enters in $g_2(0)$ (see figure 3.9). Therefore, we ignore the first point and only points with $\delta z > 0$ are considered for the fit. The minimum of the $g_2(\delta z_{\mathrm{min}})$, used to compute the contrast, is extracted with a third-order polynomial fit closer to the lowest points to compensate for the discrete experimental data. We should also note that this method becomes less precise for higher temperatures, due to the inverse proportionality between T and λ_T. Imprecisions for lower values of λ_T entail larger imprecisions for the temperature.

If we consider the double well configuration, the same ripple patterns are observed. If they are uncoupled (which is the case for the results presented in this thesis), we can consider

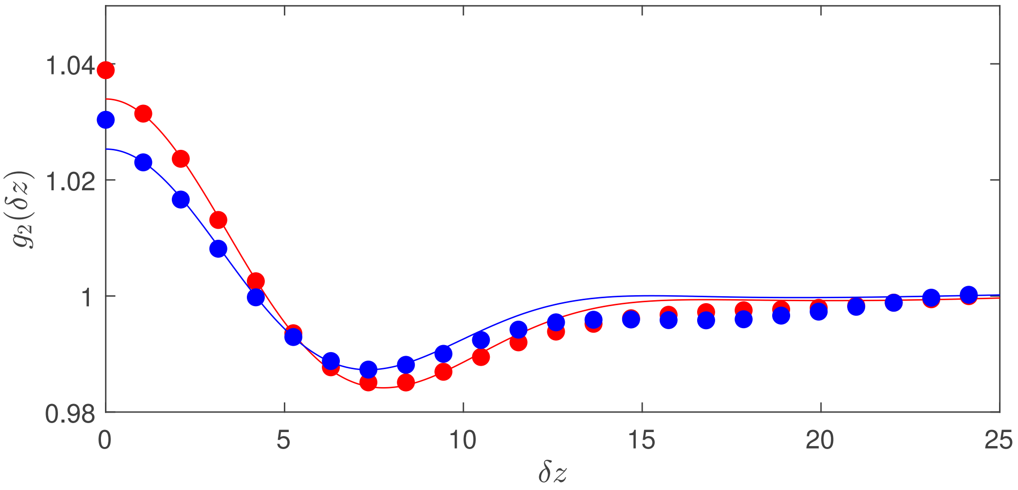

Figure 3.9: g_2 function for 35 nK (blue) and 74 nK (red) in a box potential. The circles are experimental data points, while the continuous lines are the fits from which λ_T is extracted. The atom numbers are 10521 for the colder condensate and 11754 for the hotter one.

that the imaged density fluctuations result from an incoherent sum of the patterns of each condensate. In this case the correlation function in the double well trap g_2^{DW} relates to that of a single well as

$$g_2^{\mathrm{DW}} = \frac{1}{2} + \frac{g_2}{2}, \tag{3.14}$$

meaning that the temperature obtained for the double well configuration is the same for a single well divided by a factor of two. For a derivation of the previous result see [79].

3.5.4 Relative phase measurement

It was mentioned in section 3.5.2 that the vertical imaging system can probe the interference pattern of two parallel expanding quasi-condensates. This intereference pattern depends on the relative phase $\phi(z) = \theta_1(z) - \theta_2(z)$, as shown in equation 3.10. It is thus possible to extract the relative phase profile from the intereference pictures.

To do that, we fit each row of pixels of the interference picture with a cosine modulated Gaussian, given by the function

$$f(x) = ae^{-\frac{(x-b)^2}{2c^2}} \cdot d\cos\left(2\pi\frac{x-b}{\lambda_{\mathrm{fs}}} + \phi\right), \tag{3.15}$$

where a is the contrast of the interference, d is the contrast and ϕ is the relative phase. These are the free parameters. The fringe spacing λ_{fs} and the center of the Gaussian b are fixed parameters.

Doing this for every point in the z direction, we can extract the relative phase field $\phi(z)$. This allows the computation of correlation functions which can be used to infer properties of the system (e.g. temperature) and study its dynamics [21, 83, 84]. This will be particularly important in chapter 6, where we perform local thermometry based on the decay of the correlation function $C(z)$ introduced in section 2.2.2. Thus, we should take into account the limited imaging resolution. To do so, we consider a gaussian PSF with a standard deviation σ_{psf} and account for that in the calculations, obtaining

$$C(\bar{z}, \sigma_{\mathrm{psf}}) = \exp\left[\int_0^\infty \frac{\mathrm{d}k}{\pi} \langle |\phi_k|^2 \rangle e^{-k^2\sigma_{\mathrm{psf}}^2} (1 - \cos(k\bar{z}))\right]. \tag{3.16}$$

As before, we replace the phase mode amplitudes with their thermal expectation value. Considering two uncoupled quasi-condensates, we obtain

$$C(\bar{z}, \sigma_{\mathrm{psf}}) = \exp\left[-\frac{2\bar{z}}{\lambda_T}\left(\mathrm{erf}\left(\frac{\bar{z}}{2\sigma_{\mathrm{psf}}}\right) + \frac{2\sigma_{\mathrm{psf}}}{\bar{z}\sqrt{\pi}}\left(e^{-\left(\frac{\bar{z}}{\sigma_{\mathrm{psf}}}\right)} - 1\right)\right)\right]. \tag{3.17}$$

To minimize the width of the PSF, the atom cloud should be as close as possible to the focus of the vertical imaging system. We estimate a $\sigma_{\mathrm{psf}} = 3$µm after optimizing the focus with the process described in reference [40].

Chapter 4

The Quantum Field Machine (QFM)

In this chapter, we propose a blueprint for a quantum field machine (QFM) first conceived in [9], with our system of choice being quasi-Bose-Einstein condensates in one dimension. The model of QFM we propose intends precisely to address all of the challenges posed when building genuine quantum machines: *i)* It is a genuine complex quantum many-body system, describable by means of effective quantum field theories that capture emergent degrees of freedom using different scales of refinement in the field theory model. In this particular work we focus on a QFM tuned on a Gaussian regime which is efficiently simulated numerically [85] and is also a very good approximation for moderately short time scales; *ii)* It offers potential new tools for quantum liquids and gases, e.g., by providing an additional stage of cooling, which does not involve diluting the system and can be applied after the use of existing techniques; *iii)* The available degrees of controllability makes it possible to exploit strong correlations and coherences for probing quantum effects. This is achieved by steering the functioning of the machine by our understanding of the physics of the system, instead of controlling individual degrees of freedom.

4.1 A new type of QFM

A quantum thermal machine can be constructed by choosing few suitable building blocks and applying some operations on them in a cyclic fashion, forming a thermodynamic cycle. For instance, as illustrated in figure 4.1 it is instructive to consider a quantum thermal machine consisting of three elements, of which two are thermal baths, while the third is a piston shuttling between them. With these components it is possible, e.g., to run a heat engine, by allowing heat to be transferred from the hot bath to the cold one, while work can be extracted from the piston. If quantum fluctuations play a significant role, the process of work extraction would have to be investigated in a framework compatible with quantum mechanics. In case that the individual objects are small and they feature large energy fluctuations, the systems may exhibit complex out-of-equilibrium dynamics during the operation of the cycle. As another example, if instead work is performed from outside, one can construct a heat pump and use the piston to extract heat from one part of the machine and dispose it into another part: in other words, the machine can operate as a refrigerator.

In order to implement such quantum field machines, we identify a set of general opera-

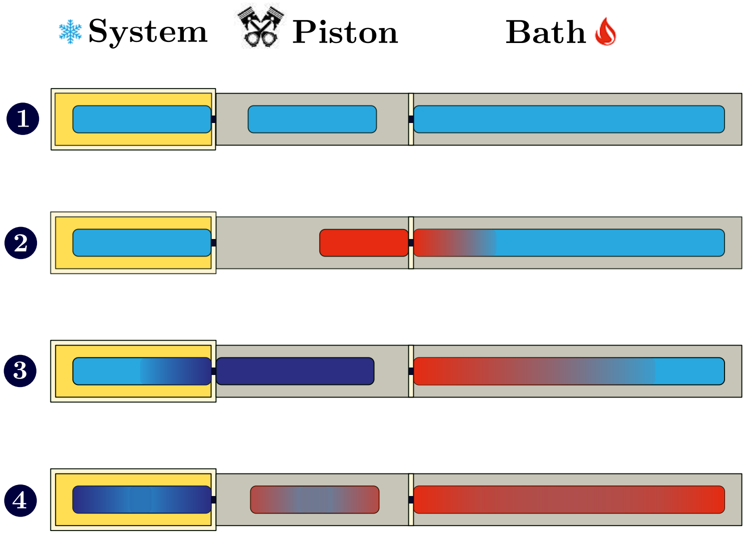

Figure 4.1: **The Quantum field refrigerator**: Similar to canonical ideas employed in ordinary thermal machines, we consider for a quantum many-body system a cycle consisting of a small set of control operations on quantum working fluids, concatenated in order to cool down a part of the machine (referred here as the "system"). This is achieved through a protocol consisting of four steps: 1) Initialization of the system, the piston and the bath at equal temperatures. 2) Compression of the piston and coupling to the bath which receives energy, and decoupling after the heat transfer. 3) Decompression of the piston, therefore decreasing its energy, then coupling to the system thus enabling heat transfer from the system to the piston. 4) Decoupling of the piston from the system and compression to initial size. Through steps 1-4), we expect to achieve a decrease in the system's energy, while the energy of the piston and bath should increase. This increase in energy happens in such a way that the piston and bath can be reused for multiple cycles before they saturate. As we will discuss, all these operations can be implemented experimentally with 1D quasi-condensates, by manipulating them with the beam-shaping techniques described in section 3.4.

tions which will be denominated from now on as quantum thermodynamic primitives (QTPs). These are the basic ingredients for the thermodynamic protocol presented here. The QTPs can be concatenated in a modular fashion to build up the complex range of potential applications that the machine might have. A variety of operations can be conceived, corresponding to different tasks such as activating or deactivating heat flow, injecting or extracting heat from a system, performing or extracting work from a system, moving or shuttling a system around, or suitably adding catalyzing systems [86–88].

In the following sections we introduce two QTPs which will be the building blocks of the proposed thermal machine. In section 4.1.1 we will introduce the QTP that controls the coupling between two longitudinally adjacent atom clouds and will allow the control of energy flow between them. In section 4.1.2 we present the QTPs which implement the compression and expansion of the atom clouds, the equivalent of the piston in a standard thermodynamical cycle. This primitive will allow the creation of temperature gradients and the manipulation of other thermodynamic parameters.

4.1.1 Coupling control between two quasi-condensates: a valve

As depicted in figure 4.1, one of the essential ingredients for operating a QFM is coupling its elements. This will be in general realized by allowing excitations to tunnel through a barrier which allows to control the flow of energy between two parts of a QFM, just as it happens with a valve. When considering a valve of a QFM, we expect to find some differences compared to a similar type of operations in an ordinary thermal machine:

1. Specifically, in classical physics, merging of systems with identical density would be largely featureless. Two quasi-condensates, in sharp contrast, if initially uncorrelated, will have a random phase, and coupling will lead to a random phase gradient which results in creation of additional excitations. In a quantum system, if we do not align the relative phases of the quantum fields, merging adds excitations and entropy. Such quantum phase diffusion [89–92] can, however, be countered by enabling yet another quantum effect which is coherent tunneling through a barrier which leads to phase-locking in an out-of-equilibrium situation [22, 79, 93–96].

2. Conversely, splitting the elements of the QFM – once they have established phase [22,79,93–96] coherence – may introduce quantum noise [21,97] related to the dynamical Casimir effect [98, 99]. In a finite and well controlled system, production of excitations in this process may add an amount of energy which is not negligible.

3. The individual elements are systems which feature correlations extending over sizable lengths and time unlike in ordinary thermal machines. Notably, even at thermal equilibrium a single quasi-condensate has a finite thermal coherence length $\lambda_T \neq 0$ [79, 100] which would not be true if one were to simply set the reduced Planck constant to zero $\hbar \to 0$ entirely disregarding quantum effects.

4. Whenever the elements of the QFM have coherent dynamics then recurrences of evolution may occur as observed in [22]. This, among others, is one of the signatures of the presence of non-Markovian effects in the system. Due to this, concatenation of cycles in the QFM may depend on the precise timing.

Notice that these effects are particularly relevant because we cannot consider the thermodynamic limit for the elements of the QFM as in state-of-the-art experiments it is not possible to create thermodynamically large ultra-cold gases. As an example, while the amount of energy injected in a local operation should be intensive, its effect may be substantial for the experiment. Another example is the fact that the coherence length in quasi-condensates is comparable to their size.

4.1.2 Rescaling the length of a quasi-condensate

Changing the length of a quasi-condensate induces a change on the internal energy of the gas. Being able to compress or expand the atom clouds allows the creation of temperature gradients between the different components of the QFM. Combining this with the valve introduced previously (section 4.1.1, it can then be used to study heat flow from the piston to the bath, as illustrated in 4.2.3. Once more, it is important to account for the fact that quantum effects come into play, namely,

1. while the energy is changing due to compression or decompression the piston may go out of thermal equilibrium, e.g., due to squeezing of internal modes [85,99]. If this quantum feature will influence thermodynamic transformations involved in the operation of a thermal machine, then such a machine will have richer physics compared to a standard one. Hence understanding the performance limits of such potential machines must be done by a thermodynamic framework including this non-classical effect.

2. Internal dynamics in our system occurs within time scales comparable to timings of individual steps of the cycles considered. In contrast for classical thermal machines the internal and cycle time scales are perfectly separated.

3. The piston can be modeled by considering a moving boundary which is also closely related to the dynamical Casimir effect [99].

4.2 Numerical implementation

As sketched in Fig. 4.1 above, using the piston and the valve as fundamental building blocks of a QFM allows to construct a refrigeration cycle. In this section, we will present results on the numerical modeling of the individual QTPs involved.

Each QTP proposed here is modeled by a TLL Hamiltonian described in section 2.1.2, which allows us to simulate the dynamics of phonons and to calculate the corresponding energy changes in the system. As the model is a quadratic Hamiltonian, our simulations are done within the Gaussian framework and are computationally efficient even when evaluating sophisticated measures from quantum information theory such as the relative entropy. Our focus will be to introduce and define the primitives, while emphasizing their physical meaning and generality. The latter is crucial as it should be clear that all QTPs that we present are independent of our modeling – qualitatively they represent robust quantum thermodynamic operations, and the quantitative details should depend only on the specific implementation. In the specific context of this work, the proposed implementation of such QTPs is done having in mind the experimental setup described in Chapter 3. The parameters used in the simulations, as well as the time and length scales, were chosen to match as close as possible the ones usually used in the experiment.

The next two sections describe the numeric implementations of the QTPs introduced in section 4.1. Section 4.2.3 shows how the QTPs can be used to observe heat flow between the piston and the bath and section 4.2.4 gives an example of how to achieve cooling by performing the QTPs cyclically.

4.2.1 An energy valve

Here, we consider a simple model, where two quasi-condensates can be coupled via a small buffer region. Specifically, we will consider a bipartite system A and B, each part being initially thermal and essentially homogeneous, the two parts being separated by a buffer region of negligible size $l \simeq \xi_h$ so that phonons cannot tunnel.

The TLL Hamiltonian discussed in section 2.1.2 is used to model the valve. We specify a GP profile of two adjacent uncoupled boxes which smoothen at the edges, as shown in figure 4.2 a). Denoting by ρ_0^A and ρ_0^B the GP profiles of the systems in the left and the right, respectively, the initial Hamiltonian of the two independent systems reads

$$\hat{H}_{A|B} = \hat{H}[\rho_0^A] + \hat{H}[\rho_0^B], \tag{4.1}$$

where the tiny separation at the interface is modeled by having four Neumann boundary conditions (introduced in section 2.1.2) in the Hamiltonian $\hat{H}_{A|B}$, two at the edges and two at the barrier location.

We then define the joint system to have a GP profile

$$\rho_0^{AB}(z) = \begin{cases} \rho_0^A(z), & z \in A \\ \rho_0^B(z), & z \in B, \end{cases} \tag{4.2}$$

implementing the "gluing" of the profiles. With this, we can take the final Hamiltonian of the merged systems to be

$$\hat{H}_{AB} = \hat{H}[\rho_0^{AB}] = \hat{H}_{A|B} + \hat{H}_{int}, \tag{4.3}$$

where now we have only two Neumann boundary conditions, one for each wall, and an interacting part between both systems (for details on $\hat{H}_{int}$, see). It should be mentioned that the buffer region was ignored in the simulations. This is based on the assumption that in the experiment it will be small enough and the experimental removal of this buffer region is negligible for the dynamics. As we will see in chapter 6, this is not always the case. Nonetheless, the results the simulations yield are accurate enough that the important part of the dynamics is captured.

Note that to merge the two systems, we need to eliminate two of the four initial boundary conditions. To do this, we interpolate linearly from the uncoupled Hamiltonian $\hat{H}_{A|B}$ to the coupled Hamiltonian $\hat{H}_{AB}$ in time t_{merge} as described by the following time-dependent Hamiltonian

$$\hat{H}_{A-B}(t) = \left(1 - \frac{t}{t_{\text{merge}}}\right)\hat{H}_{A|B} + \frac{t}{t_{\text{merge}}}\hat{H}_{AB}, \tag{4.4}$$

with $t \in [0, t_{\text{merge}}]$. The linear interpolation describes the external potential smoothly being changed to couple both densities [1] .

In order to study the dynamics of merging two quasi-condensates, we consider initial conditions that are typical for the experiment used in this thesis. For this simulation, we use two independent thermal atom clouds at temperatures $T_A = T_B = 50$ nK. The thermal states are defined as

$$\hat{\rho}[\hat{H}] := \frac{e^{-\frac{\hat{H}}{k_B T}}}{\mathcal{Z}}, \tag{4.5}$$

where $\mathcal{Z} = \operatorname{Tr}\left(e^{-\frac{\hat{H}}{k_B T}}\right)$ is the partition function. In this specific simulation, $\hat{H}$ will be the Hamiltonian (2.45) for each system individually. Both quasi-condensates have the same density $\rho_0^A = \rho_0^B = 100$ atoms/µm and falling off towards a smaller value at the edges (see

---

[1] As it can be seen in Appendix C of [29] , the mixing of boundary conditions is well defined.

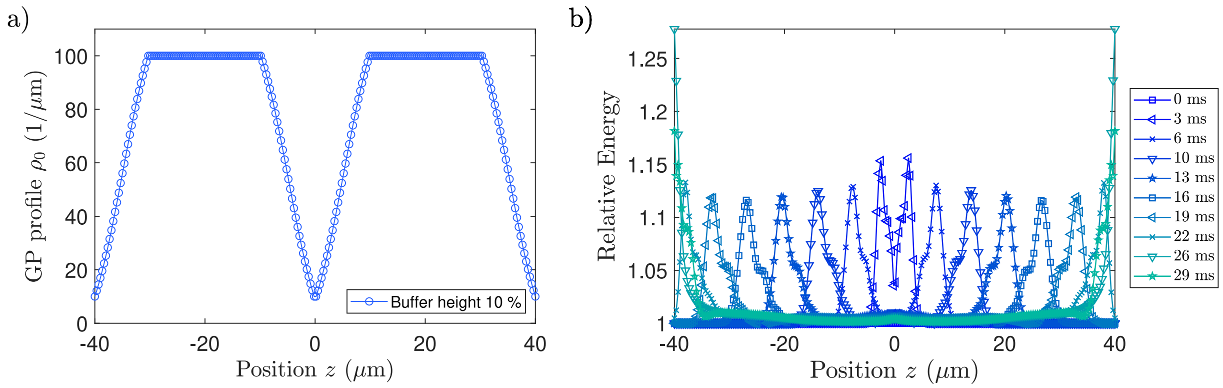

Figure 4.2: Operating a valve between two identical and independent thermal quasi-condensates. *(a): GP profiles:* We consider two quasi-condensates which are homogeneous in the bulk but their density falls off towards zero at their edges. At position $z = 0$ there is initially the boundary condition that in our effective model at a single point implements the separation between the two systems. As the systems become coupled, the energy can tunnel between the two systems through this point. Throughout on line plots of real-space quantities bullets indicate the discretization lattice used in the simulation while the continuous lines are merely a guide to the eye. (b): Dynamics of energy density. We plot $\mathrm{d}E(z)/\mathrm{d}z$ defined in Eq. (6) for different times during the coupling of two quasi-condensates. Initially, the energy density in each quasi-condensate is uniform, and we use that value to normalize the plotted values. During the coupling, localized energy is injected at the interface of the two systems and travels ballistically away in form of wave-packets, which increase the energy density by $\sim 15\%$.

figure 4.2). The density decrease near the boundary conditions is modelled with an error function to account for the finite-sized box walls found in the experiment. The TLL model is solved for this background density.

In figure 4.2 b), we show the numerical results for a linear ramp with merging time $t_{\text{merge}} = 40$ ms. This is a rather long time-scale and it was chosen here to show that the excitations can start returning towards the interface ($z = 0$) if the merging takes a long time. Initially, the energy is distributed homogeneously in each system so we present the energy distribution relative to that value. This relative measure, which will be employed throughout, allows to disregard the cut-off dependent shift coming from zero-point fluctuations. In fact, our effective Hamiltonian is not normal-ordered but rather regularized by the finite healing length $\xi_h = \hbar/(mc)$ in the system (note that the cutoff Δz in our numerical simulations is higher than the healing length). We find that, as anticipated, merging two systems via tunnel coupling induces excitations in form of two counter-propagating wave-packets traveling with the respective speed of sound, which in typical experiments on the Atomchip platform is about $c = 2\,\mu\text{m/ms}$. The simulation predicts that the presence of the wave-packets increases the local energy by quite a sizable amount of about $\sim 15\%$. This may cause system dynamics to deviate from the TLL model. Nevertheless, the higher-order terms that could become relevant in the experiment should have only the effect of dispersing the wave-packets. According to the simulations [2], the amount of injected excitations is higher if the systems are coupled at peak density (see appendix C2 in [29]). The reason for this is that in the lattice approximation we are adding an off-diagonal coupling between the two respective edges of A and B of scaling with time and density $\sim (1 - t/t_{\text{merge}})\rho_0(z = 0)$ and so the merging is "softer" if the density value is lowered at the interface.

It is instructive to analyze the correlations of the coupled state during the merging. As shown in figure 4.3, we find that initially there are no correlations between A and B and hence we see that two independent thermal TLLs are not thermal with respect to the joint Hamiltonian. During the merging the systems become coupled and the established correlations drive the state towards being close to the joint thermal state, see appendix C2 of [29] for more details. Interestingly, after the first traversal time, i.e., when a local excitation at the merging interface has traveled to the edges, the joint system is close to being thermal in the bulk as shown in the inset of 4.3.

In order to check if the merging QTP is intensive we calculate the relative entropy of the state evolving during merging with respect to the thermal state of the coupled Hamiltonian at T = 50nK. Initially, the relative entropy decreases rapidly, reflecting the ongoing thermalization around the interface of the two systems, where the correlations are being established. For the whole system the relative entropy does not reach zero and levels off to a constant value within about 10 ms. This is due to the wave-packets being always present in the system, hence the impossibility for the entire system to be in thermal equilibrium. This is in line with the fact that quadratic Hamiltonians never thermalize, due to the absence of interactions. If we consider the reduced covariance matrix describing only the bulk middle region, we see that around 20 ms the relative entropy drops essentially to zero. This means that once the excitations leave the window of observation, the system left behind agrees, in that region, with the (joint) thermal state. Finally, for longer times the wave-packets come back to the bulk and allow for detecting an out-of-equilibrium component of the state.

4.2.2 Compression and expansion

In this section, we propose a model to describe what happens to phonons when the confining trap (space ocupied by the trap) changes in time. More precisely, we will continuously change the length L of a box-shaped potential, which will induce a change in the GP profile ρ_0. We assume that the total number of atoms $N = \rho_0 L$ is conserved at all times so that

$$\rho_0(t) = \rho_0 \frac{L(0)}{L(t).} \tag{4.6}$$

This time-dependent GP profile assumes that the change in volume is slow, so that a homogeneous system remains homogeneous at all times. Under this assumption, the TLL Hamiltonian will now have a time dependence. Specifically, the integration in Hamiltonian (2.45) is performed over the time dependent length $L(t)$. In the homogeneous case, the

---

[2] The higher modes mentioned here are the ones coming from the quantum pressure term in Hamiltonian (2.11), which is quadratic. Check Chapter 6 for a more thorough discussion considering a Hamiltonian beyond the quadratic approximation.

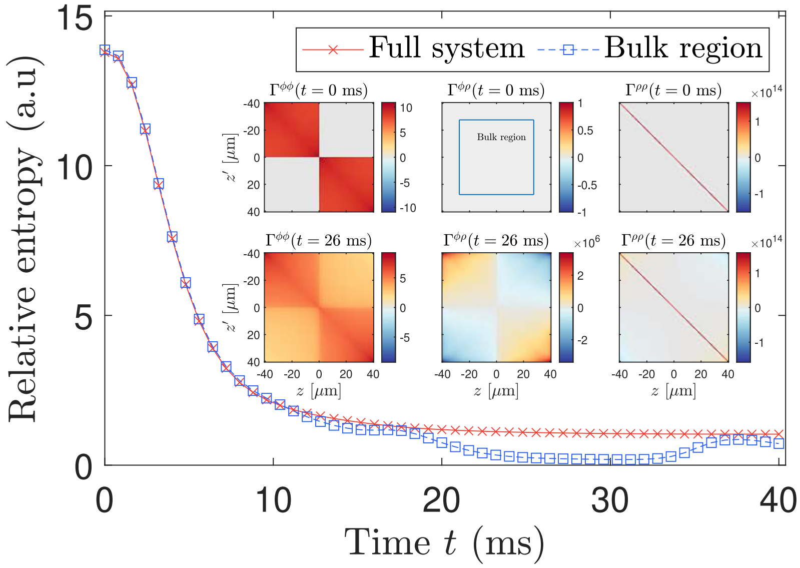

Figure 4.3: Correlations before and after merging. The initial covariance matrix $\Gamma(t=0\text{ms}$ (inset top) is characterized by phase fluctuations $\Gamma^{\phi\phi}=2C^{\phi\phi}$ ranging only over the individual systems, no cross-correlations between phase and density operators $\Gamma^{\phi\rho}\equiv 0$, and density fluctuations $\Gamma^{\rho\rho}=2C^{\rho\rho}$ being essentially diagonal. When heat excitations reach the edges, the covariance matrix $\Gamma(t=26\text{ms}$ (inset bottom) restricted to the bulk region of the system agrees with the thermal covariance matrix of the joint Hamiltonian: phase fluctuations $\Gamma^{\phi\phi}$ become uniform over the joint system, in the bulk of the system crosscorrelations vanish $\Gamma^{\phi\rho}\approx 0$, while density fluctuations $\Gamma^{\rho\rho}$ are diagonal. Quantitatively, we plot the relative entropy ofthe time-dependent covariance matrix with respect to that of the thermal state of the coupled Hamiltonan at $T=50\text{nK}$ and observe that it decreases rapidly over around 10ms. Due to the presence of the heat wave packets, the relative entropy for the full system (red crosses) does not converge to zero over time, while for the covariance matrix restricted to the bulk region (blue squares) again. it essentially vanishes at around t = 26 ms and then increases (for details on how the covariance matrix is calculated, see appendix A).

following change of the integration variable

$$z \to \zeta = z\lambda(t), \quad \lambda(t) = \frac{L(0)}{L(t)} \tag{4.7}$$

allows the time-dependent Hamiltonian to be written as

$$\hat{H}(t) = \int_0^{L(0)} \mathrm{d}\zeta \left[\frac{\hbar^2\lambda^2(t)\rho_0}{2m} (\partial_\zeta \hat{\phi}(\zeta))^2 + \frac{g}{2}\lambda(t)\delta\hat{\nu}^2(\zeta) \right] \tag{4.8}$$

where we have defined a rescaled density fluctuation field $\delta\hat{\nu}=\delta\hat{\rho}/\lambda(t)$ in order to preserve the canonical commutation relations, i.e., $[\delta\hat{\nu}(\zeta),\hat{\phi}(\zeta')]=i\delta(\zeta-\zeta')$. Here we made the integration limits explicit and changed the frame so that the length of the system is effectively constant

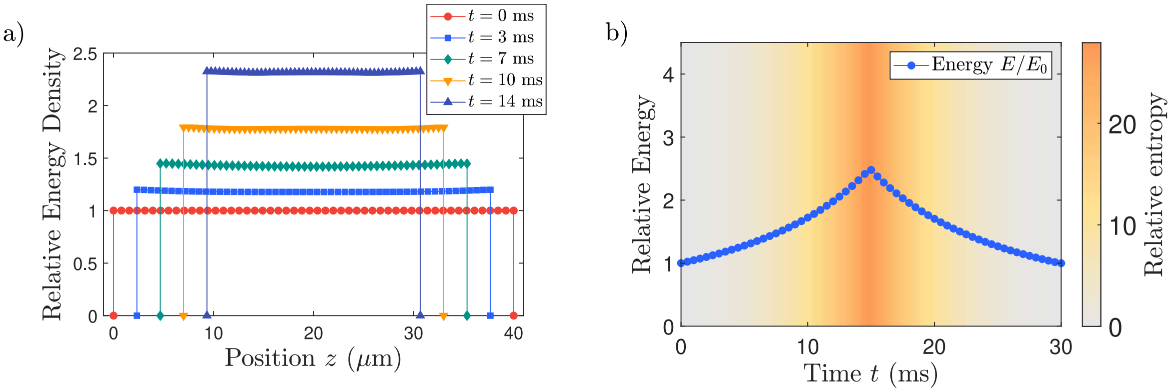

Figure 4.4: Single stroke of a piston. A piston initially thermal and homogeneous and of length 40μm is compressed to half size within 15 ms and then expanded back to the initial length in the same time. *(a):* Energy density during compression. The piston keeps a homogeneous energy density which, however, increases while the length is reduced. *(b):* (Non-)equilibrium properties of piston during the stroke. We plot over time the global energy relative to its initial value (blue dots) and the relative entropy to the closest thermal state as a color gradient during the whole stroke (i.e., compression and decompression). We find that the compression increases the total energy of the system due to increasing pressure of the phononic gas. Furthermore, the piston goes out of equilibrium, as the relative entropy to the closest thermal state also increases during compression. The reverse happens when the piston decompresses. In particular, the piston is again fully thermal at the initial energy and temperature at the end.

but the Hamiltonian density becomes time-dependent due to the dimensionless length ratio $\lambda(t)$.

We observe that if the system stays homogeneous then for all times t the time-dependent Hamiltonians 4.8 share the same momentum-eigenmodes, which will become squeezed. We hence should expect that compressing will have an effect of introducing squeezing of phase and density quadratures in the system, see [99] for a related discussion.

With this model we can simulate the functioning of a piston: In figure 4.4 we show the results of a simulation of a single stroke. We consider a piston in the same initial state as either of the two systems shown in 4.2 before merging. We then compress the system uniformly by half in $t_{\mathrm{comp}} = 15$ ms and then decompress it back to the initial size in the same time. We find that the energy stays essentially homogeneously distributed during the piston stroke, see figure 4.4 (a). It is moreover possible to check whether the piston stays thermal during the compression and decompression. The necessary condition is fulfilled as the energy density is uniform at all times and changes in relation to volume. As shown in figure 4.4 (b) the total energy increases and comes back the initial value during the stroke of the piston. However, a more refined check involving the relative entropy shows that the system is not at thermal equilibrium at all times. At a sequence of times during the evolution we evaluated the relative entropy of the time-dependent state to thermal states with temperatures taken from a certain range. The temperature of the thermal state with the lowest relative entropy

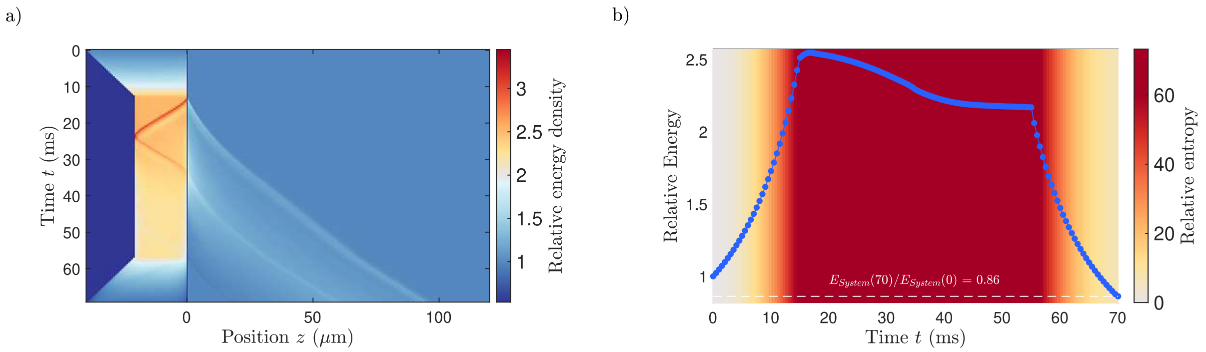

Figure 4.5: Heat flow between the piston and bath. Initially, the piston and bath are two independent condensates, with the bath being 3 times larger in size. The piston on the left is compressed to half of its original size. Then, it is coupled to the piston to the bath at $t = 15$ ms and decoupling starts right after. *(a) Energy density over time.* Energy as a color gradient in a space-time grid. The coupling between the two parts introduces the propagation of wave packets at the speed of sound, which is higher in the piston, due to the higher density resulting from compression. *(b) Energy dynamics in nonequilibrium.* The plot shows the ratio of average energy versus initial energy in the piston over time. We observe that it first increases strongly, while decreasing to a value that is less than 1, just before the piston starts coupling with our system of interest. This is what will allow the system to be cooled with a full Otto cycle. We also plot the relative entropy to the best fit thermal state as a color gradient in the background and observe that during coupling the system goes strongly out of equilibrium, while returning to be close to equilibrium at the end.

gives the effective fit for the temperature. It is clear that if the time-dependent state remains thermal at all times, then there will be a temperature for which the relative entropy vanishes. If the piston is away from thermal equilibrium then the value will be strictly positive. We find that as the energy increases the relative entropy measure shows that the state is pushed away from thermal equilibrium, and comes back to it only when the stroke is finished.

4.2.3 Heat flow between two components

We now can use the compression QTP in order to enable heat flow between two systems. In figure 4.5, we show the steps (1-2) of the Otto cycle that were sketched in figure 4.1, i.e. we compress the piston, couple it to the bath and, after decoupling, decompress it back to its initial state. As before, the piston and bath are both thermal initially and have the same overall shape of the GP profile with the only difference that the bath is three times larger than the piston. As was shown above, coupling two systems with the same temperatures does not lead to heat flow. In order to enable it, we compress the piston using the compression QTP. After the piston is compressed its energy is higher and so is its effective temperature. The bath remains static so there is a temperature difference between the piston and bath which means heat will flow from the piston to the bath. Using the coupling QTP we effectively open the valve between the piston and bath so that heat can flow. After this is completed we split the two systems closing the heat flow valve and decompress the piston to its initial length. This means that the piston has performed a stroke but in its compressed state has released heat to the bath. After it comes back to its initial length it should therefore be colder than it was initially. In figure 4.5 we show the results of this protocol plotting the full spatio-temporal dynamics of the energy density and in figure 4.5 we show that the compressed piston couples to the bath with effectively squeezed modes and the two systems are not at thermal equilibrium while the valve is open. Nevertheless energy in the piston decreases as heat flows into the bath which is also seen in figure 4.5 (a) in form of a light color stripe entering the bath. Finally, we find that the total energy in the piston decreases to a lower value than initially and thus we conclude that the piston has been overall cooled down at the end of this protocol. Interestingly, at the end of the protocol the decompression undoes the squeezing of the modes. The low value of the relative entropy at the end of expansion shows evidence that the piston ends in a state very close to thermal equilibrium.

Summarizing, it should be stressed that we have performed work on the piston which allowed us to enable heat flow and by composing the compression QTP with the open valve QTP we deposited some of the piston's energy into the bath. An experimental demonstration of heat flow is presented in Chapter 6. The experimental procedure for the observation of heat flow is simpler than the procedure described in this section. Nevertheless, we demonstrate the flow of energy from one condensate to the other and explore further important physics regarding non-markovianity that are not captured by the TLL simulation.

4.2.4 Example of a cooling cycle

We now join the QTPs introduced above and the knowledge about the possibility of transferring heat from one component to the other to build a cyclic machine. The idea is to use the three components mentioned in figure 4.1 and apply a set of operations similar to those used in section 4.2.3 to perform cooling on the 'System' component. In more detail, the cycle works as follows:

1. The machine is initialized with a system, a piston and a bath, each at thermal equilibrium.
2. The first non-trivial thermodynamic transformation is the compression of the piston with a subsequent interaction with the bath. The work inserted to compress the piston enables heat flow as described in section 4.2.3.
3. After splitting the piston from the bath, the piston is expanded back to its initial length. This aims to cool it down and when it subsequently interacts with the system it should take up some heat from it.
4. Finally, the piston and system are split again and the cycle can be repeated.

In figure 4.6 we depict the energy changes of these three pieces of the QFM over the duration of the Otto refrigeration protocol obtained from a numerical simulation. It can be seen that the piston first increases its energy due to compression ($t_{comp} = 15$ ms) and then lowers it during interaction with the bath and successive expansion ($t_{merge} + t_{comp} = 35$ ms). Finally, the piston increases again its energy when interacting with the system and then

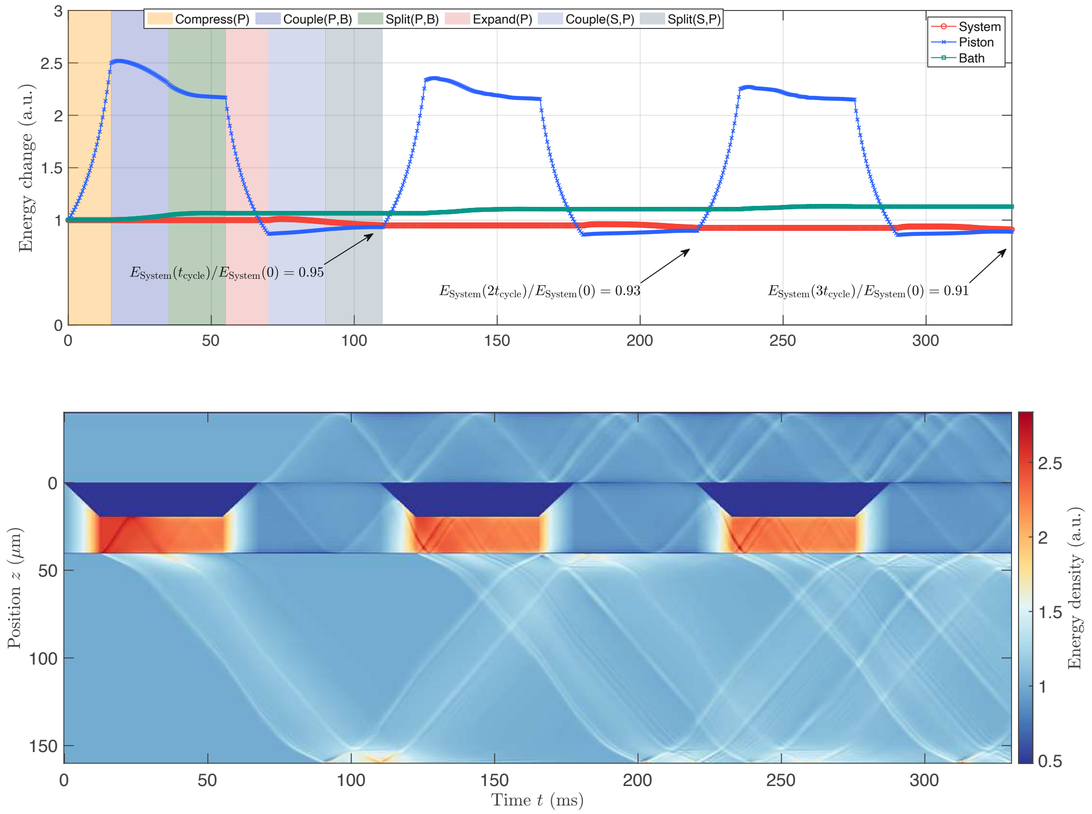

Figure 4.6: Top: Quantum field refrigerator. The QFM is initialized in thermal equilibrium and equal density, i.e., the system, piston, and bath differ only in length, which is $40, 40, 120$µm, respectively. We run the Otto cycle by compressing the piston (15 ms), depositing heat in the bath (40 ms), and then expanding the piston again (15 ms). The cooling begins at around 70 ms by coupling the initially thermal system to the cooled piston. The systems exchange energy by the physical mechanism of the valve described in Sec. 4.2.1. After the final splitting of the system and piston, we find that the system cools down, while the quantum field refrigerator extracts approximately 5% of the system's initial energy. Further cycles continue to contribute to cooling of the system, but only in very small amounts. Bottom: time-and-space-resolved energy dynamics during the operation of the QFM. From the top we show the system, piston (which changes in size) and bath. Whenever a valve QTP is operated, wave packets are injected and multiple reflections in each system can occur. The principal wave packet in the bath is timed to arrive at the interface to the piston at around 160 ms when the valve is closing, so that the piston energy is not further increased. The overall amount of energy in the bath increases, which is due to the presence of multiple wave packets.

resizing to its original length ($t_{merge} + t_{comp} = 35$ ms). Overall, at the end of the first cycle ($t_{cycle} = 110$ ms), the piston has slightly decreased in energy, while system and bath have consistently decreased and increased their energy, respectively. By performing three Otto cycles, we obtained cooling of about 10%.

4.3 Experimental implementation - a piston

This section provides a detailed explanation for how the compression and expansion operations are implemented in the experiment. The very first step is the optimization of a box potential as described in section 3.4.2. Once the optimization of a box potential is finished, implementing compression or expansion, consists in changing the size of the optimized box by turning on or off, respectively, columns of light in the DMD. The protocol for compression is thus a sequence of DMD patterns in time, where the following pattern has walls closer to each other than the previous one. To implement the inverse process, i.e. expansion, the same patterns are used but the sequence is reversed.

Experimentally, two parameters can be controlled when performing this QTP. We can choose how much the the atom cloud is to be compressed or expanded and we can control how fast we do it. Each of these parameters will have different effects on the system. Faster length changes will induce more energy and excitations into the gas, while slow processes (slower than the speed of sound) will have smaller effects. The amount of change in the length also has an effect on the temperature of the gas. The more the condensate is compressed (expanded) the more it is expected to heat up (cool down). In the following sections we quantify the effects of these processes and demonstrate the implementation of a piston stroke, reproducing the experimental implementation of the operation discussed in section 4.2.2.

4.3.1 Compression and expansion

Figure 4.7 shows the density profiles of an atom cloud being compressed. Turning on more and more columns of light closer to the center of the trap, decreases the length of the box-like potential. Since the interactions between the atoms and the dipole trap light is repulsive, more and more atoms will move closer to the center of the box. The length is changed linearly, similarly to what was done in the numerical simulations. Since the number of atoms is conserved, the density increases and becomes narrower. The inverse happens if the gas is expanded.

The compression shown in figure 4.7 was executed moving each wall $1\mu\text{m}\,\text{ms}^{-1}$, a speed smaller than the speed of sound in the gas (typically $c \simeq 1.8 - 2\mu\text{m/ms}$). It is evident that, although the compression speed is slow compared to the time scales of the system, this process still introduces perturbation on the order of 20% of the mean density. These perturbations show that the system goes out of thermal equilibrium during the process and it also becomes evident that its energy increased.

Quantifying how the system's energy changes after this QTP can be achieved through thermometry measurements. To do so, the atoms are cooled down in a box-like potential with length L_0. Starting from this point, the atom cloud is then compressed or expanded such that, at the end of the operation, the box length is L. The temperature of the system is measured

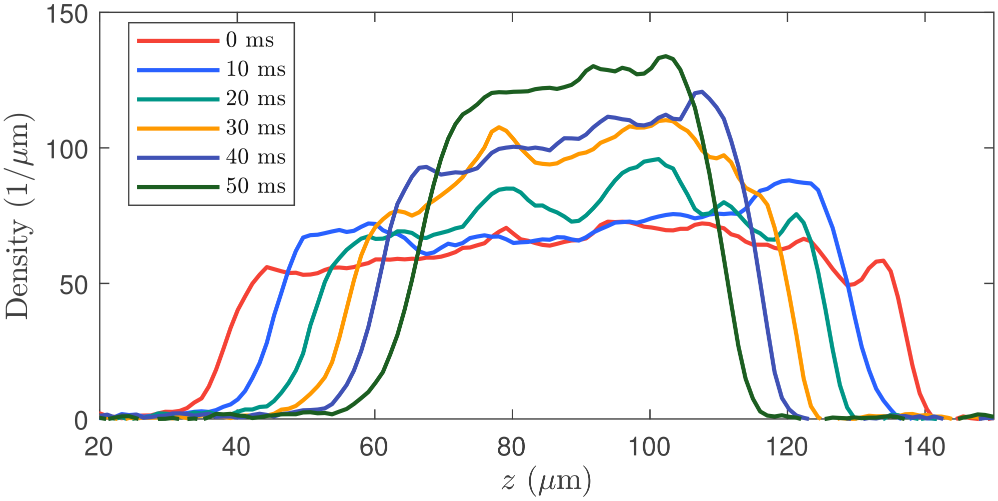

Figure 4.7: **Compressing a 1D-BEC:** Immediately before the compression ($t = 0$ms) the atom cloud is 100µm long. As the condensate is compressed, the linear density increases and the length of the atom cloud decreases. After 50 ms, the compression ends and the cloud has half of its size. The compression rate is 1µm/ms which is approximately half the speed of sound.

before and after each compression/expansion. For all the different compressions/expansions the speed of the moving walls is kept constant to investigate how the energy change depends on the initial and final lengths L_i and L_f, respectively.

It has to be taken into account that immediately after a compression or expansion the system might not have reached equilibrium. For that reason, the atom cloud evolves in the trap for 100 ms after the QTP is finished. Only then the thermometry measurement takes place. This way, the excitations induced by the length rescaling will decay and the system is homogeneous and in thermal equilibrium at the time of measurement.

It is possible to predict the final temperature after an adiabatic compression/expansion. If the process falls within the regime of adiabaticity, then the mode occupation $n(\epsilon_k)$ remains constant. The phononic energy depends on the length of the box as follows (section 2.1.2)

$$\epsilon_k = \hbar c k = \hbar c \frac{\pi}{L} n, \tag{4.9}$$

with c the speed of sound. If the length of the box changes adiabatically from L_i to L_f, then the energy ϵ_k of mode k becomes ϵ'_k. According to the theory in adiabaticity, we have

$$n(\epsilon_k) = n(\epsilon'_k) \implies \frac{\epsilon_k}{k_B T_\mathrm{i}} = \frac{\epsilon'_k}{k_B T_\mathrm{f}}, \tag{4.10}$$

where $\mathrm{n}(\epsilon_\mathrm{k})$ follows the Bose-Einstein distribution and $T_\mathrm{i,f}$ are the temperatures of the atom cloud before and after the length change, respectively.

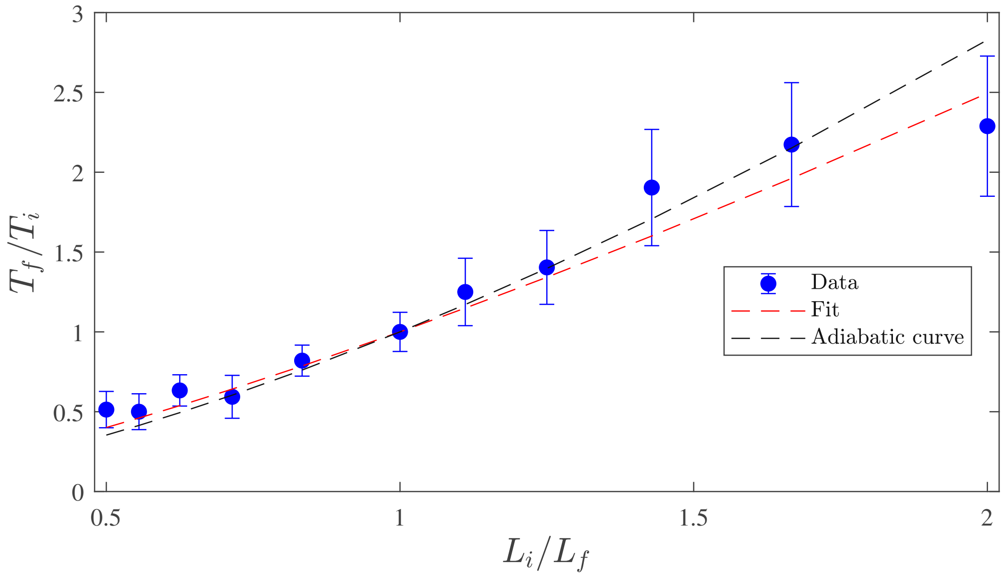

Figure 4.8: **Temperature change after a compression/expression:** The box starts with lenght $L_i = 100\,\mu m$. The length is changed linearly, by moving the walls symetrically at the constant speed of $1 \mu m\, ms^{-1}$ until the final length L_f is reached. The blue points indicate the ratio between final and initial temperatures as a function of the ratio L_f/Li. As expected, the temperature increases when the length is decreased and vice versa. The black-dashed curve shows the adiabatic prediction, while the red-dashed curve shows the fitting result of the exponent in equation (4.11), yielding a value of 1.32 ± 0.15.

Sticking to the low-energy approximation, we can use equations 4.9 and the speed of sound to derive the relation between the ratios of initial and final temperatures and box lengths.

$$\frac{T_\mathrm{f}}{T_\mathrm{i}} = \left(\frac{L_\mathrm{i}}{L_\mathrm{f}}\right)^{\frac{3}{2}} . \tag{4.11}$$

The red dotted curve in figure 4.8 shows the resulting curve when the exponent of the length ratio is extracted through fitting. A value of 1.32 ± 0.15 was computed when the wall speed is $1\,\mu m\, ms^{-1}$. The fitted curve shows that a compressing/expanding speed at half the speed of sound is close to the adiabatic scenario, probably achievable in the experiment if a slower compressing/expanding speed is used. However, from the point of view of the practical implementation of the QFM, an adiabatic process is not desired, since that would increase significantly the operating time of the machine. On the other hand, the 15 ms used for the simulations (see section 4.2.2) don't fall within the adiabatic scenario and make the implementation of the piston irreversible, as it will be shown in the following section.

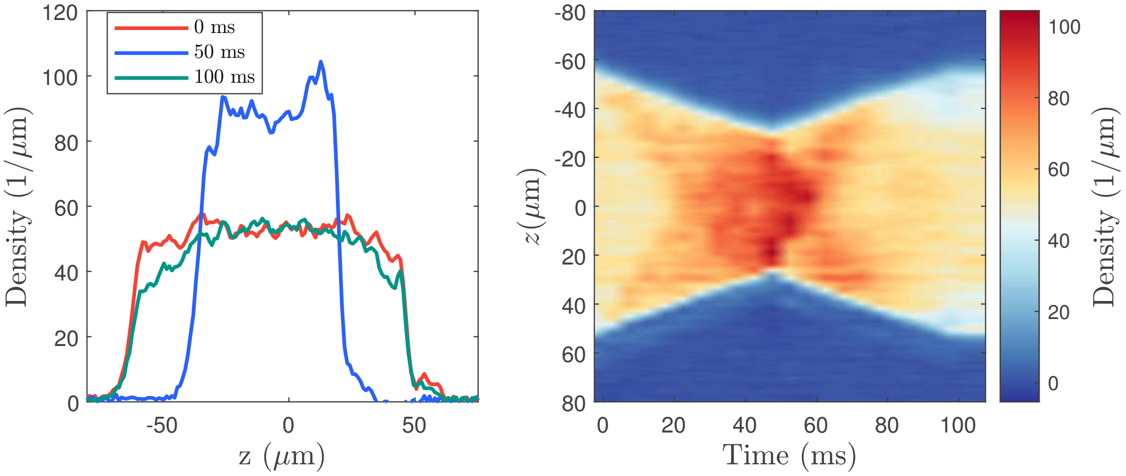

Figure 4.9: **Implementing a piston by sequentially compressing and expanding a BEC**. Both compression and expansion last 50 ms. The quasi-condensate's length is compressed to half and then restored to its original size.

4.3.2 Implementing the piston

Having demonstrated the ability to implement this QTP, it is interesting to implement the full piston stroke. This way it is possible to experimentally test the prediction from section (4.2.2), claiming the piston state should be the same after sequentially compressing and expanding the gas. In figure 4.9, we show the density profile of the cloud across time as a consequence of these processes. The condensate is compressed 50µm at a rate of 1 $\mu m\,ms^{-1}$. The expansion restores the original length of the system in the same amount of time. As expected, the density doubles when the compression finishes and goes back to its initial value when expanded again. However, it is clear that the density profile is not similar to the initial one, especially close to the walls, where the deviations from the mean initial density reach $20-30\%$. However, the profile becomes the same as the initial one after 15ms of evolution, approximately.

To study how the speed of compression/expansion affects the the piston, we repeat the protocol similar to the one described above. The piston stroke is implemented with different speeds, which is the same to say that the speed of the moving walls will be different for each case. The temperature of the piston is measured before and after the stroke procedure. In order to make sure the gas is in equilibrium, it evolves 50ms before the temperature measurement takes place. Table 4.1 presents the thermometry results before and after the piston stroke. It is evident that the faster the stroke is executed, the higher will be the temperature. Notice that the model used to fit the data assumes a system that is thermal. The bigger χ^2 values found for faster processes hints that the atom cloud had not reached equilibrium at the time of measurement. The same does not happen when the piston stroke takes 80ms to be executed. This demonstrates that only for very long times would it be

Table 4.1: **Consequences of a piston stroke.** Measured temperatures before and after sequentially applying a compression and an expansion procedure. The compressions and expansions are implemented with different durations. Slower compressing/expanding times yield more reliable results. The temperatures were computed considering a heating rate of $0.1\,\mathrm{nK\,ms^{-1}}$ in the trap.

Duration ms	T(nK)	λ_T(µK)	χ^2
Before stroke	53 ± 4	14 ± 1	2.1
40	184 ± 7	5 ± 0.1	9.6
60	184 ± 8	5 ± 0.1	3.5
80	120 ± 18	7 ± 0.5	1.6
100	116 ± 15	7 ± 0.6	0.9

possible to perform this QTP close to adiabaticity.

These observations demonstrate that a piston stroke is not a reversible operation when executed in finite time, even for time scales considerably larger than the systems time scales. Besides the energy increase after the process, it is clear that changing the length of the system in a way that preserves density homogeneity can only be done at very slow speeds (smaller than $c/2$), which makes the implementation of the QFM cycle infeasible. Note, however, that the implementation presented in this section relies only on linear operations. In other words, the changes to the box-like potential were done through simple linear interpolations between the initial and final potentials. The use of Optimal Control Theory (OCT) to implement such processes [75] is expected to minimize the perturbations introduced in the system.

4.4 Controlling longitudinal coupling

In section 4.2.1 we discussed the merging operations of two TLLs using a linear interpolation between two Hamiltonians with different interaction terms. Although this simple approach was enough to investigate some of the dynamics resulting from this process, it offers no insight to how the quasi-condensate behaves under the influence of an interface that locally changes the coupling in the longitudinal direction.

The experimental implementation of this QTP demands a closer look at how the presence of a barrier influences the degrees of freedom of the quasi-BECs. Specifically, in section 4.4.1 we will look at how the presence of a local barrier affects the phase correlation function and how that can be used to quantify the strength of the barrier. Section 4.4.2 demonstrates how local coupling is implemented experimentally.

4.4.1 Modelling a finite barrier barrier

To investigate the implications of a local potential barrier in the condensate, we follow reference [95] as a basis to the following calculations [3]. We will also use the notion of correlation functions used in section 2.2.2.

---

[3] Thanks to Igor Mazets for the enlightening discussions and help with the calculations.

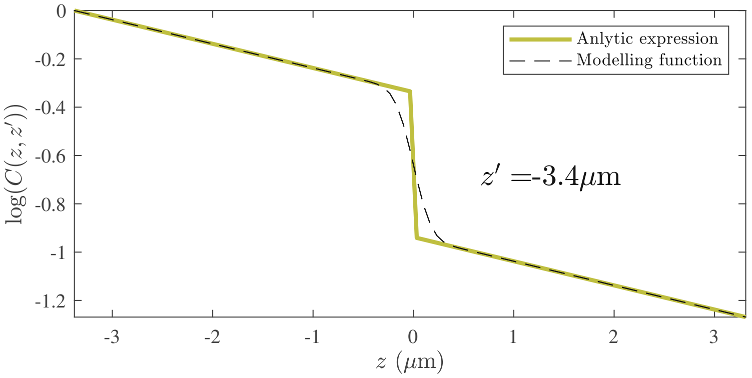

Figure 4.10: Analytic expression for the decay of correlations over a thin barrier (solid yellow line), versus the modelling function to fit the effective phase decay (dashed black line).

In the following, we will assume that we have an elongated condensate of length $L \gg \xi_h$ (with ξ_h the healing length) and a barrier at $z = 0$, the center of the condensate. In the spirit of reference [95], we will consider a perturbation of wavenumber k propagating from left to right and will assume that this perturbation is not affected by the barrier if the distance between them is greater than an amount Δz_B. If that's the case, then we can describe the perturbation with the wavefunction $\eta_k(z)$

$$\eta_k(z) \propto \begin{cases} e^{ikz} + \tilde{r}_k e^{-ikz}, z < -\Delta z_B \\ \tilde{t}_k e^{ikz}, \qquad\qquad z > \Delta z_B, \end{cases} \tag{4.12}$$

where $\tilde{t}_k$ and $\tilde{r}_k$ are the transmission and reflection coefficients, respectively. Their properties are described in reference [95]. For now, it suffices to say that the they are orthogonal, i.e., $|\tilde{t}_k \pm \tilde{r}_k| = 1$ and that they obey the condition $|\tilde{t}_k|^2 + |\tilde{r}_k|^2 = 1$ (see more details in appendix B).

If we consider the regime where the barrier is strong, we fulfill the condition $|\tilde{t}_k| \ll 1$ and thus $|\tilde{r}_k| \sim 1$.

With this new way of expressing ϕ_k, we can write the new eigenfunctions

$$\eta_{ck}(z) = \cos(kz + \text{sign}(z) \cdot \chi_{ck}) \tag{4.13}$$
$$\eta_{sk}(z) = \cos(kz + \text{sign}(z) \cdot \chi_{sk}), \tag{4.14}$$

where $\chi_{ck} = \frac{1}{2}\arg\left(\bar{t}_k + \bar{r}_k\right)$ and $\chi_{sk} = \frac{1}{2}\arg\left(\bar{t}_k - \bar{r}_k\right)$. Here sign$(z)$ is the sign function defined as

$$\text{sign}(z) = \begin{cases} -1, & \text{if } z < 0 \\ 0, & \text{if } z = 0 \\ 1, & \text{if } z > 0 \end{cases} \tag{4.15}$$

The arguments $\chi_{c,sk}$ can only be computed numerically. Instead of doing that, we make a few assumptions to simplify our analysis.

If we consider only the lowest Bogoliubov modes, we can assume $|\bar{t}_k| \sim 1$ and a linear dependence with the wavenumber $\bar{t}_k \sim 2\alpha k$ [95] , where α is a real constant. In this case, we have $\chi_{ck} \sim \chi_{sk}$. Additionally, we assume that we have $k \lesssim \lambda_T^{-1}$ (low temperatures). Using the new basis functions (B.3) and performing the integration yields,

$$\langle e^{i\phi(z)-i\phi(z')}\rangle = \exp\left(-\frac{2}{\lambda_T}(|z-z'| + |\text{sign}(z) - \text{sign}(z')|\alpha)\right). \tag{4.16}$$

If we take α to be positive, this is equivalent to introducing a Wigner delay in the phase shift [101]. The phase correlation has a drop after the barrier, proportional to the magnitude of this parameter.

In reality the barrier will have a width Δz_B. Instead of the discontinuity at the barrier position, the phase decays smoothly over the region where the influence of the barrier is present. To account for the decay of correlations under the barrier, we use an error function to model the logarithm of the PCF by summing a linear curve with an error function. To each PCF profile we fit a function (see figure 4.10)

$$f(z) = \frac{a}{2}\,\text{erf}\left(\frac{z-b}{c}\right) + dx + e \tag{4.17}$$

where the parameter a plays the role of α introduced in equation (B.6) and the parameters b and c depend on the position and width of the barrier, respectively. The slope d depends on the temperature of the gas and the parameter e is an offset which ensures that the curve starts at 0, where $\log(\mathrm{C}(\mathrm{z}_0,\, \mathrm{z}_0) = 1)$ is maximum.

SGPE simulations of a static box-potential with different barriers at its center helps illustrating the predictions made above. In figure 4.11 we can see the effects of barriers with different strength on the correlation function. Away from the barrier, the correlations decay exponentially, as expected. How fast they decay, depends only on the temperature [4] of the system. Notice that the decay rate of the correlations is the same for points outside of barrier's region of influence, defined by Δz_B. However, for points in the vicinity of the barrier, the phase correlation function decay accelerates, decreasing faster for stronger barriers. When comparing the correlations from cases with different barrier strengths, we find that, far from the barrier, the slope of the curves is the same, the correlations are identical up to an offset.

This makes it clear that a sharp change in the potential leads to loss of correlations over space, which can be used to control the coupling between to quasi-condensates in a head-to-tail configuration. A barrier bigger than the chemical potential is enough to uncorrelate the regions of space that it separates. By controlling the strength of the barrier in time, we can implement a valve that allows or prohibits the transfer of energy and matter between two distinct parts of a system.

Although the effect of the barrier on the phase correlations seems to be clear, it is so only for low enough temperatures. Indeed, the effects just described are more easily observed if there is no competition between the decay induced by the potential landscape and the one

---

[4] It also depends on the density ρ_0 and the scattering length a_s, however, in this discussion we are assuming these to be constant.

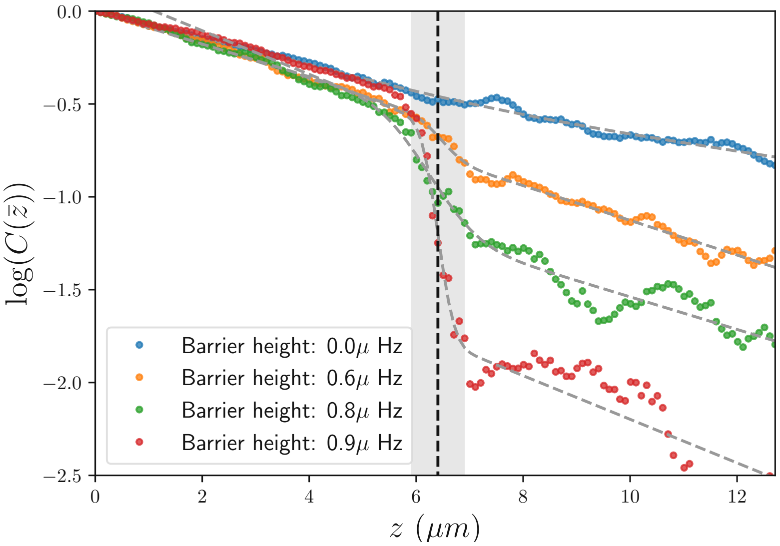

Figure 4.11: **Correlation decay over barriers of different strength:** simulation performed with the SGPE method for a quasi-condensate with a temperature of 30 nK. In the absence of a barrier (blue dots) the correlations decay exponencially (notice the log scale). When a barrier is present, the correlations decay faster under its influence. The decay rate is the same in regions where the influence of the barrier is negligible. The dashed gray lines are the curves from fitting each set of points with equation 4.10.

due to temperature. Figure 4.12 shows the evolution of the phase correlations over space at different temperatures when the same barrier is present. For systems at higher temperature, the correlations vanish after the barrier, or approach zero very quickly. Note that the effect of the barrier is not stronger due to the higher temperature [5], it merely becomes harder to quantify the strength of the barrier when the correlations after it are practically zero. For this reason, the modelling expression (4.17) might not be applicable if the temperatures are not low enough.

4.4.2 Experimental implementation of the valve QTP

Experimentally, the coupling between two different parts of a condensate can be controlled using the dipole light in a specific point in space. The presence of the blue detuned light reduces the density locally, which alters the the amount of quasi-particles that travel through that region of space. The repulsive potential created by the light is proportional to its intensity. Thus, it is expected that different amounts of light can be used to control the amount of coupling between the atoms on each side of the barrier.

The barrier is implemented by turning DMD pixels on. More precisely, the pixels giving shape to a rectangle of dimensions $H_B \times W_B$ are turned on, where H_B specifies the height of the barrier (number of vertical pixels) and W_B specifies the width of the barrier (number

---

[5] Counter-intuitively, the gap in the correlation function due to the barrier is actually smaller for higher temperatures (see appendix B).

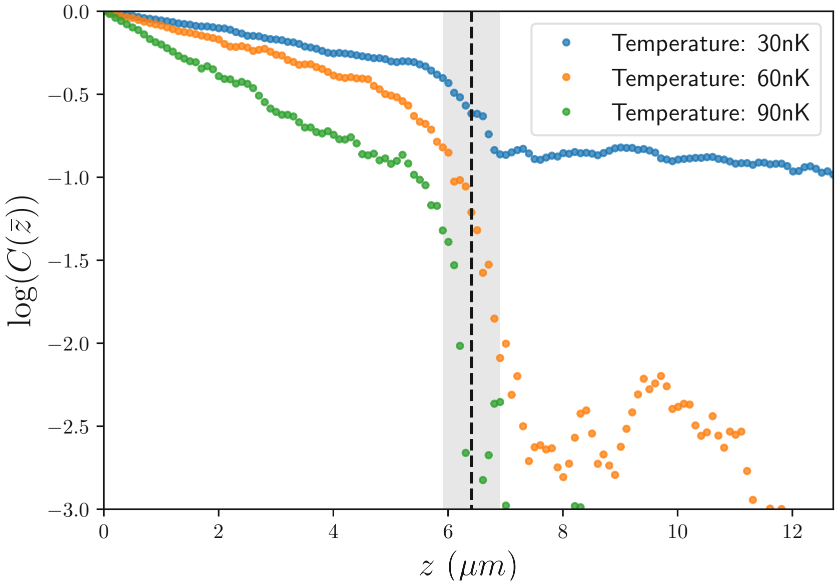

Figure 4.12: **Phase correlations in the presence of the barrier for quasi-condensates at different temperatures.** The presence of the barrier becomes harder to detect, due to the faster decay of the phase correlation function. For higher temperatures, the value of $C(\bar{z})$ is lower, making its value closer to zero after the barrier and thus harder or impossible to detect.

of horizontal pixels). The higher the values of H_B and W_B, the stronger the barrier is. Our main purpose here is to demonstrate that by creating different barriers with the DMD, we are able to achieve different coupling levels between two different parts of the atom cloud.

The measurement preparation consists in cooling down the atoms in a 100µm box potential divided by a barrier with dimensions $H_B \times W_B$. For each value of W_B, we prepare 10 different values of H_B to scan the barrier size in both dimensions. For the first of these preparations, no barrier is loaded ($H_B = 0$) so that we have a reference for comparison.

To ascertain the effects of the barrier precisely, we measure the relative phase of the longitudinal clouds and compute their phase correlation functions. The correlation function $C(z, z')$ introduced in section 2.2.2 is plotted for barriers of different strengths in figure **??**. Reading the figure from top to bottom (increasing barrier height), we see that for $H_B = 0$ we observe the typical PCF pattern for a square homogeneous box. As the value of H_B increases, it is clear that the barrier starts decreasing the correlations between the left side of the box ($z < 0$) and the right side of the box (z>0). For the figures with higher H_B values, we observe again the PCF of a single homogeneous box repeated twice. This is evidence that the two halves of the system are less and less correlated as the potential barrier becomes more relevant. Note that the effect of the barrier becomes more relevant for lower values of H_B when higher values of W_B are used, since the strength of the barrier is proportional to its volume, which is proportional to the number of pixels turned on in the DMD.

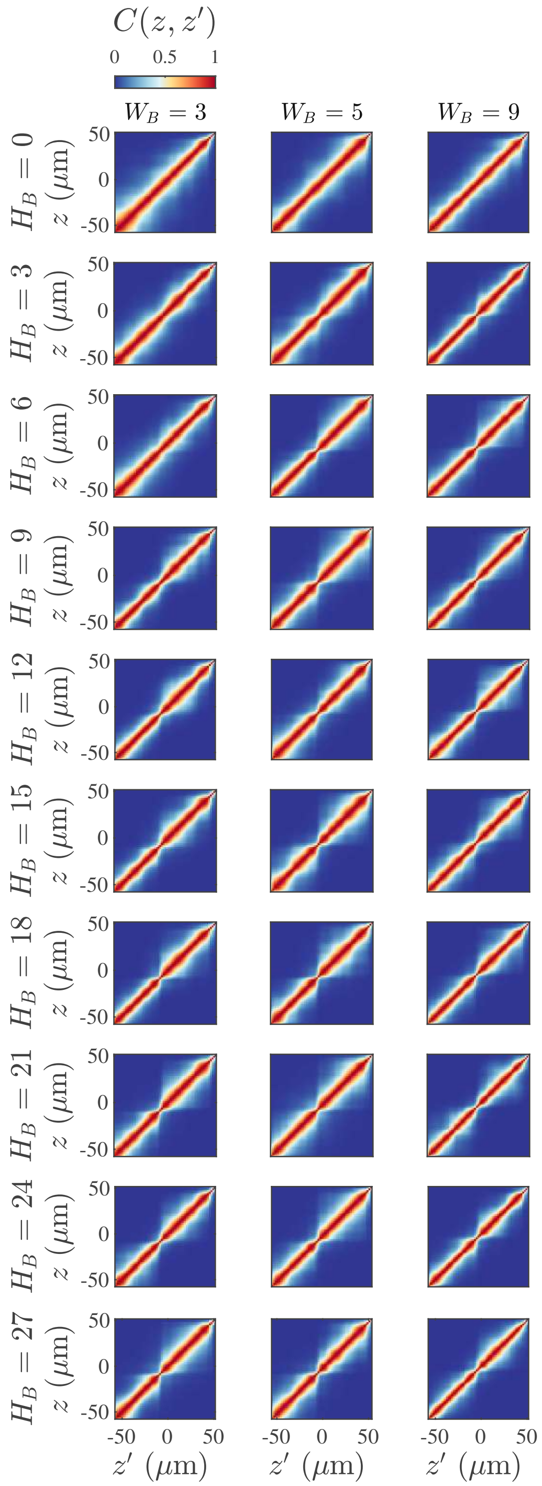

Figure 4.13: Phase correlation function $C(z, z')$ for different barrier strengths. The correlations between the left part of the quasi-condensate (lower left quadrant) and the right part of the quasi-condensate (upper right quadrant) are less correlated for bigger values of H_B and W_B.

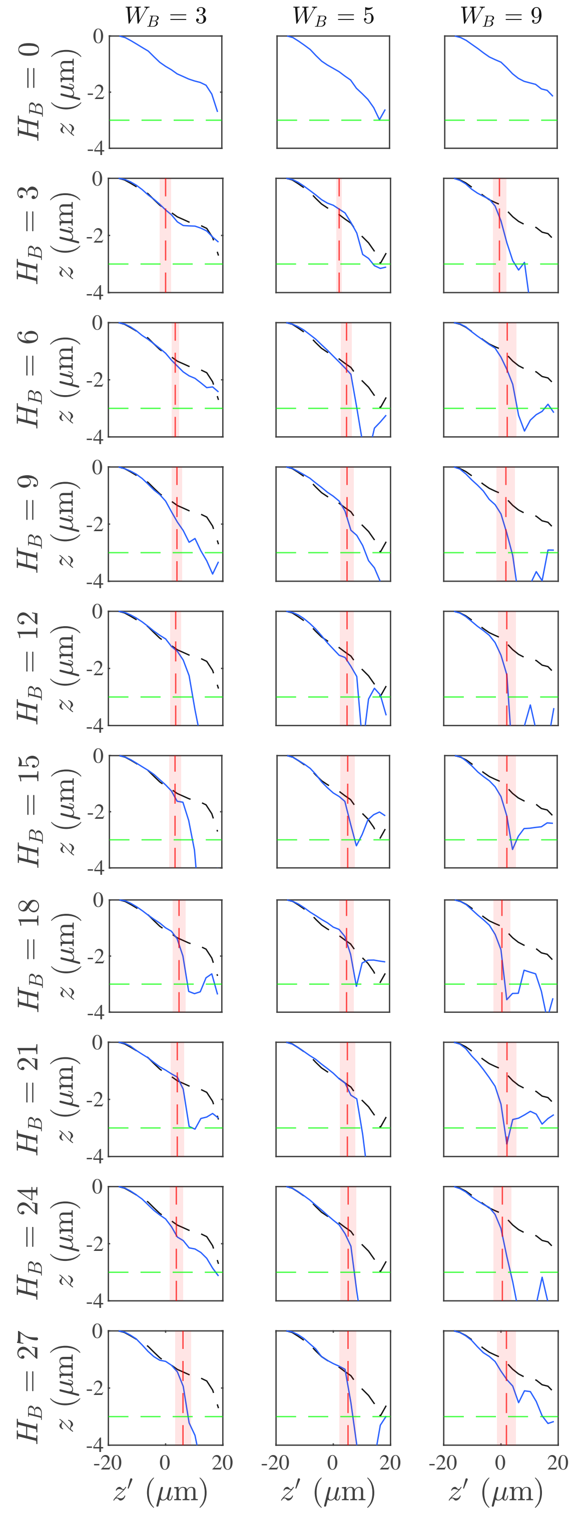

Figure 4.14: Plot cuts of the phase correlation function $C(z, z\prime)$. The plots shown here correspond to a horizontal cut in the 2D plots of figure **??** for the reference point $z_0 = -20$µm. The red dashed line indicates the barrier position and its uncertainty is given by the red shade. The green dashed line indicates the noise treshold. For $H_B > 0$ the black dashed line show the correlations found when no barrier is present.

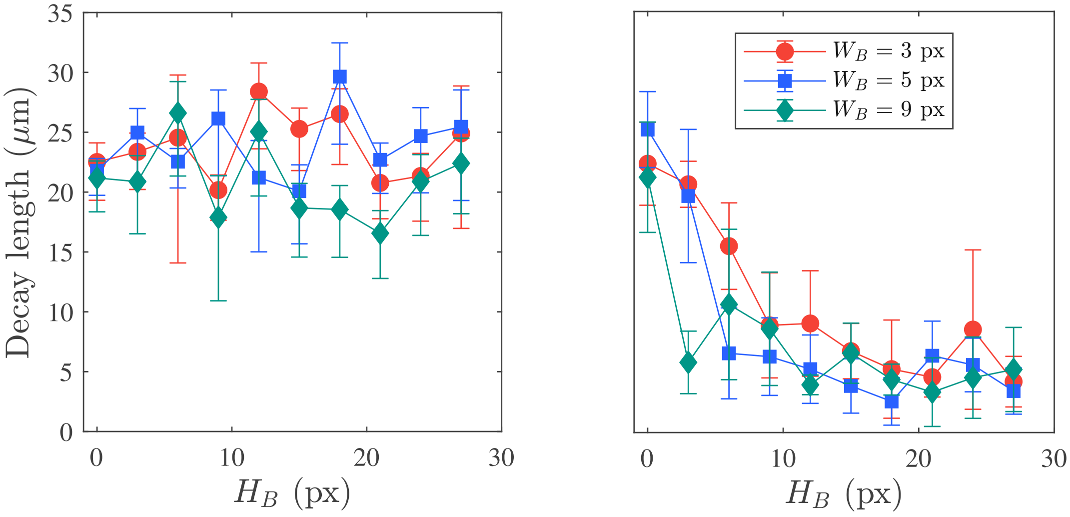

Figure 4.15: **Phase decay lengths under and far away from the barrier**. On the left, the decay lengths fitted for a reference point fixed at $z_0 = 25\,\mu m$ are shown for different values of H_B and W_B. All the fitted values at this reference point lie in between $20\,\mu m$ and $30\,\mu m$. On the right the decay length under the barrier can be found. As expected, the decay becomes smaller for larger barriers. Note that the decay lengths converge to the same value of $\sim 5\,\mu m$, hinting that a stronger barrier does not achieve lower correlations. The lines are a guide to the eye.

As discussed before, lower temperatures make the effects of the barrier more evident, whereas higher temperatures make the influence of the barrier harder to observe. This becomes clear by having a closer look at the PCF. Figure 4.14 shows how the PCF changes in space for a reference point $z_0 = -20\mu m$ for the same measurements showed in figure **??**. The red vertical bar marks the position of the barrier, while the green horizontal one signals the noise level at 3 dB. The noise level was chosen by measuring the PCF in regions where correlations are known to be practically zero. This region corresponds to distances $\bar{z} \sim 3\lambda_T^B$, where $C(\bar{z}) \sim 0.01$ is negligible. It is clear that the correlations are affected by the barrier, however, the behaviour discussed in section 4.4.1 does not seem to be present systematically. The explanation relies on the fact that the temperatures of the atom clouds, varying from $50 - 60\,$nK, are too high for that analysis to be applicable.

Nonetheless, it is still possible to analyze the barrier strength quantitatively. With that purpose in mind, we chose a reference point z_0 and compute the decay of the phase correlations around that point for the different barriers. Additionally, we evaluate how rapidly the phase correlations decay under the influence of the barrier, by using the same fitting procedure, using the center of the barrier as the reference point. Note that the decay of the phase correlation function under the barrier depends on the strength of the barrier (see figure 4.11).

Figure 4.15 shows the decay lengths found in the two different situations. As expected, the correlations are approximately constant when the reference point is far from the barrier, while under the barrier the correlations decay faster when its strength is bigger. It is also possible to observe that this decay is more pronounced for the barrier with $W_B = 9$, since the volume of the barrier increases faster with height for larger widths. Furthermore, note that the decay rate reaches a plateu for the different barrier strengths, meaning that the further increase in strength will not have any effect on the correlation function. This is evidence that the two halves of the condensate are completely separate.

Figure 4.15 shows the decay lengths found in the two different situations. As expected, the correlations are approximately constant when the reference point is far from the barrier. Under the barrier, the phase correlations decay faster for higher values of H_B, confirming the previous observations. It is interesting to note that although a faster decay is clearly observed for the thickest barrier, the values of the decay rates converge to a plateu around 5 µm, indicating that a stronger barrier will not decrease the decay rate of the phase correlations further. This is evidence that controlling the amount of light used to generate the barrier can be used to locally tune the coupling between two different parts of the atom cloud.

4.5 Summary and discussion

This chapter introduced the concept of a quantum field machine. The operation of this machine can in general be decomposed in two basic primitives: length scaling of a subsystem and coupling control between two subsystems of such a machine. In the context of this work, the QFM was conceived with the goal of being experimentally implemented with one-dimensional BECs using the atomchip platform. Therefore, the Tomonaga-Lutinger liquid model was chosen, for it is the standard model to describe such systems. Each primitive operation was implemented numerically showing the consequences of each procedure. Theoretically speaking, changing the length of one of the machine's components is a reversible task, provided that it is done slowly enough. The energy (and entropy) is increased when a cloud is compressed and the opposite happens when the cloud is expanded in the same way. Splitting and merging disturbs the system and are not reversible processes. This primitive drives the system out of equilibrium through the introduction of perturbations that propagate across the system. By stitching these operations together it was possible to build a cycle with three components, a system, a piston and a bath, and reduce the energy of the first one by 9%.

The experimental implementation of the aforementioned primitives was demonstrated. The compression and expansion of the atom clouds is achieved by linearly changing the position of the walls with the DMD. It was shown that the quasi-condensate's temperature increases when it is compressed, while the opposite behaviour is observed when the quasi-condensate is expanded, as expected. The piston stroke was also implemented. Although the density behaves as predicted, it is clear that the final state of the gas after the piston stroke is not the same even if it is executed slowly. It should however be mentioned that the implementation of this primitive relied only on linear procedures. Compression and expansion using non-linear trajectories for the walls were studied [102] and its implementation in the experiment is possible. These type of procedures use Optimal Control Theory techniques to achieve an efficient and clean change of length, using, for instance, shortcuts to adiabaticity

[74]. Due to the high computational resources required and the difficulties of matching experimental results with numerical ones, this work is still under development.

We proceeded to the demonstration of the amount of coupling that can be achieved between two different parts of the quasi-condensate. Although it was clear that it is possible to manipulate the size of the barrier to change the amount of coupling, the effects of temperature introduce a lot of noise which reduces the accuracy of the measurement.

Chapter 5

Local thermometry

In the last twenty years, the interest in the topic of the locality of temperature has risen. Driven essentially by the technological development which allows probing of micro and nanoscale dimensions, the necessity of understanding the thermal properties of small systems became unavoidable [103–105]. Also in the fields of cold atoms and atomtronics, the concept of temperature plays a central role in the description of systems in equilibrium or close to it [20]. In recent years, there has been a lot of discussion on the role of temperature in the quantum thermodynamics community, regarding its validity in the quantum realm and significance for smaller systems [106, 107].

Temperature is widely used to characterize large systems in equilibrium. The disciplines of thermodynamics and statistical mechanics use it to characterize a global state of a system, where the characterization of individual particle dynamics is unfeasible. Therein, a global temperature is assigned to the system, usually assuming the thermodynamic limit to be valid. Arguing for the existence of local temperatures is thus a subtle topic.

Although it has been demonstrated that such a concept is valid and useful [105], it is good to gve an overview why it is so. Since temperature is associated to a system in equilibrium, the concept of local temperature contradicts the global character of this quantity. For it to be valid locally, the concept of temperature has to apply to the partition of the system which is being considered. In other words, when looking at a specific sub-part of the whole system, it has to be indistinguishable from a canonical state.

If different partitions of the same system show similar temperatures, this shows that the system is globally in equilibrium. If this is not the case, then it is an indication of a global non-equilibrium state, since a redistribution of energy is likely to happen. However, such local analysis poses a problem, because the sub-systems are not isolated from each other. What are, then, the conditions under which it is valid to use temperature as a local parameter? The answer relies on the correlations existing between different sub-divisions of the system. According to [108], the temperature is intensive on a given length scale if and only if the correlations with other parts of the system in that length scale are negligible. In other words, as far as the different regions of space are uncorrelated, it is valid to consider different temperatures for each of these regions. Since we are considering independent temperatures for uncorrelated points in the same system, temperature is deemed here as a local quantity.

Given that an assessment of the temperature for different points in space is possible, this thermometry method is particularly interesting for 1D quasi-condensates. It can be used as a method to probe out-of-equilibrium states as well as a way to map (up to a certain resolution) the distribution of energy over space. This last point is utterly important for studying energy transport in phenomena such as heat flow through the quasi-condensate.

Following this line of thought, the next section discusses the concept of local temperatures applied to the 1D-condensates described throughout this thesis. We start by looking at how we can find local temperatures in these systems and what are the assumptions behind this thermometry method. Then, we show examples of the usefulness of local temperatures by looking at examples of systems in thermal equilibrium and systems where different temperatures can be found in distinct regions of space.

5.1 Local thermometry method

The relationship between the phase coherence length and the temperature of a quasi-1D BEC is the starting point for the development of local thermometry the context of the systems described in this thesis. As mentioned in section 2.2.2, the phase correlation function $C(z, z')$ of a homogeneous and thermal condensate decays exponentially in space as follows

$$C(\bar{z} = |z - z'|) = e^{-\frac{2\bar{z}}{\lambda_T}}. \tag{5.1}$$

Here, λ_T is the decay length given by

$$\lambda_T = \frac{2\hbar^2 n_{1\mathrm{d}}}{m k_B T} \tag{5.2}$$

usually known as the thermal coherence wavelength. The factor of two in the exponent accounts for the fact that we consider the double well configuration. Notice that both homogeneity and thermal equilibrium must be fullfilled for equation (5.1) to be valid.

The correlation function $C(\bar{z})$ can be measured experimentally. To obtain a temperature, a reference point z_0 is chosen and the thermal coherence wavelength λ_T can be extracted through fitting. The λ_T provides information about the temperature and is also a reference length scale which allows to ascertain which points are significantly correlated to z_0 and which ones are not. Note that to obtain λ_T, we regard the phase correlations between z_0 and all the other points. Thus, this is a parameter that characterizes the system globally (non-locally). If the system is in thermal equilibrium, we will obtain the same value for λ_T, regardless of the reference point z_0. In other words, the correlations decay with the same rate for every point in space. Otherwise, it is safe to assume that the gas is not in thermal equilibirum.

The main claim here states that a non-thermal correlation function can be interpreted as the existence of localized temperatures in uncorrelated regions of space [108]. It is only possible to do such an interpretation provided that within the considered region, the system is homogeneous and the correlations decay exponentially. These are the same conditions required for the validity of equation (5.1), applied only to the partition of the system under analysis [1].

To compare temperatures of two distinct parts of the system, the two conditions mentioned just above are not enough. In addition, it is required that these two sub-systems are

---

[1] In fact, a homogeneous density is not required to define local temperatures. However, since it simplifies the problem substantially, we shall move forward with it.

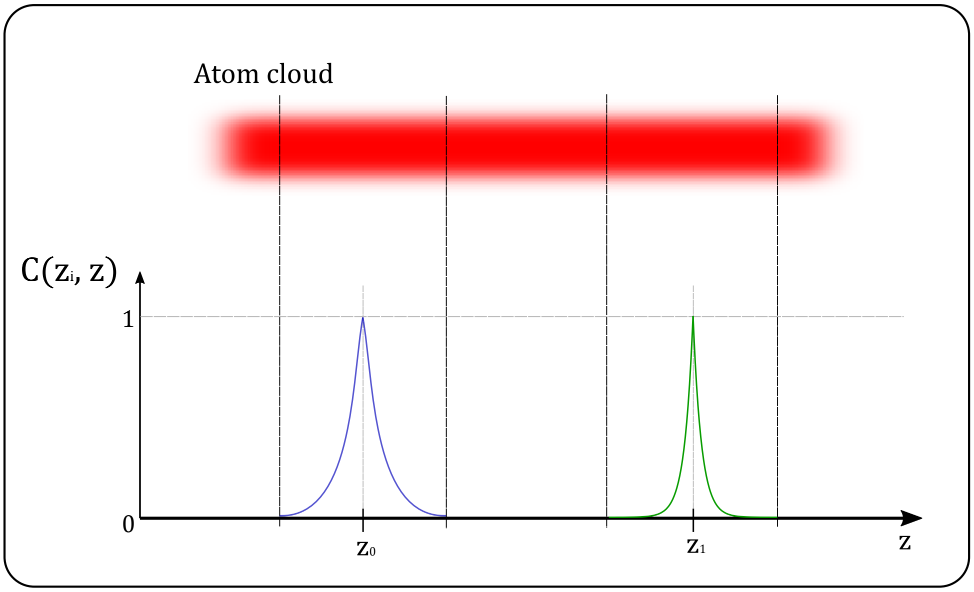

Figure 5.1: **Illustration of local temperature method:** The red shade represents the one-dimensional atom cloud in space. The phase correlations are sketched for two different reference points (blue for z_0 and green for z_1). The vertical black solid lines mark the limits of the analysis region for each of the reference points. Notice that at the boundaries of these regions the correlations are practically inexistent. The regions defined for each reference point are also distant enough such that no correlations exist between them. By extracting a decay length within each region, we can effectively compute a temperature that characterizes each of the regions, making the analysis local. Since the correlations within the region defined by z_1 decay faster, we will find a higher temperature around this point, compared to the one found for the region defined by z_0.

sufficiently far away from each other, in order to avoid correlations between them. Negligible correlations are crucial because it approximates each sub-system to the "isolated system" scenario. Although it is true that these partitions of the system are not isolated and exchange energy with the surroundings, the fact that they are uncorrelated makes them independent, allowing an unambiguous interpretation of the phenomena happening locally (see figure 5.1).

To measure the temperature at a specific region, we select the reference point z_0 at the center of that region. Fitting the correlation decay in the surroundings of z_0 allows the extraction of the decay length of the phase correlation functions λ_D on that region. The different notation for the decay length emphasizes that this parameter refers to a region of the system and not to the whole space. Knowing the value of λ_D allows the calculation of an effective temperature T_{eff}, valid only in the surroundings of z_0. Given we can perform this analysis for every point in space, we can write a local version of equation (5.2)

$$T_{\text{eff}}(z) = \frac{2\hbar^2 n_{\text{1d}}}{m k_B \lambda_D(z)} \tag{5.3}$$

Note that the value of λ_D has to be similar or smaller than the region's length, otherwise

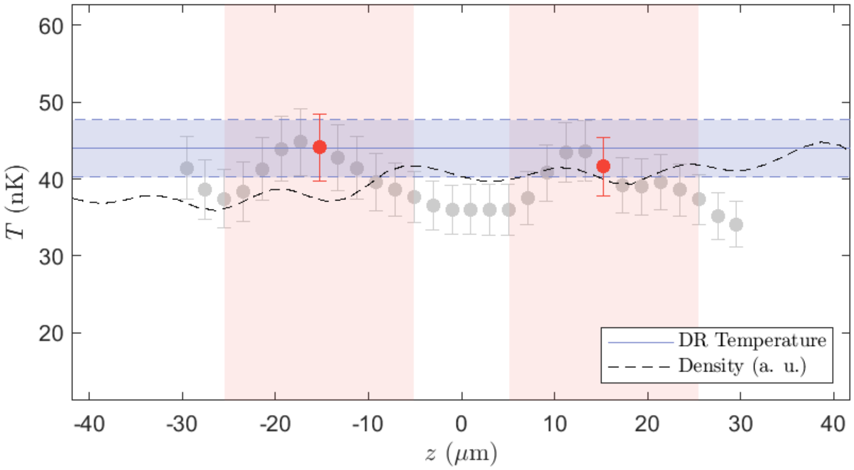

Figure 5.2: **Local thermometry method applied to a thermal state:** Comparison of the local thermometry method (red dots) with Density ripples thermometry (gray bar). The density profile (dashed black line) is shown for visual reference only. A region of 24 µm around each point was chosen to fit a decay length of the phase correlation function. The atom cloud with $\sim$ 5000 atoms was measured in a box-like potential with a length of 100 µm. All the error bars were computed using a confidence level of 68%.

important correlations are being thrown away. Regions on the order of the decay length of the correlations ensure that the intensive property of the effective temperature is respected (see figure 5.3). Since we are working under the local density approximation, $n_{1\mathrm{D}}$ in (5.3) is the mean value of the density within the region of analysis.

Besides the requirements above, we need to take into account other technical details when applying this method. Therefore, there are specific criteria to evaluate the validity of this method. A thorough discussion of such criteria is provided in section 5.4.

5.2 Example: homogeneous thermal cloud

As a first example, we apply the local thermometry method to a thermal cloud in a 100 µm long box potential. This scenario provides a system under well known conditions and allows the comparison with the standard Density Ripples (DR) thermometry method. Figure 5.2 shows the comparison between these two methods. The blue line indicates the temperature found with DR and the shaded area indicates the error computed with a confidence level of 68%. The red dots show the temperatures found with the local thermometry method for the corresponding red shaded regions (each one 20 µm long).

Each of the remaining gray points, indicate the temperatures that were extracted if they had been chosen as the reference point for a region centered around it. For all of them we find similar temperatures, as expected, since the system is thermal and homogeneous. It is also interesting to observe that the temperatures from both methods are similar, confirming the reliability of the local thermometry method described before. Notice that the selected regions are far enough apart such that they are effectively uncorrelated. The distance between them

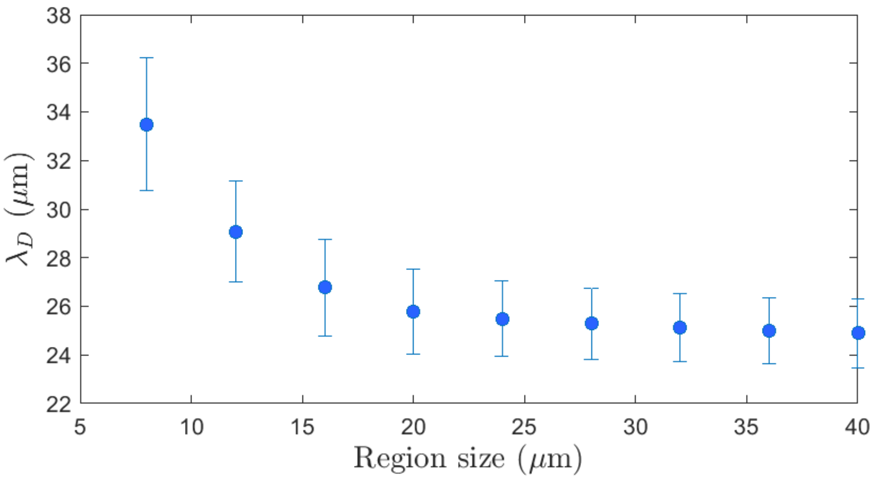

Figure 5.3: **Finding the smallest region for local thermometry:** The center of the box was used as reference. We find that the coherence wavelength converges for regions which are of the same scale as this parameter. Too short regions neglect relevant correlations, making such regions not suitable for local thermometry. This shows how to find a lower limit for the size of region of interest for such a method.

exceeds the value of λ_D, which indicates that the mutual information shared between both is inexistent [109]. The selected points are at least 20 µm from the box edges, to make sure that the influence of the vanishing density near the boundaries is negligible.

Choosing how big a region of analysis should be, is crucial to obtain reliable results for the temperature. By truncating the region where $C(z, z')$ is being fitted, it is necessary to make sure that important correlations are not neglected. Figure 5.3 shows the extracted decay lengths λ_D for different region sizes. It is clear that the value of λ_D converges for regions of larger size. A value of approximately 25 µm is obtained reliably for regions of 24 µm or larger. Regions considerably smaller than 25 µm yield bigger values with larger uncertainties, revealing that important correlations were neglected. From this, we infer that a region of analysis is only valid when from the point in which increasing its size does not yield a different decay length of the phase correlation function.

5.3 Example: two different temperatures across space

We now apply the local thermometry method on a system where two distinct (and independent) atom clouds have different temperatures. The system consists in two boxes with half the size of that shown in figure 5.2. The boxes are uncorrelated, separate by a potential barrier, so that energy can not flow from one box to the other. At the end of cooling, the two halves of the system show similar temperatures. A temperature imbalance is created by shining random blue-detuned light over a period of 175 ms (for a full description of the heating procedure, see section 6.3) on the right box. After the heating procedure, the system consists of two independent atom clouds in a head-to-tail configuration, exhibiting different temperatures. The local thermometry method can be then applied to each of the smaller

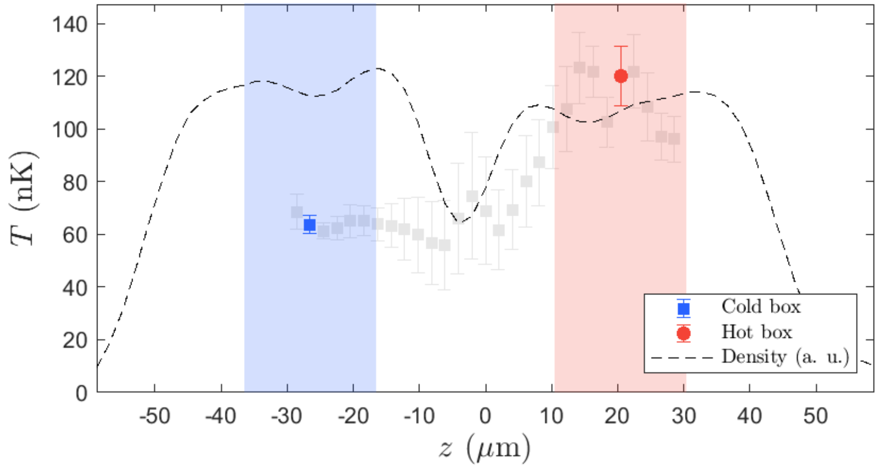

Figure 5.4: **Thermometry in different regions of space:** The blue and red data points show the measured temperature for the cold box (blue shaded region) and for the hot box (red shaded region), respectively. The coherence lenght λ_D found for the cold and hot boxes are, respectively, 19 µm and 9 µm, smaller than the 24 µm regions considered. The points were chosen to be in the middle of each box to avoid the influence of boundary conditions. The light-gray points indicate the temperatures found when each of those points is used as a reference. The bigger errorbars close to the barrier position show that the method is not reliable when the density is not homogeneous enough. The dashed black line shows the density profile shape as a guide to the eye. The density profile was measured after 15.6 ms time of flight.

thermal clouds.

The results yielded by the local thermometry are shown in figure 5.4. To compare the temperature in the different boxes, we choose the reference points to be at the center of each box. The regions around these points are chosen to be 24 µm long and are independent from each other. As expected, the heated box has a higher temperature than the box where no heating was performed.

The gray points shown in 5.4 show the temperatures that would have been obtained if the respective points were chosen as the reference. It is interesting to observe that the gray points close to the chosen references show similar temperatures, indicating that around the selected regions the temperature is constant. On the other hand, the points close to the barrier position show larger error bars, indicating less reliability. Indeed, around the barrier the density is not homogeneous, which falls out of the local density approximation assumed before.

Notice that the two small boxes are independent due to the presence of a potential barrier between them. This makes it possible to compare a point of the cold box with any of the points in its hotter counterpart and vice versa. For the specific case of the regions presented in figure 5.4, the comparison would still be valid even if a barrier was not present. This is possible due to the distance between them ($\sim$ 30 µm), which exceeds largely the coherence wavelength found within those regions (see figure 5.4 caption).

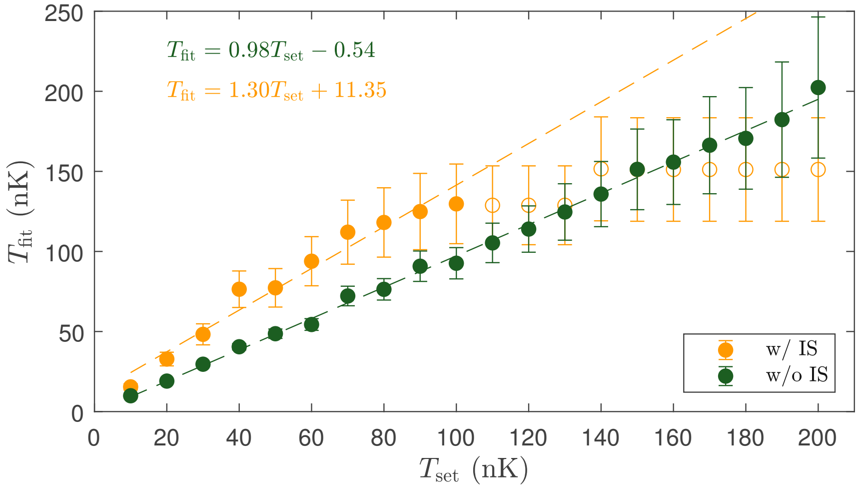

Figure 5.5: **Effects of the imaging system:** The green points show the simulations set temperatures vs the fitted temperatures extracted with the local thermometry method. The yellow points show the same but considering the effects of the imaging system. The imaging system introduces an offset temperature and the fitted temperatures grow by a factor of 1.3. Moreover, the results are not reliable anymore for higher temperatures, due to the width σ_{PSF} of the point spread function. The dashed lines (and correspnding text) show the fit curve (and fit parameters) with and without the imaging system. When the imaging system is considered, only the full points are considered for the fit.

5.4 Discussion

5.4.1 Validation criteria

The local thermometry analysis can be applied using any space point as a reference to define a region. However, as mentioned before, not every region of space yields a result which can be interpreted as a temperature. The local thermometry method requires homogeneity and thermality in the spatial region being analyzed. Since there might be dynamics in the system, the validity of analysis of a specific region can change in time. Thus, it is necessary to find adequate criteria and verify that the region around a specific reference point fulfills these conditions at different times.

To address the density's homogeneity, we calculate the averaged density variance of the initial state, known to be thermal, and use it as a reference for the future instants. Using the averaged density is crucial, for it eliminates the thermal fluctuations and accounts for all the inhomogeneities present due to the box-potential imperfections. Using the averaged density variance of the initial state as a variance, we proceed to the calculation of the same quantity at later times ($t > 0$) in the selected space regions. For such region to be considered homogeneous, its (averaged) density variance has to match that of the initial state, making sure there is resemblance between the thermal density and the one being analyzed. Otherwise, the effective temperature extracted in the selected space region is not valid, that is, this specific region of space at that instant cannot be used for local thermometry, due to the non-homogeneity of the density.

Thermality within the region of analysis can be checked by comparing the distribution of the measured phase variance with the phase variance distribution of a reference thermal state [2]. The reference thermal states are generated using the Ornstein-Uhlenbeck process to simulate thermal wavefunctions at different temperatures. We also simulate the measurement process (see section 5.4.2 for details) so that the simulated data is in the same situation as the experimental one. Then, for each temperature, we can calculate the phase variance distribution of the reference thermal states.

Having extracted the local temperature T_L^{exp} from the experimental data, we can compare the phase variance distribution within the region of analysis to that of the thermal state with the correspondent simulated temperature T_{set}. Since the phase distributions are known to be exponential (see appendix C), we consider the distribution to be the same if the same mean value is found for both.

These are the two criteria used to validate the computed effective local temperatures. Although these criteria fulfill the requirements introduced in section 5.1, there are experimental and technical limitations that introduce further restrictions for the validity of local thermometry. These are discussed in the following section.

5.4.2 Limitations

The limited resolution of the imaging system imposes restrictions on the upper limit for temperature measurement. Since temperature is computed through the fitted decay length λ_D, the smallest value for this quantity is limited by the resolution available. The point spread function of the vertical imaging system (described in 3.5.2) is modulated with a gaussian function, whith width $\sigma_{\mathrm{PSF}} = 3\,\mu\mathrm{m}$. Figure 5.5 shows how the imaging system affects the measured value of the temperature with this method. By simulating thermal states with the Ornstein-Uhlenbeck process [110], we apply the local thermometry method before and after considering the effects of the imaging system [3]. Without taking into account the imaging system, the temperatures computed from simulated wavefunctions match closely the temperatures initially set in the simulations. When the imaging system is considered, the relation between the set temperatures and the ones fitted is only linear for lower temperatures. Moreover the linear relation is not without an offset and a slope that deviates from 1 by 30%. For the densities presented in this work ($n_{1\mathrm{D}} \sim 60 - 70\,\mu\mathrm{m}^{-1}$), the linear relation stops being valid for temperatures close to $\sim 150\,\mathrm{nK}$, when the correspondent λ_T starts getting close to σ_{PSF}. For this reason, we disregard values of $\lambda_T < 5\,\mu\mathrm{m}$.

Besides the restrictions enunciated above for the application of this method, there are other limitations that have to be accounted for. The phase correlations don't decay exponentially if the reference point is close to the system boundaries (local density approximation

---

[2] Here we mean the spatial variance of the phase field. For each experimental/simulated realization, the phase variance is computed for a specific region.

[3] The effect of the imaging system can be simulated by computing the expansion of the wavefunction in time of flight and convolving the evolved wavefunction with the PSF [79]. The code was written by Thomas Schweigler and developed further by Frederik Møller.

breakdown) [111] . Thus, a local temperature can only be extracted when far its reference point is not in these conditions. In the context of this thesis, the reference points are always located at the center of a box, as in the example in figure 5.4.

Chapter 6

Heat flow

In this chapter we look at the first experimental endeavors exploring the thermodynamics of non-equilibrium 1D cold gases. We start by motivating this endeavor in section 6.1. Here it is also clarified what is meant by heat flow and how it can be measured with the available tools. The general scheme of how this topic will be studied in the experiment is described in section 6.2. The basic idea is simply merging two 1D atom clouds at different temperatures and observe the consequences for the following dynamics. To achieve this temperature imbalance for the initial state, we need to heat up one of the clouds at the final stage of evaporative cooling in the trap. This local heating procedure is described in section 6.3. After describing the experimental details that allow the investigation of heat flow in 1D systems, a theoretical description and the experimental results are presented in sections 6.4 and , respectively. We conclude by providing a summary and a discussion on the results presented throughout the chapter.

6.1 Motivation

The merging procedure studied numerically in section 4.2.1 is one of the pillars of the QFM. Implementing it experimentally is thus of paramount importance to have a completely functioning QFM, for it is through this process that energy is shuttled between different parts. On the other hand, it is also a very interesting problem solely from the thermodynamic point of view. Inducing an energy exchange through coupling in one dimension, requires evolving a non-equilibirum state, a subject of great interest in the recent years [21, 46, 112] .

To address this process experimentally, we start with a simple protocol which consists of coupling two atom clouds that are initially separated by a potential barrier sufficiently strong to uncouple them (see figure 6.1). This barrier is then lowered linearly in a finite amount of time to merge the two clouds into one. For an energy exchange to happen, we make sure that the two clouds to be merged have different temperatures. This simple setup allows the detailed study of the merging process, sparing the complications of extra procedures, as the ones shown in secion 4.2.3 .

After merging, we intuitively expect to see some redistribution of energy due to the different temperatures that the systems hold in the beginning, namely an evolution towards a global thermal state. We denominate this redistribution of energy as heat flow. To measure heat flow, we use temperature as a proxy quantity, since this is accessible from the measurable observables in the experiment (Chapter 3). Note that we are dealing with an isolated system, whose total energy can be assumed to remain constant (after the merging). Since the energy distribution is not homogeneous in space, we expect that it will change in the subsequent dynamics. Thus, the heat flow that we adress here is actually a local quantity, which varies over time. For this reason, we apply the local thermometry method, described in chapter 5.

Even though an approach to a thermal state is expected, it is known that the Poincaré theorem [113] is also valid for a system with discrete energy spectrum [21,114–116]. Therefore, it is expectable that after the merging is complete, we observe the system returning to a state close to the initial one. Thus, we expect that the heat flow takes the merged system to a state closer to thermality and that this evolution is somehow reversed, bringing the system to a state closer to a non-equilibrium one. Since this last redistribution of energy drives the system away from thermality, opposite to what is expected classically, we denominate this energy flux as anomalous heat flow. The theoretical description for this phenomena is laid down in section 6.4.

6.2 Experimental procedure

To study the merging procedure, we cool down the atoms in the double well trap by applying evaporative cooling for 400 ms. While evaporative cooling takes place, the light of the dipole trap (see section 3.4.2) is ramped up to create a potential landscape that consists of two boxes adjacent to each other, as illustrated in figure 6.1. The slow increase of the light intensity allows the atoms to adapt to the new potential while avoiding heating through scattering. The cooling procedure happens uniformly over the longitudinal direction. Since the initial state for the merging protocol requires two boxes with different temperatures, an additional local heating procedure is performed, while the atoms are being cooled down. One of the boxes is heated up for a period t_{heat}, which determines its final temperature. More details on this heating procedure are presented in section 6.3.

As soon as the preparation of the initial state finishes, the barrier that separates the two condensates starts being removed. The removal happens through a linear decrease of the barrier height that lasts 9 ms. After this, the system evolves in the full box (the two initial boxes without the barrier).The evolution after the merging is complete ranges from 100 ms to 145 ms, depending on the length of the full box (see section). After the evolution of the merged system, the traps are turned off and a measurement takes place. Since the measurement is destructive, the procedure is executed several times, tipically 300 repetitions.

This experiment is performed in the double well configuration such that an interference pattern can be measured and the relative phase field extracted from it, as described in section 3.5.4. The investigation about the system dynamics will be carried on by looking at the evolution of the phase correlation function and by applying the local thermometry method.

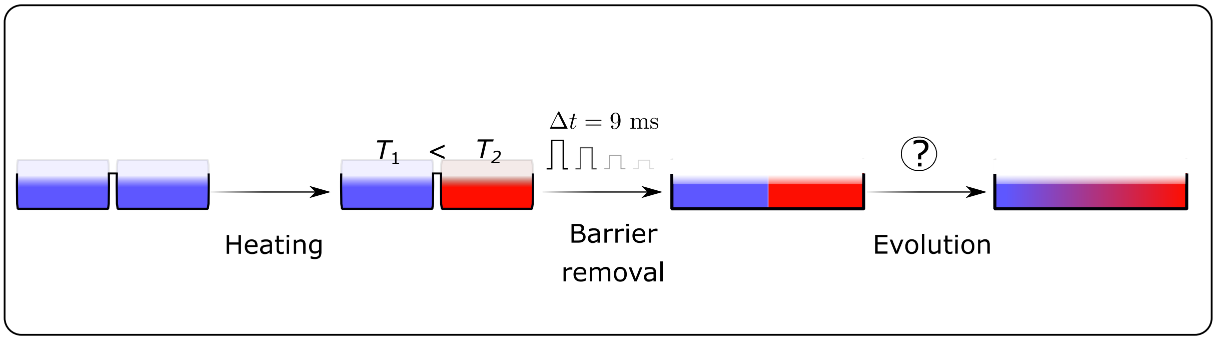

Figure 6.1: **Merging procedure scheme:** The initial state consists of two adjacent and uncorrelated gases at different temperatures. After the preparation of the initial state, the barrier between the two condensates is removed linearly in $\Delta t = 5\,\mathrm{ms}$. The system evolves in the full box for enough time to styudy the subsequent dynamics. The main goal is to observe how the redistribution of energy in the joint system will take place. The observation of a single temperature in the whole box shows that heat flow ocurred.

6.3 Local heating

This section describes how a difference in temperature between two condensates in a head-to-tail configuration is achieved. Having such a spacial-dependent temperature difference in the initial state is convenient to study the propagation of energy through the system when the two independent quasi-condensates are coupled. At the end of the cooling cycle, due to the global effect of evaporative cooling, both condensates have the same temperature. To create a temperature difference, extra procedures are necessary.

It would be possible to create such a difference in temperature through compression of one of the condensates. However, this procedure brings some technical challenges because changing the length of one condensate also changes its density. Since a zero net flow of particles between the two boxes is to be achieved, coupling two atom clouds with different densities would require the manipulation of the chemical potential of at least one of the clouds. Although this is deemed possible, it would increase substantially the complexity of implementing this protocol.

A simpler approach consists in introducing random noise in one of the condensates to increase its average energy and thus its temperature. The random noise is implemented by shining the dipole light in the region of space where the quasi-condensate to be heated is located. The dipole light, manipulated with the DMD, will dynamically change the bottom of the heating box in such a way that the atoms get moved around but the chemical potential remains unchanged. This is the mechanism through which the temperature of the atoms in one box can be achieved without any particle loss or major change in the potential. The details of the implementation of this procedure as well as its consequences are described in detail throughout the next sections.

6.3.1 Heating with white noise

The phase and density fluctuations of a quasi-condensate can be described in k-space (see section 2.1.2) through a cosine transform

$$\delta\hat{\rho}(z) = \sqrt{\frac{2}{L}}\sum_k \delta\hat{\rho}_k \cos(kz), \quad \hat{\theta}(z) = \sqrt{\frac{2}{L}}\sum_k \hat{\theta}_k \cos(kz), \tag{6.1}$$

where $\delta\hat{\rho}$ and $\hat{\theta}$ are the mode amplitudes, following bosonic commutation relations. In a thermal state, the occupations of these modes follow the Bose-Einstein (BE) distribution [48]

$$n_{\mathrm{BE}}(\epsilon_k) = \frac{1}{\exp\left(\frac{\epsilon_k}{k_B T}\right) - 1} \tag{6.2}$$

where ϵ_k is the energy of mode k. The temperature of the condensate is related to the distribution of energy over the different modes. The bigger the occupation of the modes, the higher the temperature of the condensate. It is thus clear that in order to increase the temperature of a quasi-condensate, a mechanism that increases the occupation of all the modes is needed.

Although the BE distribution is not linear, working in the regime of low energies ($\epsilon_k/k_B T \ll 1$) allows a linear approximation to be made

$$n_{\mathrm{BE}}(\epsilon_k) \simeq \frac{k_B T}{\epsilon_k}. \tag{6.3}$$

Given that this approximation is valid for the setup of this work, it becomes clear that to increase the temperature by a certain amount, it suffices to increase the energy of all the accessible modes by the same ratio. The natural choice for the energy-inducing noise used to heat up the quasi-condensate is white noise. White noise has the property of having a constant power spectral density, that is, all the frequencies have the same amplitude [117]. By changing the bottom of a box potential with white noise, it is possible to excite all the box modes equally, increasing the mode occupation in the desired fashion.

The noise is implemented by manipulating the dipole trap light with the DMD. It consists of a sequence of changing patterns displayed in the DMD over time. The different patterns in the DMD create a dynamic trap in time.

Specifically, in each DMD pattern, a random number of pixels is turned on in each column that affects the targeted quasi-condensate. In each pattern a different number of pixels is turned on in each column. The sequence of pictures in time makes the light intensity random at each point in space, creating the random changing box-bottom that will increase the energy of the atoms.

Although the number of active pixels in a column is random, an upper bound $N_{\max}$ is defined. This way, the average number of active pixels per column in a picture will be $N_{\max}/2$. The value of $N_{\max}$ is kept constant for the entire sequence of images. This allows the strength of the noise to be controlled. A higher value of $N_{\max}$ will increase the amount of average active pixels, leading to a bigger change in energy.

It is now clear that there are two parameters to control the heating process of the quasi-condensate: the noise 'amplitude', defined by $N_{\max}$ and the duration of the process.

The pixel size defines the width of columns, which sets an upper bound for the box modes that can be populated. If the columns' width is not small enough, the uniform excitations of the energy modes in equation (6.3) is not achievable. The column width in the plane of atoms is $l = 0.417\mu\text{m}$ (slightly larger than the typical healing length $\xi_h \sim 0.3\mu\text{m}$). A simple calculation with typical experimental parameters is sufficient to see that we are within the requirements to perform the desired heating procedure. The ratio between the box's length $L \simeq 50$ and the columns width quantifies how many modes can be targeted with the DMD resolution

$$\frac{L}{l} = \frac{50}{0.417} \sim 120. \tag{6.4}$$

This is well above the number of modes entailed by the low-energy approximation used in equation (6.3).

Recall that during all this process, the two longitudinal clouds are separated by a potential barrier which uncouples both clouds and thus avoids tunneling of excitations between the two. As a consequence, the energy input from the heating process is restricted in space and only one of the quasi-condensates is heated up.

6.3.2 Effects of the heating procedure

In this section we look at the consequences of executing the heating procedure. There are two parameters that can be controlled experimentally: the duration of the process and the noise strength. To demonstrate the effects of each one, we consider two adjacent boxes, separate by a barrier which completely uncouples them. The atoms are cooled down in this 'box-with-barrier' potential and thus each of the small boxes has a similar temperature. The noisy light is shined on the box on the right. After the heating process finishes, the cloud is measured. All the temperatures in this section are computed using the local thermometry method introduced in section 5.

Figure 6.2 shows the difference in temperatures between the two boxes when the heating procedure is carried on for different times. The value of N_{max} is fixed to 5 pixels. For smaller heating times, the temperatures of the two boxes remain similar, while for times longer than 300ms significant differences between the temperatures of the two boxes start to emerge, reaching differences in temperature as high as 60nK. Notice how the temperature of the unheated box remains constant for different heating times. This reveals that the two adjacent quasi-condensates are indeed independent and that this heating procedure can be targeted to one specific cloud without perturbing the other.

We now look at the consequences of using different noise amplitudes for the heating procedure. Figure 6.3 shows how the temperature of each box changes for each value of N_{max} used in the heating process. The targeted box was heated for a period of 437ms. It is clear that using a bigger value of N_{max} will decrease the coherence length of the targeted condensate (see the inset in figure 6.3). It is thus expected that the temperature exhibits the opposite behaviour. However, that is not observed. Instead, we see the temperature found for values of $N_{\text{max}} > 5$ are similar or smaller compared to the one found when $N_{\text{max}} = 5$. This happens because higher values of N_{max} don't conserve the number of particles of the targeted quasi-condensate. The amount of energy input is enough to expel a considerable

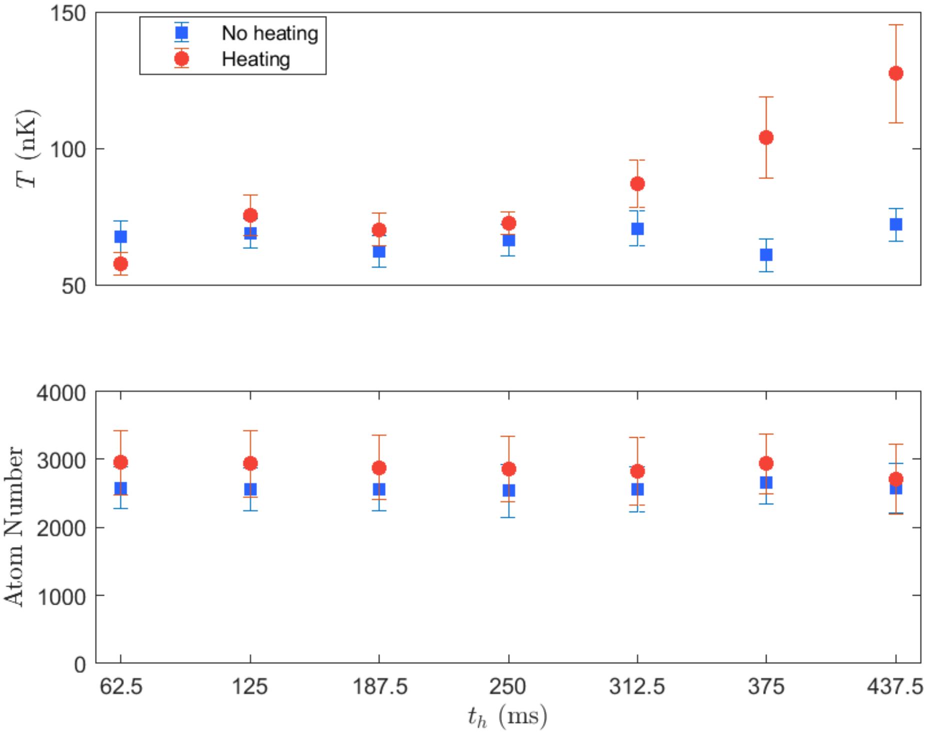

Figure 6.2: **Different heating periods.** Top: Temperature for each box after the heating procedure takes place. The temperature of the right (targeted) box increases for longer heating periods, while the left box (blue squares) remains constant, regardless of the heating time. The value of N_{max} was set to 5 DMD pixels. Bottom: Atom number in each box. Heating duration doesn't have an effect on the number of atoms in each box, a difference in temperature can be achieved while conserving the atom number in each box.

amount of atoms out of the trap (see bottom of figure 6.3). This effect is important to be accounted for, not only to know the actual meaning of temperature but also because equal densities are desired at the end of the heating procedure.

It should also be pointed out that the relation between the obtained temperature and the value of N_{max} might change whith the optimization of the specific potential being used. Since more or less light might be needed for the optimization of a potential, the amount of DMD pixels demanded to produce significant noise might change. It is highly recommendable checking these dependence before any experiments requiring temperature differences are performed.

6.3.3 Conclusions

We have seen that heating an isolated 1D atom cloud is achievable by using a random pattern of light in space and time. The spatial distribution of the light should populate the different spatial frequencies uniformly, following the statistics of White Noise. The range of frequencies spanned by the random patterns should at least cover frequencies on the order of $1/\xi_h$ to

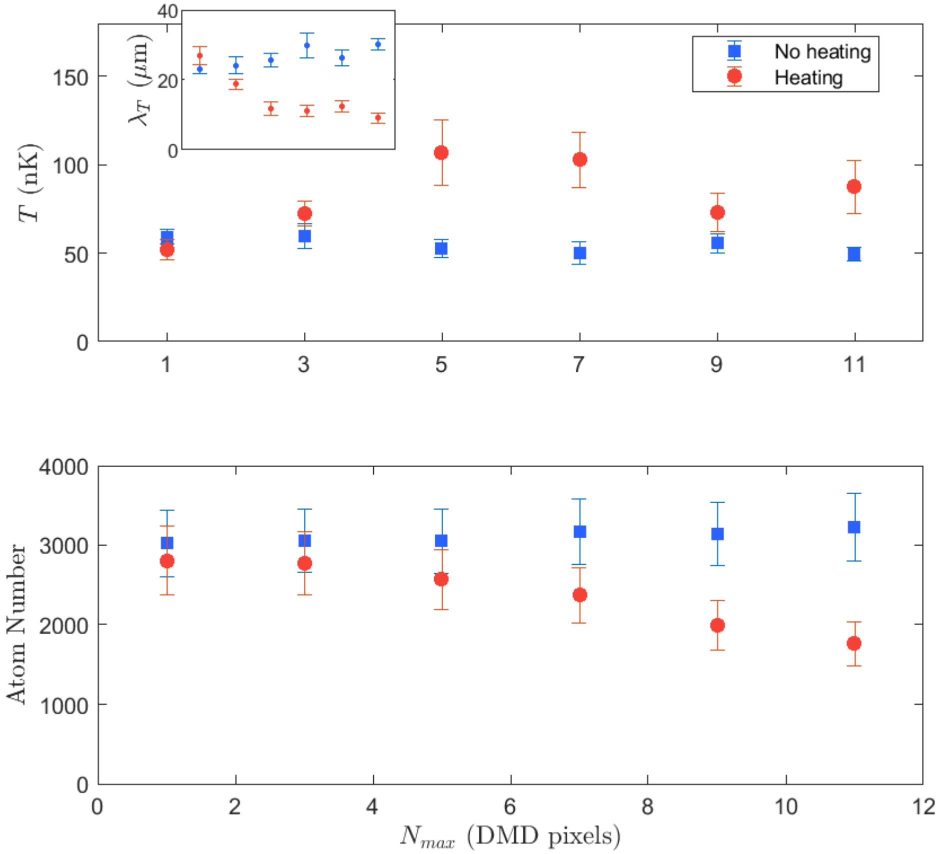

Figure 6.3: **Heating with different noise amplitudes.** Top: Temperature for each box after the heating procedure for different values of $N_{\max}$. The non-heated box shows the same temperature for the different values, indicating that it is not affected by the heating in the adjacent box. The heated box shows a significant higher temperatures for $N_{\max} > 3$. Notice that although the box is hotter when $N_{\max} > 5$, the temperature is similar or smaller than for the case of $N_{\max} = 5$. This is due to the fact that higher noise amplitudes don't conserve the number of particles in the heated box (see picture below). Bottom: Atom number in each box as a function of $N_{\max}$. Higher noise amplitudes ($N_{\max} > 5$) input enough energy for some atoms to leave the trap, this has implications in the value computed for the temperature.

ensure that all the relevant mode frequencies are addressed.

Experimentally the noise patterns are generated by turning on a random number of pixels in the columns that affect the region to be heated. This provides the ability of controlling how much the cloud heats up by tuning the amplitude of the noise (set by $N_{\max}$, the maximum number of pixels per column) and the amount of time that the heating procedure lasts. Increasing the heating period or amplitude will result in higher temperatures. It has to be taken into account that a very high noise amplitude results in a loss of atoms in the trap.

6.4 Theoretical description

Classically, if two similar gases under the same pressure at different temperatures establish contact, it is expected that they find there equilibrium state at a temperature which is the average of the two initial ones [48]. However, the 1D BECs used in the context of this work are integrable systems, meaning that thermalization is not expected to occur [114, 118]. It is thus interesting to investigate how the merging process of two gases at different temperatures evolves in time.

We may start such investigation by looking again at the Bogoliubov theory, introduced in section 2.1.2. This theory is dominated by the lower part of the energy spectrum and considers that the quasi-particles in the sytem propagate freely (the approximations used in this model are discussed below in 6.4.1). Assuming that the barrier and the merging time are small, we start by projecting the modes of the initial small boxes in the basis of the big box. The operators in the new basis read

$$\langle b_m^\dagger b_n\rangle = \frac{1}{n_{1\mathrm{D}}L^2}\sum_{j=p,q}\sum_{j=1}^{\infty}\left(\frac{E_j}{\epsilon_j}\sqrt{\frac{E_mE_n}{\epsilon_m\epsilon_n}}+\frac{\epsilon_j}{E_j}\sqrt{\frac{\epsilon_m\epsilon_n}{E_mE_n}}\right)I_{m,j}I_{n,j}\langle b_j^\dagger b_j\rangle, \tag{6.5}$$

$$\langle b_m b_n\rangle = \frac{n_{1\mathrm{D}}}{L^2}\sum_{j=p,q}\sum_{j=1}^{\infty}\left(\frac{E_j}{\epsilon_j}\sqrt{\frac{E_mE_n}{\epsilon_m\epsilon_n}}-\frac{\epsilon_j}{E_j}\sqrt{\frac{\epsilon_m\epsilon_n}{E_mE_n}}\right)I_{m,j}I_{n,j}\langle b_j^\dagger b_j\rangle, \tag{6.6}$$

where b_m is the anihilation operator for mode m of the full box, and $b_{p,q}$ is the corresponding operator for each of the small boxes. The subscript p and q are used to denote the mode indexes of the initially cold and hot boxes, respectively. The term $I_{i,j}$ is given by (more details in appendix D)

$$I_{i,j} = \begin{cases} \delta_{\frac{i}{2},j} & \text{if } i \text{ is even} \\ \frac{1}{2}\left[\frac{L}{\pi(i-2j)}\sin\left(\frac{\pi}{2}i-\pi j\right)+\frac{L}{\pi(i+2j)}\sin\left(\frac{\pi}{2}i+\pi j\right)\right] & \text{if } i \text{ is odd} \end{cases} \tag{6.7}$$

Note that minor quantum contributions were neglected.

Figure 6.4 shows the initial mode distribution in the basis of the full box. The distribution shows a GGE state [84], characterized by at least two temperatures, the higher one associated with the odd modes, which encode the temperature difference between the two boxes, and the lower one associated with the even modes.

Knowing the values of the correlators from equations (6.5) and (6.6), we can now compute the evolution of the phase variance. Using the general formula for the phase variance evolution [46], adapted to the specific geometry of the box trap used here, we have

$$\begin{aligned}\langle\Delta\hat{\phi}(z,z',t)^2\rangle = &\\ &\frac{1}{2n_{1\mathrm{D}}}\Bigg[\sum_{m=1}\mathcal{B}_{m,m}(z,z')(2\langle b_m^\dagger b_m\rangle+1)-(e^{-2i\omega_m t}\mathcal{B}_{m,m}(z,z')\langle b_m b_m\rangle+\text{H. c.})+\\ &\sum_{n=2}\sum_{\substack{k=1\\k\neq(n-k)}}^{n-1} e^{-i\delta\omega^-_{k,(n-k)}t}\mathcal{B}_{k,k-n}(z,z')\langle b_k^\dagger b_{n-k}\rangle+1)-e^{-i\delta\omega^+_{k,(n-k)}t}\mathcal{B}_{k,k-n}(z,z')\langle b_k b_{k,n-k}\rangle+\text{H.c.}\Bigg].\end{aligned} \tag{6.8}$$

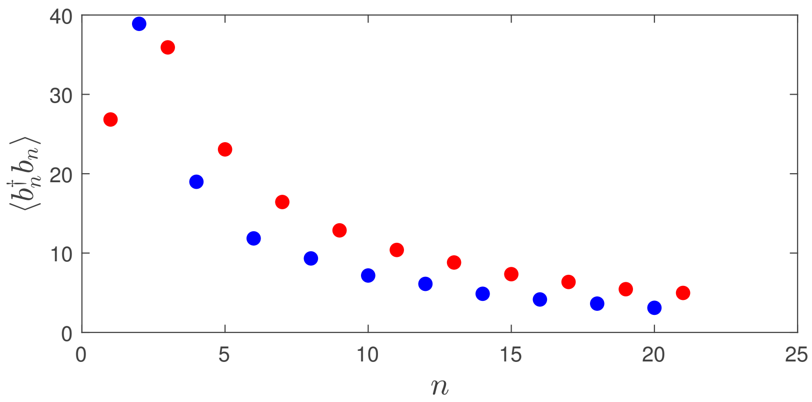

Figure 6.4: **Mode occupation in the full box:** The initial state consists of two boxes 50 µm long, with temperatures of 50 and 100 nK, with 5000 atoms each. Using the projection from equations (6.5) and(6.6), we get a distribution where the odd modes have a higher occupation than the even modes (except for $n = 1$). Such distribution is a GGE state, where even and odd modes have a thermal occupation with distinct temperatures.

The first and second summations account, respectively, for the diagonal and non-diagonal terms of the matrix

$$\mathcal{B}_{m,n}(z, z') = F_m(z, z')F_n(z, z'), \tag{6.9}$$

where the function $F_n(z, z') = \sqrt{\frac{\epsilon_n}{E_n}}\left(\cos\left(\frac{\pi n}{L}z\right) - \cos\left(\frac{\pi n}{L}z'\right)\right)$ relates the basis functions (2.14) in the two spatial coordinates. Furthermore, the frequency sum and difference $\delta\omega^{\pm}_{k,(n-k)} = \omega_{n-k} \pm \omega_k$, specify the time evolution for the non-diagonal elements of the $\mathcal{B}$ matrix. By inserting the result of equation (6.8) into equation (2.28), we can compute the time evolution of the phase correlation function.

For the low-momentum modes, which dominate the Bogoliubov theory, the energy can be approximated as $\epsilon_k = \hbar\pi cn/L$, providing a comensurate energy spectrum. Therefore, we expect these modes to dephase during the evolution and to rephase again at the recurrence time t_{rec} given by [21]

$$t_{\text{rec}} = 2L/c, \tag{6.10}$$

corresponding to the instant in which the first mode ($n = 1$) completes a full revolution. Figure 6.5 shows the phase correlation function calculated with equation (6.8) for a few relevant time instants. At $t = 0$ the system shows the two uncorrelated boxes. The difference in temperature between them is reflected on how fast the correlation decays in space. At $t_{\text{rec}}/4$ we reach the point where all the modes are dephased and the system resembles a thermal state. This coincides with the moment that the wavepackets introduced by the barrier reach the edges of the full box. Although globally the system is known not to be thermal, a local analysis disregarding points close to the boundaries can't distinguish between this actual state and a thermal one with the same temperature (see 4.3). At $t_{\text{rec}}/2$ all the even modes will

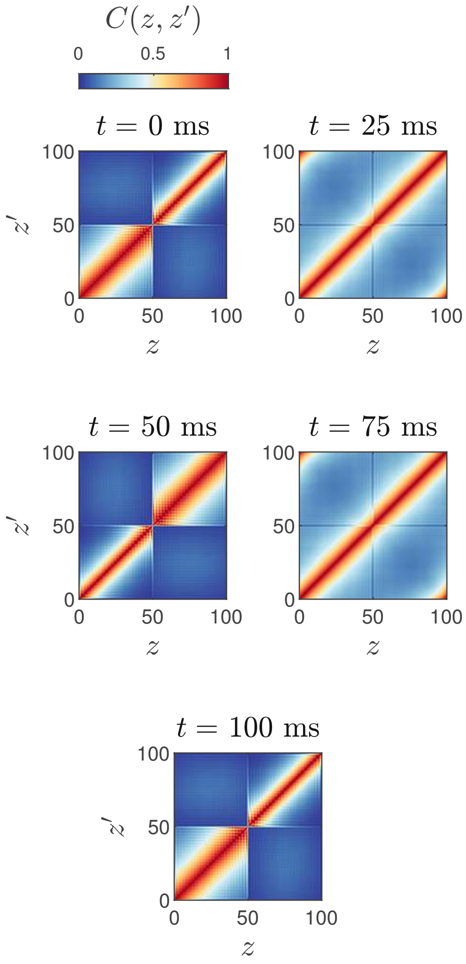

Figure 6.5: **Evolution of the phase correlation function:** Each plot shows the phase correlation function at an instant t, multiple of t_{rec}. At $t = 0, t_{\text{rec}}/2, t_{\text{rec}}$ the system shows the two uncorrelated boxes (with their spatial positions inverted at $t = t_{\text{rec}}/2$) due to the rephased mode interference. At $t = t_{\text{rec}}/4, 3t_{\text{rec}}/4$ the modes are dephased and the whole system resembles a thermal state (when the correlations at the edges are ignored). This evolution is obtained by projecting the individual mode distribution of each box in the basis of the full box. After this, the correlation function is propagated with equation (6.8). This example shows a box with length $L = 100\,\mu\text{m}$ and 5000 atoms, resulting in a $t_{\text{rec}} = 100\,\text{ms}$. The initial temperatures of each box are $T = 50\,\text{nK}$ and $T = 100\,\text{nK}$.

have completed a full rotation, while the odd modes rotated a half-integer rotation, reaching the "inverse" state relatively to the initial point. That explains the fact that, at this instant, we recover the uncorrelated boxes with different temperatures with their positions swapped. From this point on, the modes dephase again (we get a pseudo-thermal state at $3t_{\mathrm{rec}}/4$ as we did at $t_{\mathrm{rec}}/4$) and recover the initial state with the full rephasing of the modes at t_{rec}.

From a thermodynamic point of view, the evolution between $t = 0$ and $t = t_{\mathrm{rec}}/4$ can be regarded as heat flow, since the initial temperature gradient between the two halves of the system is not present at this stage and the system evolved to a state closer to thermality. The evolution away from this state to one where two regions of space are clearly distinguishable, can be interpreted as the ocurrence of anomalous heat flow, since there is an evolution towards a (apparent) less entropic state. This reading is valid from a local perspective, as the one adopted in section 4.2.1, when the state can not be distinguished from a thermal one if the effects of removing the barrier are not considered.

6.4.1 Limitations of the Bogoliubov theory

Some of the approximations used in the previously described model are not fulfilled by the circumstances in which the experiment is performed. Therefore, we will discuss the assumptions that are not respected and the consequences of neglecting them completely.

In this application of the Bogoliubov model it is assumed that the density is constant at all times. The merging procedure is implemented by removing a barrier that is infinitely thin. Therefore, the consequences of removing a real barrier (such as perturbations in the density) are not accounted for. Furthermore, removing the barrier is an irreversible process that might involve modes in the incommensurate part of the energy spectrum. It is also considered that the box trap has perfect walls. This is not possible to achieve in the experiment due to the limitations imposed by the optical systems that generate the trap (section 3.4.2). It is known that having a box potential whose walls have a finite width hampers the ocurrence of a perfect rephasing of the modes [40].

This theory was derived under the harmonic approximation, i.e., the Hamiltonian describing the dynamics is quadratic and does not consider higher order terms which might be important, considering the complex dynamics involved.

6.4.2 SGPE simulations

In order to understand the consequences of the merging procedure considering some of the experimental limitations, we perform simulations of such process with the SGPE method (see section 2.4.2). Contrary to the Bogoliubov model, SGPE allows to simulate conditions that suit some of the experimental apparatus limitations and also considers higher order terms that go beyond the quadratic approximation, which encode, for instance, phonon-phonon interactions. In this simulations we implement a 1 µm wide barrier which is removed in 5 ms, mimicking what actually happens in the experiment. Moreover, the box-potential considered has imperfect walls, with a width of 1 µm. The different temperatures for each box in the initial state is prepared by making the noise term η in equation (2.47) spatially dependent.

Figure 6.6 shows the full phase correlation function at different times for the 100 µm long box. The estimated recurrence time was calculated taking into account the barrier removal

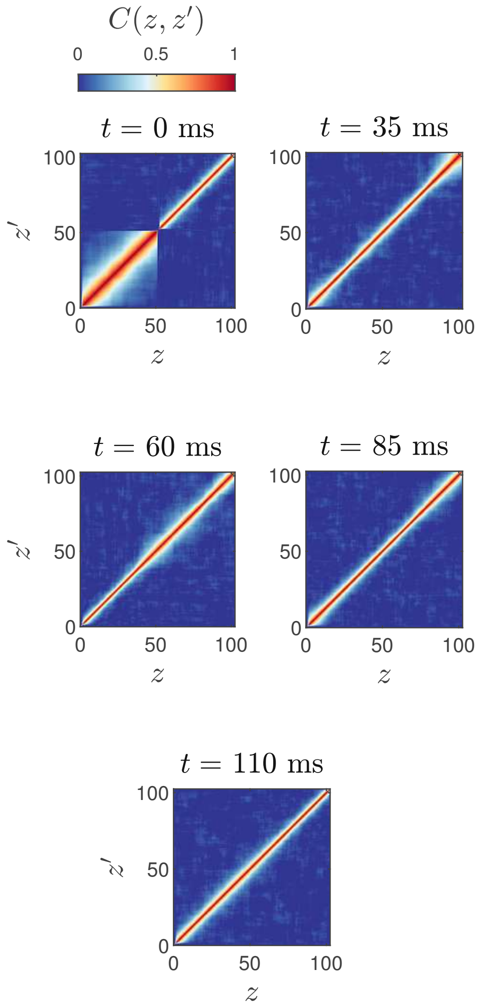

Figure 6.6: **Evolution of the phase correlation function under evolution with SGPE:** Each plot shows the phase correlation function at an instant t, multiple of $t_{\mathrm{rec}} + 10\,\mathrm{ms}$, accounting for the removal of the barrier starting at $t = 5\,\mathrm{ms}$ and lasting $5\,\mathrm{ms}$. At $t = 0$ the system shows the two uncorrelated boxes. After merging the two boxes, the rephasing of the modes as predicted by the Bogoliubov theory is not observed. Instead, the system resembles a thermal state whose temperature is close to the one of the initially hot box. The dispersive dynamics is explained by the terms of higher order consider in th SGPE equation. This example shows a box with length $L = 100\,\mu\mathrm{m}$ and 6000 atoms, mimicking the experimental parameters. The initial temperatures of each box are $T = 50\,\mathrm{nK}$ and $T = 100\,\mathrm{nK}$.

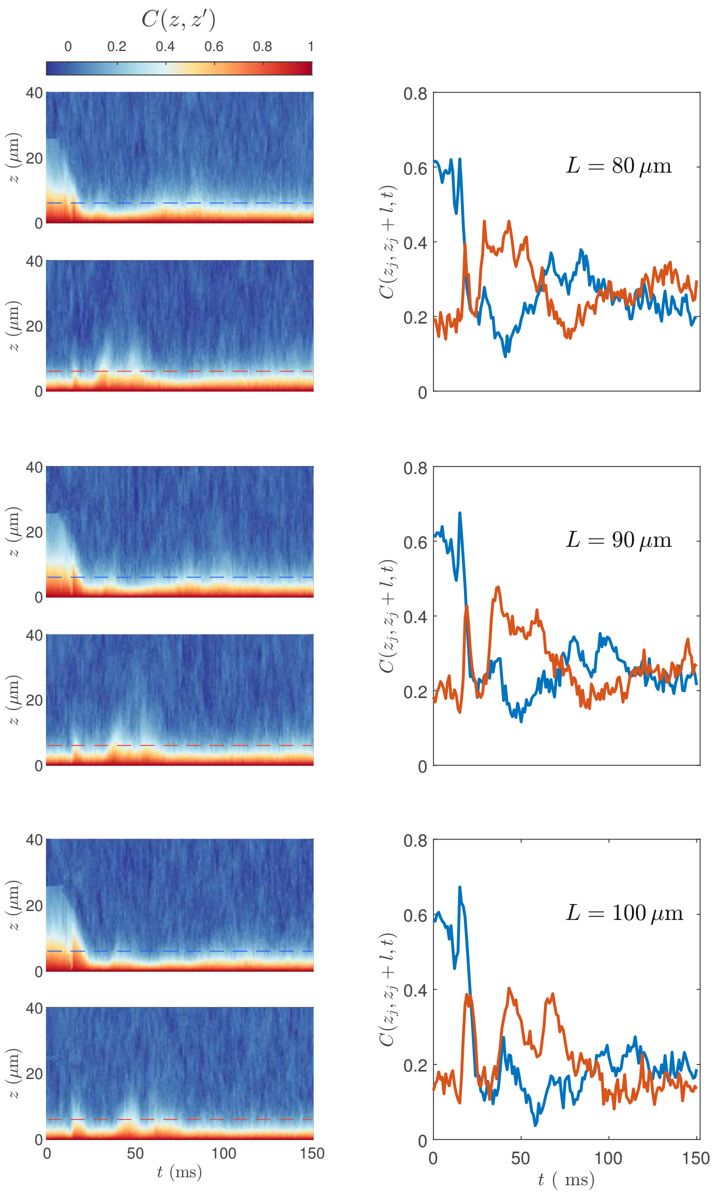

Figure 6.7: **Evolution of the phase correlation function for each box:** Each of the three rows of plots show the evolution of the correlation function for different box sizes. The carpet plots on the left show the evolution of the phase corrleation function in time and space, where the center of the cold (top) and hot (bottom) boxes are used as reference points. The plots on the right show the same quantity where the second point was fixed at a distance $l = 6\,\mu\text{m}$ from the box center. The parameters used in this simulations are the same as the ones mentioned in 6.6

time (5 ms). In comparison with Bogoliubov theory, it is clear that the recurrent behaviour of the system is not as clear as the one shown in figure 6.5. It is possible to observe that, at $t = 35$ ms where the system is closer to thermality, the correlation function shows a peak at the box edges, as before. At $t_{\text{rec}}/2$, the scenario is different from the inverse state provided by the half-integer rotation of the odd modes. Here, although the correlation function displays larger values on the right side of the box, they are not as high as the ones exhibited by the hot box in the beginning. Afterwards the system is barely distinguishable from a thermal state even at t_{rec}. It is interesting to observe that at $t = 75$ ms, the peaks on the correlation function associated with the wavepackets introduced by the barrier removal are not present. The dispersion of these wavepackets can be explained by the higher order terms considered in this simulation (and neglected by the quadratic theory).

To investigate more closely the evolution of the correlation function under the SGPE, we look at the evolution in time and space of $C(z_C, z, t)$, where z_C is a reference point centered in the cold box. Figure 6.7, shows the evolution of $C(z_C, z, t)$ for three different box lengths. The initially hot box becomes colder in time, and the opposite happens for the cold box. This behaviour seems to invert, leading to a state which is qualitatively closer to the initial one, where the initially colder box is again the coldest. This evolution is more easily observed for the smaller boxes, due to the smaller recurrence times.

Even though these simulations account for some experimental imperfections, there are more factors (such as atom number fluctuations or trap heating) which have not been contemplated. In section , a discussion about these imperfections as well as a comparison between the simulated and experimental data is presented.

6.5 Experimental results

Figure 6.8 shows an example of the phase correlation evolution after the barrier that separates the two halves of the system is lowered. For the initial state ($t = 0$ms) the difference in temperature between the two small boxes is clear. The left box ($z < 0$) shows a longer coherence length when compared to the right box (z $>$ 0). The corresponding computed temperatures are, 49 nK and 75 nK, respectively. It is also visible that there are no correlations between the two boxes. After the barrier is completely removed ($t = 9$ ms), the correlations in the colder box start to fade away, while in the hotter box there seems to be a slight increase for the first instants after the merging procedure is complete. For later times, the phase correlations of the whole system resemble those of a thermal cloud in a box potential. The evolution of the phase correlation is similar the one computed by the SGPE in section 6.4.2.

Choosing specific regions of space to investigate how the phase correlations evolve in time allows to find out whether there are recurrences holding evidence of memory of the initial state. To analyze the time evolution of the correlation functions, we average n points to compute the average $\bar{C}(z, z', t)$ of $C(z, z', t)$ in each region

$$\bar{C}(z, z', t) = \frac{1}{N} \sum_{z,z'} C(z, z', t), \quad z, z' \in [z_{min}, z_{max}] \tag{6.11}$$

where z_{min}, z_{max} define the region under consideration. Figure 6.9 shows the evolution of the averaged correlations $\bar{C}(z, z', t)$ for three boxes with different length L (after merging).

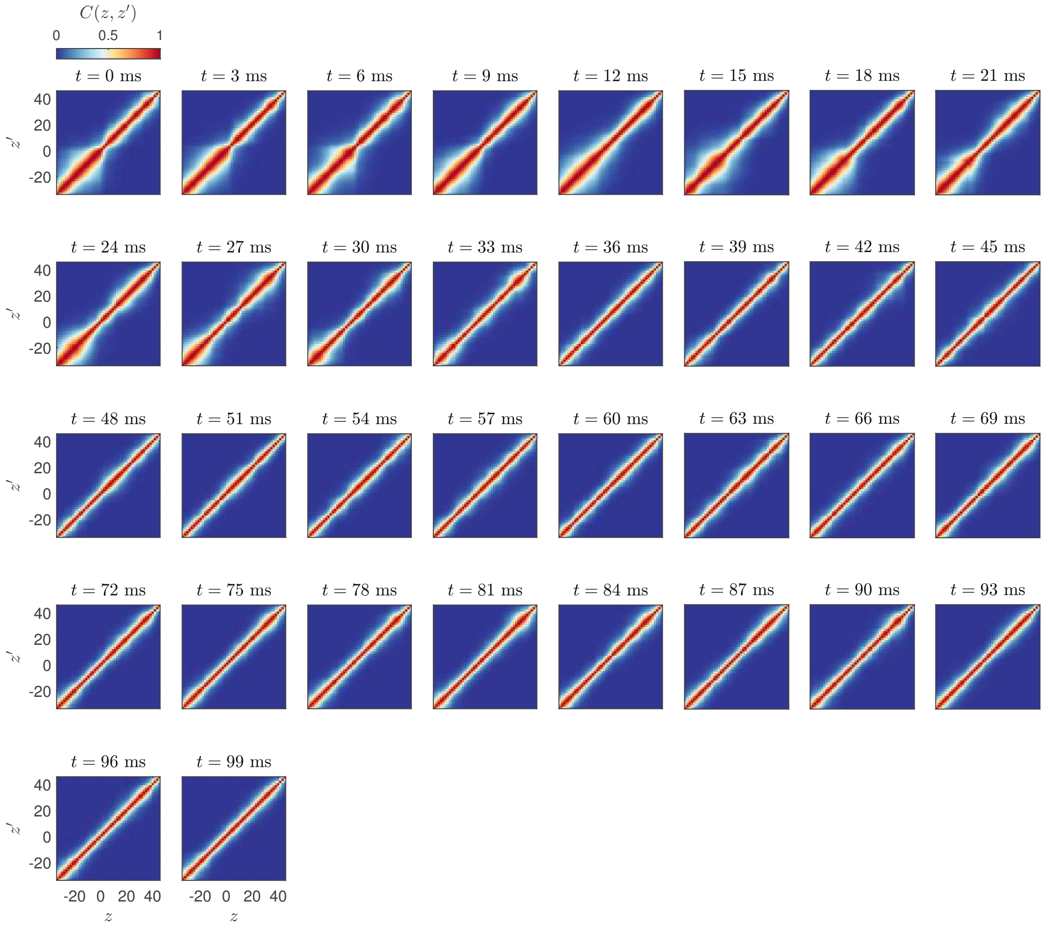

Figure 6.8: **Phase correlation evolution in time:** Each small box is 40 µm long and they are separated by a 1 µm barrier which is removed in 9 ms, starting at $t = 0$ ms. The temperatures measured for the cold and hot box are, respectively, 49 nK and 75 nK. The total number of atoms is $N = 5000$, equally distributed by both boxes in the beginning. The expected recurrence time is $t_{rec} = 49$ ms.

The heating procedure to achieve the initial temperature gradient between the small boxes is the same for each data set. The colder box starts at an initial temperature $T \sim 50$ nK whereas the hot box shows approximately double the temperature ($T \sim 100$ nK). We compute the value of $\bar{C}(z, z', t)$ for a region encompassing the points belonging to each of the initial small boxes in the initial state.

In any of the three cases shown in figure 6.9 it is clear that each small box have distinct levels of correlations in the beginning. After the barrier is removed, the average value of the correlation in the cold box decreases. After achieving the minimum at $t_{\mathrm{rec}}/2$, the correlations seem to stay around the value of 0.6 for the remaining instants for the larger lengths. When $L = 80, 90$ µm, the value of the correlations goes up slightly close to the recurrence time. This is evidence that there exists some memory of the initial state. Observations for the initially hotter box are less clear. The correlations start at a lower value and seem to increase slightly

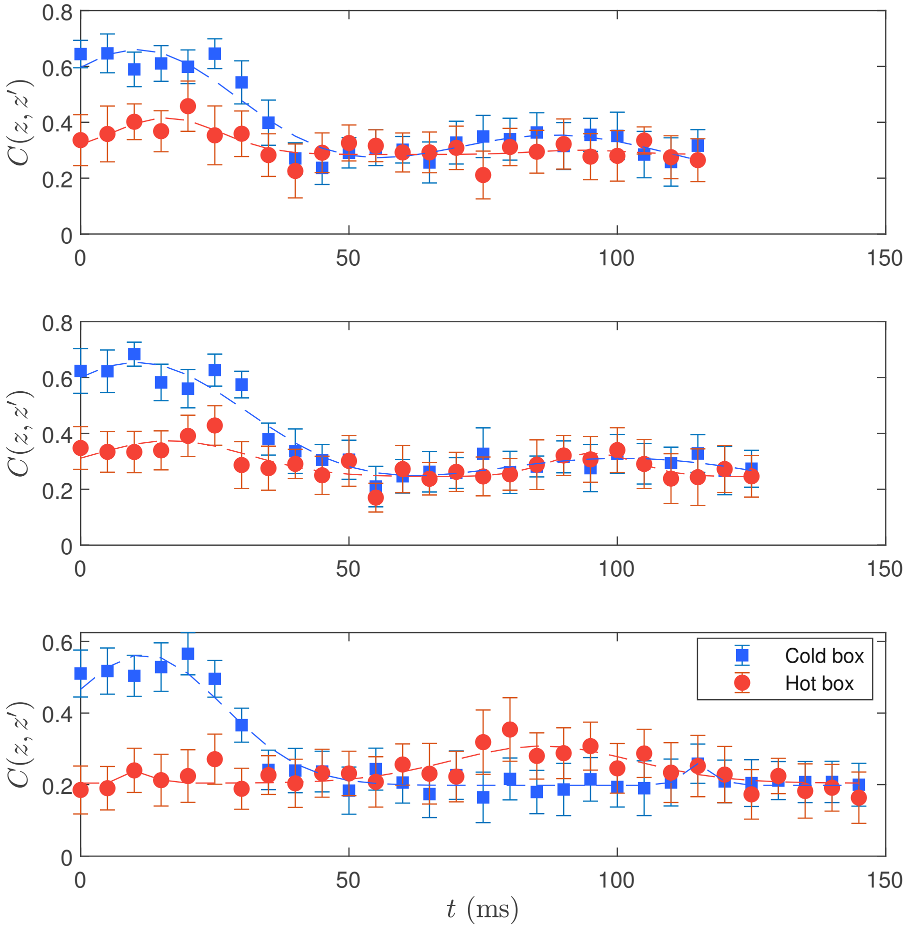

Figure 6.9: **Averaged phase correlation evolution:** The total length of the full box is, from top to bottom, $L = 80\mu\text{m}, 90\mu\text{m}, 100\mu\text{m}$, respectively. The heating process is performed such that (for all three values of L) the temperature of the cold box is $T = 50\text{nK}$ and the hotter one is $T \sim 100\text{nK}$. The total evolution time is proportional to the value of L. For $L = 80\mu\text{m}, 90\mu\text{m}, 100\mu\text{m}$ the total evolution time is, respectively, $115, 125, 145\text{ms}$. The value of $\bar{C}(z, z', t)$ was calculated with pairs of points close to the center of each box.

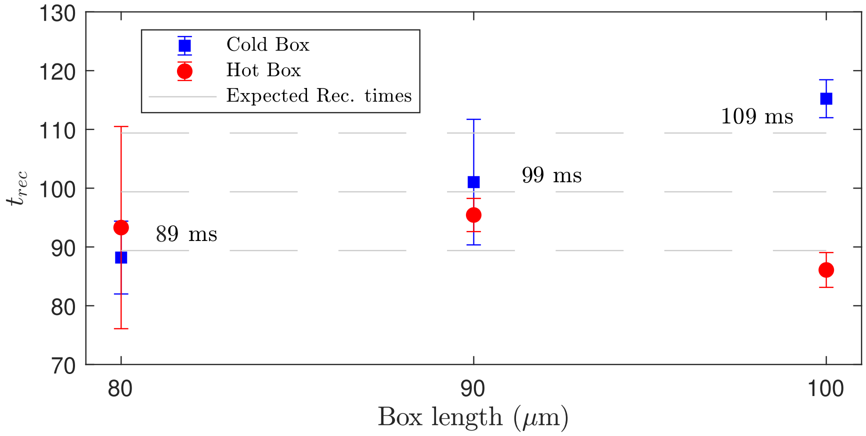

Figure 6.10: **Fitted recurrence times for different boxes.** The recurrence times were extracted through fitting, using equation (6.12). The blue dots show the times resulting from the analysis of the correlations in the cold box, while the red points show the same quantity regarding the hot box. The gray dahsed lines (as well as the aiding texts) show the times predicted by the Bogoliubov theory for each box size. The correlations in the colder box seem to provide more reliable predictions fot the recurrence times, showing that there is some preserved memory of the initial state.

in the first 30 ms of evolution. After that the value tends to go back to the initial one and remains approximately constant for the remaining instants. Interestingly, for the $L = 100\,\mu$m box, there seems to be an increase of the correlations in the hot box starting around 75 ms. Although delayed in time, this behaviour seems to agree qualitatively with the predictions from the SGPE simulations.

The theoretical predictions agree about the qualitative behaviour of the cold box, while measured correlations regarding the hot box don't match the theoretical predictions. It should be considered that the results presented in section 6.4.2 don't account for the effects of the imaging system, nor other experimental imperfections (see 5.4). This kind of effects limits the amount of features observable on the measured data.

It is possible to further analyze the time evolution of the correlations, to find out if the second peak observed for the cold box relates to the expected recurrence times in each different box. Figure 6.10 shows the recurrence times obtained by fitting the function

$$f(t) = a \cdot e^{-\frac{1}{2}\left(\frac{t-b}{c}\right)^2} + d \cdot e^{-\frac{1}{2}\left(\frac{t-e}{f}\right)^2} + g, \tag{6.12}$$

where the fitting parameters are represented with the letters a–f. The fitting parameter e corresponds to the recurrence time introduced in 6.4. The resulting fitting curves obtained with this function are shown with dashed lines in figure 6.9. The recurrence times extracted by fitting the phase correlations in the cold box yield results close to the ones expected theoretically. In this specific case, we compute the recurrence time using equation (6.10) and adding 9 ms to account for the barrier removal. Applying the same analysis to the colder box returns less clear results. The fitted recurrence time for the largest box is off by 20 ms. The 80 µm box shows a value that, although not far from the expected one, yields a very high uncertainty. The fact that the correlations are considerably lower in the beginning (due to a higher temperature) and the additional heating due to the barrier removal make recurrent phenomena harder to observe. Nevertheless, the results obtained for the cold box, provide good evidence that some memory of the initial state is still present.

6.5.1 Application of the local thermometry method

To investigate how the energy is distributed over the system, we use the local thermometry method introduced in section 5. By computing a temperature for specific regions of the full system, it is possible to map the energy distribution, assuming that the assigned local temperature is a good proxy for that quantity. The heat flow is then measured by looking at how the temperature changes in each of the chosen regions of observation. For the purpose of the work presented here, we select two regions, each one centered around the middle point of one of the small initial boxes.

Figure 6.11 shows both the temperatures and the fitted decay lengths used to compute them. It is clear that the temperatures are distinct in the beginning for the three different lengths. After the barrier is removed, the temperatures in both regions increase. This increase is steeper for the region associated with the cold box, since its initial temperature is lower. Notice that most of the effective local temperatures after the barrier removal are not valid to be interpreted as such. This is expected due to the propagating wavepackets introduced by the barrier. These make the density non-homogeneous in the regions of analysis, breaking one of the criteria to do local thermometry. From this point on, the effective local temperatures on each region seem to converge to a value that is higher than the initial ones. From this fact it can be deduced that the energy introduced by the barrier can't be neglected and heats up the system significantly, enough for the final temperatures of each box to be larger than the initially hotter temperature.

Performing local thermometry in these circumstances leads to a considerable amount of uncertainty, as demonstrated by the T_{err} errorbars in figure 6.11. Furthermore, many of the effective local temperatures extracted are not valid due to the limitations of the imaging sytem or the complex non-equilibrium state after the merging of the two clouds. This makes the analysis of the dynamics more difficult, however, most of it is more clearly encoded on the values of λ_D.

The initial behavior exhibited by λ_D is the inverse of the one described for the local effective temperatures, as expected. After the barrier removal, they converge to a value close to 6 µm. Close to $t_{\mathrm{rec}}/2$, we observe a higher value for the hot region, relatively to the one recorded for the cold region. This is an inversion of the relative positions compared to the initial state, matching the prediction that the relative magnitude of the two regions should swap. This is a signature of a heat flow towards a thermal state (when the two values converge after the barrier removal), followed by a departure from such state through an anomalous heat flow (when the values of λ_D diverge). From this point onwards, the values of the two regions converge again and seem to remain close to the value of 5 µm.

To confirm whether the experimental data points corroborates the theoretical predictions, we compare the results of the local thermometry method applied to the experiment and both

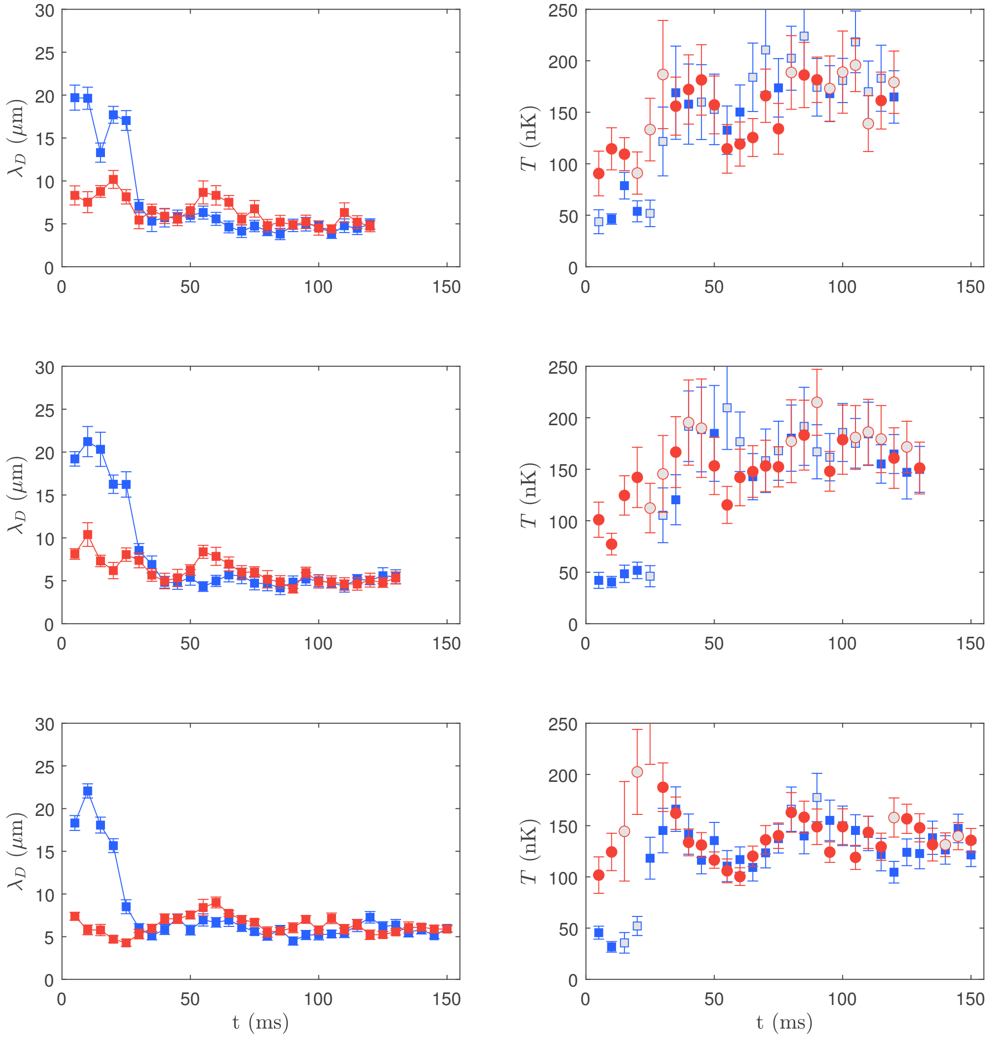

Figure 6.11: **Local thermometry analysis:** Each rows shows the results of the local thermometry method for different times for a region at the center of the initially cold box (blue) and hot box (red). The first column shows the extracted phase decay lengths λ_D for these regions. From these values, the effective temperatures T_{eff} are calculated, taking into account the density of the condensate at that moment. The points filled in gray show the time instants where interpreting the calculated value of T_{eff} as a local effective temperature is not valid (the validity criteria is described in Chapter 5).

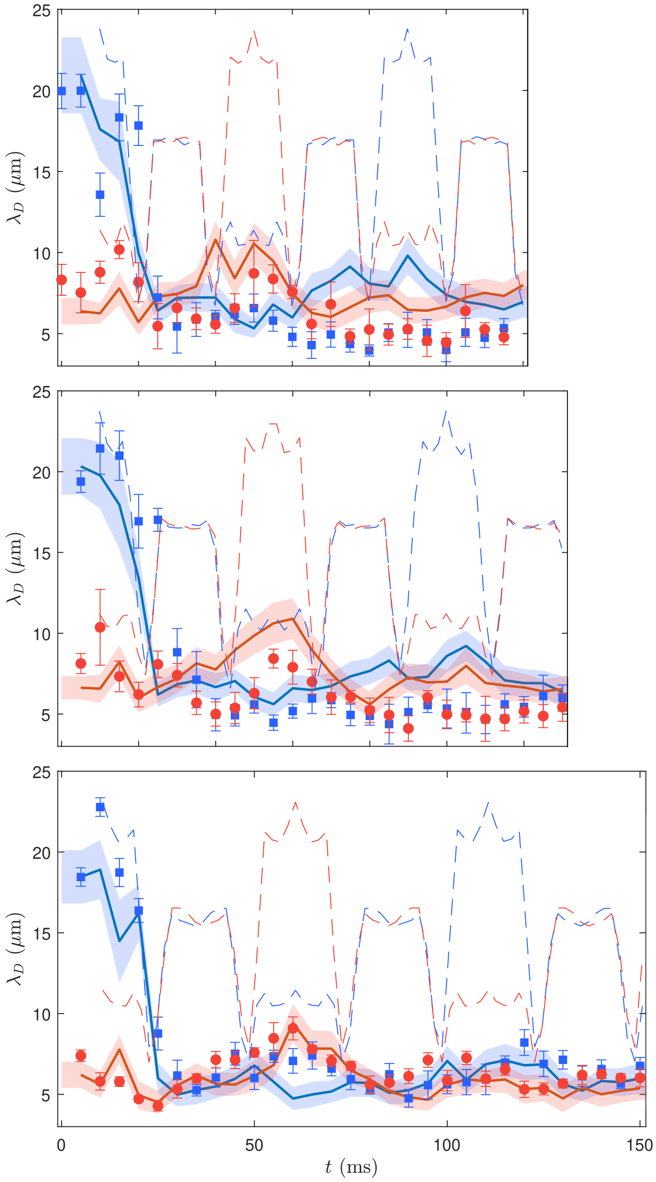

Figure 6.12: **Comparison between experimental and simulated data:** Evolution of the decay length λ_D in time for Bogoliubov theory (dashed lines), the SGPE (solid lines) and the experimental data (sqare and rounded points). The blue color refers to the λ_D in the initially colder box, while the red color is associated with the remaining box. For each lenght ($L = 80, 90, 100\,\mu\text{m}$, from top to bottom) six values over the length of each box are averaged. The shades around the SGPE predictions indicate the statistical uncertainties found for this method. For these simulated values, the effects of the imaging system were accounted for. All the errorbars and uncertainty levels indicate a confidence interval of 68%.

SGPE and Bogoliubov theory predictions. Figure 6.12 shows clearly that the Bogoliubov theory is far from capturing the dynamics happening after the barrier removal. The results obtained from the SGPE equation provide a much more accurate prediction, showing the damped inverted state at $t_{\text{rec}}/2$ and a path to thermalization afterwards. Such a result implies that the damping of the oscillations of λ_D are due to the higher order terms neglected in the Bogoliubov theory.

6.5.2 Evolution of the common density

We've been mainly concerned with the relative phase degree of freedom, since this is our main probe into the system dynamics. It is also possible to observe the consequences of coupling the two atom clouds by measuring the common density.

Figure 6.13 shows the evolution of the common density before and after the merging procedure. The consequences of removing the barrier are visible through the light cone propagation of the two emerging wavepackets. It is also clear that these perturbations decay in approximately 25 ms, matching approximately the time they take to be reflected by the box walls.

It is interesting to analyze the density evolution while the boxes are being merged (figure 6.13 b)). Notice that although the height of the barrier was decreased linearly (by decreasing the number of pixels that compose it), the behaviour of the density at the merging point does not seem linear. At $t = 3\,\text{ms}$, when the barrier has one third of the height, the density seems not to notice the change in the potential. In the following instants, the density behaves as expected, leading to a full atom cloud with no defined separation. This indicates that there is a delay between the time at which the barrier is lowered and the time at which the density reacts to the change in potential (notice that at $t = 9\,\text{ms}$ the barrier still appears to be present, even though it has been removed already). This matter requires further investigation that is not pursued here.

6.5.3 Discussion

The comparison between the theoretical and experimental results shown in figure 6.12 shows clearly that the Bogoliubov theory is not enough to make accurate predictions about the consequences of coupling two adjacent atom clouds. On the other hand the results obtained with SGPE capture the dynamics of the system more accurately, even if some of the events (such as anomalous heat flow, for instance) seem a bit delayed or different in magnitude. It is interesting to discuss why this is the case and to point out what are the sources that explain these differences. Some of these sources stem from experimental limitations, while others arise due to the many-body physics taking place.

The atom number in each realization of the experiment fluctuates, which makes the speed of sound differ for different realizations. Since the speed of sound depends on the density, it will also change every time a measurement is performed. This makes the rephasing of different modes less coherent, since there recurrence time depends on the speed of sound as well. The typical standard deviation for the atom number rangers from 10–15% of the average. The phase correlation function computed to analyze the dynamics is an average over the different realizations. As a consequence, some recurrent phenomena might not show

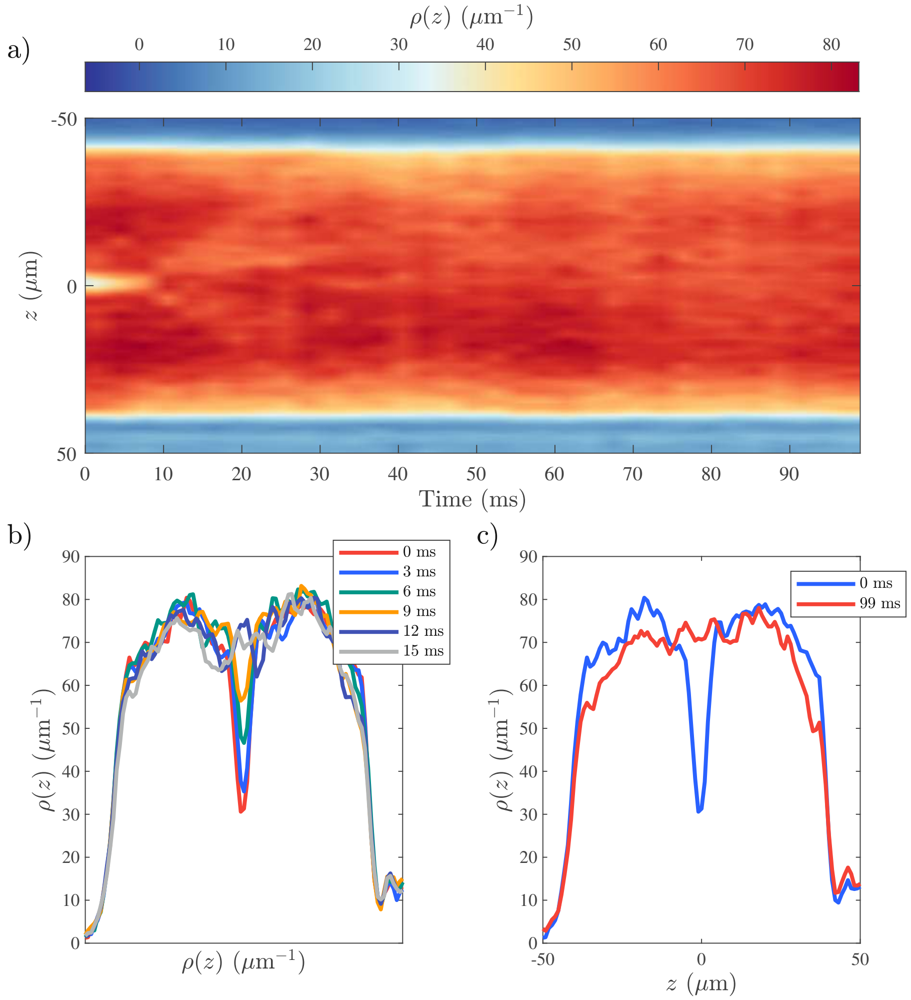

Figure 6.13: **Common density evolution:** Merging two 40µm long boxes. The colder box has a temperature $T = 50\,\text{nK}$, while for the hotter one $T = 70\,\text{nK}$. The merging starts immediately after the initial state is prepared and lasts 9 ms.

up as clearly as in the simulated data (notice the smaller difference in λ_T at $t_{\mathrm{rec}}/2$ for the $L = 100\,\mu\mathrm{m}$ box, for instance). Post-selecting the data mitigates this effect but it is never completely overcome. Due to the long measurement times, there is some atom loss in the box trap. This also plays a role on the fact that at the last instants of evolution, the system dynamics is more difficult to predict. In the data presented here, the atom loss is always 10% or less.

An imbalance in the number of atoms in each of the longitudinal clouds can induce a coupling between the relative and the common degrees of freedom [89]. Before the measurements performed here, the number of atoms in each well was optimized such that the imbalance would be minimal.

The imperfection of the box potential are another source of error that induces damping in any recurrent phenomena. The steepness of the box walls not only weakens the validity of the perfect-box approximation (used in the Bogoliubov theory) [40], it also contributes significantly for the dispersion of the propagating quasiparticles in the condensate (see 6.13 *a)*). This effect is, however, considered in the SGPE simulations. On the other hand, the box is not perfectly flat, due to the limitations of the optimization process (section 3.4.2). Despite this technical imperfection, the optimization error is bounded in 10% which should not affect the present results significantly.

The results of figure 6.12 shows that the Bogoliubov theory, dominated by the low energy part of the spectrum, is not enough to describe the dynamics after the merging protocol. This suggests that the evolution subsequent to the barrier removal is highly influenced by the higher terms that go beyond the quadratic approximation. Although these can be studied numerically with the GPE equation, it is hard to describe what role each scattering term plays in the merging of the two atom clouds. Indeed, the exact consequences of driving two uncorrelated atom clouds into the strongly coupled regime (a complete barrier removal) remain unclear. This problem has some parallelism with the one that the Kane-Fischer model [119] tries to solve. This model is meant to describe transmission through barriers in interacting one-dimensional electron gases. However, the common techniques used to approach it are not suitable for the setup presented here [120, 121] . Other works have attempted to tackle the interaction between adjacently coupled BECs with their analysis regarding the weak coupling regime only [122, 123].

The local thermometry method is essential to study the kind of dynamics induced by the merging procedure. It requires a local analysis with a proxy variable to energy that allows deriving conclusions about its distribution over time. The system dynamics seems to be well captured by the decay lengths λ_D. Both in theory and experiment, these values are precise enough to observe the expected features of heat flow and anomalous heat flow. Even though at t_{rec} the system is expected to recover partially the initial energy distribution (i.e., the initial colder box becomes colder again), this becomes increasingly difficult to measure experimentally due to the limitations described above, inherent to the experimental apparatus.

On the other hand, the associated local effective temperatures don't allow a similar analysis due to the lack of precision of the computed values. This is a consequence of the temperature interval in which the experiment is performed. The temperatures measured in the different experiments range from $40 - 150\,\mathrm{nK}$. Due to the limitations of the imaging system, no temperatures above $150\,\mathrm{nK}$ can be measured reliably. For higher temperatures the precision of T_{eff} decreases significantly due to the inverse proportion relation to λ_D. Since the energy in the system increases significantly after the barrier is removed, it is hard to evaluate, in detail, the behaviour of the system after this event, based on the values of T_{eff} only. It is enough, however, to claim that for long evolution times both regions show the same temperature, one higher than the ones in the initial state.

Starting this procedure with colder atom clouds could make the observation of expected features more clear. However, this was not possible to achieve, since the lowest temperatures that can be reached in the box trap were $\sim 40\,\text{nK}$. Smaller boxes would also provide better results, because the recurrence time would be smaller, leading the quasiparticles to disperse less and reduce the incoherence brought about by the experimental imperfections. Nonetheless achieving smaller boxes with the dipole light makes the cooling in the atomchip trap less efficient and the temperatures achieved in the initial state are not low enough to have conclusive results.

6.6 Summary

We've seen that studying the merging protocol is interesting to investigate the thermodynamics of a 1D many-body system and its implementation is also a relevant milestone for a future implementation of a QFM. We implement the merging protocol by coupling two uncorrelated clouds adjacent to one another in a head-to-tail configuration. Initially the clouds have different temperature, so that, once they are merged, a redistribution of energy, here denominated heat flow, takes place during the joint evolution.

It is possible to create a temperature imbalance in two uncoupled regions of the condensate through a local heating technique. To increase the energy of a specific cloud, white noise is shined on the targeted spatial region for a controllable period of time and amplitude. Both these parameters will influence how much the cloud heats up. In the examples shown here, the colder box starts close to a temperature of $40-50\,\text{nK}$ and the hotter one is approximately $100\,\text{nK}$.

The initial prediction for the observation of anomalous heat flow is provided by the recurrent behaviour expected by the Bogoliubov theory, where the dephasing and rephasing of the modes will take the system to a state closer to thermality and restore the initial state after the recurrence time t_{rec}, when all the modes have completed an integer number of complete rotations simultaneously. The predictions provided by the Bogoliubov theory are however not accurate due to the very strict approximations required. Simulating the same merging protocol using the SGPE, allows not only to consider some experimental limitations in the numerics but also take into account higher order terms which play an significant role on the dynamics subsequent to the barrier removal.

The experimental results agree with the SGPE predictions, even though there are some deviations regarding timings and the magnitude of some events. These can be explained considering some experimental limitations, the most relevant being the atom number fluctuations, the high temperatures in which the experiment is performed and the limitations of the imaging system. Despite these imperfections, these results hold the first observation of anomalous heat flow on a many-body system. This is of utter importance, for it holds a fruitful investigation bridging fields of Cold Atoms, Many-body and Quantum Thermodynmics, more specifically, we drive two systems into the strong coupling regime, a regime that is usually not tackled theoretically.

Chapter 7

Outlook

This thesis aimed at introducing the concept of Quantum Field Machine (QFM), a type of heat engine that operates at the quantum level implemented in a quantum many-body system that requires statistical considerations to describe its dynamics. Furthermore, the entrails of the machine were numerically and experimentally investigated, paving the way to a full implementation in the future and opening new questions regarding the thermodynamics of quantum systems in 1D.

Chapter 4 motivates the need for the concept of a genuinely quantum heat engine, a device that performs a specific task, requiring quantum mechanics and thermodynamics simultaneously for its behavior to be described. The QFM is then decomposed in its basic primitive operations, namely, compression/expansion (playing the role of the classical piston) and merging/splitting (playing the role of a valve at the quantum level). Each of these primitives is implemented using the Tomonaga-Luttinger Liquid (TLL) model and explored individually. It is concluded that under a slow enough change of length of the machine's component, the system can be driven out of equilibrium and restored to the initial situation if the reverse operation takes place. The splitting/merging primitive is the one allowing energy exchange between two components of the machine. It was found that this kind of operations introduce extra energy in the system in the form of counter propagating wavepackets. This however, doesn't prevent the exchange of energy to happen. Indeed, it is demonstrated that reducing the energy of the piston component is possible by compressing, coupling it to the bath and decompressing it to the initial length. This process is used several times between different pairs of components to decrease the energy of the System by 9% after three cycles. Due to the finite size of the machine, the cooling power will be exhausted in a finite number of cycles. This is one of the interesting observations of performing thermodynamics far from the thermodynamic limit [29].

After the numerical study, an experimental proof-of-concept implementation of each primitive was provided. Compression/expansion were implemented by moving the walls of the box symmetrically inwards or outwards, respectively. Even if the process was carried on slower than the typical time scales of the system, perturbations due to the wall movement could not be avoided. Although changes in length close to adiabaticity could be achieved, the presence of these perturbations do not allow the system to be restored to the initial state as predicted by theory. This poses severe limitations to a full implementation of the machine, since compression and expansion don't seem to be reversible at the time scales that allow a feasible experimental realization of such machine. Nevertheless, it has to be taken into account that this primitive is performed in a linear fashion which might not be the optimal way to do it. Optimal Control Theory (OCT) can be used to optimize the time-dependent operations [102, 124].

Although the experimental implementation of the full valve is not shown in chapter 4, a demonstration of the coupling control between two adjacent atom clouds is demonstrated. Some brief theoretical considerations regarding the decay of correlations before and after barriers of different strength are provided. The high temperatures found in the experiment didn't allow to clearly observe a match between such considerations and the experimental data, however, the different coupling strengths between the two clouds could be demonstrated.

In chapter 5.1 a method to measure temperature locally is presented. The motivation behind the development of such a method is the ability of having an effective temperature associated to different (uncorrelated) regions of space. This way, it is possible to use the effective temperatures as a proxy to energy and map its distribution over space and time. This is a crucial tool to study the evolution of systems in a situation far from equilibrium. For a local effective temperature to be measured in a specific region of space, the system has to appear thermal inside that region. In other words, the density of the condensate should be homogeneous and the decay of the phase correlations has to be exponential (the region should be on the order of the phase decay length, or larger). This method is better suited for lower temperatures, due to the big uncertainties obtained otherwise. Furthermore, the resolution of the imaging system has to be taken into account, for it sets an upper bound on the temperatures that can be measured with this method.

Chapter 6 looks at the implementation of the merging process studied before numerically. The purpose of investigating the coupling of two (initially uncorrelated) thermal clouds which exhibit different temperatures. The motivation is justified regarding its importance both to characterize one of the primitive operations of the QFM and the possibility to probe interesting quantum thermodynamics phenomena (e.g. anomalous heat flow). After detailing how the procedure is carried on, the process is modeled using the Bogoliubov theory and simulated with the SGPE. It is clear that the lnearized theory fails to capture most of the dynamics taking place after the two atom clouds are merged. On the other hand, the results obtained from the SGPE can predict the evolution of the phase decay length λ_D, used for local thermometry, showing that a quadratic approximation is insufficient to describe the merging procedure accurately.

The results presented throughout this thesis show that the implementation of a full cycle of the QFM is a big challenge. The simplest experimental realization of single primitives revealed that the smooth operations (like compressing/expanding) induce non-negligible perturbations in the system that make difficult achieving the goal of cooling down part of the system. Besides perturbing the system, processes described here have to be implemented quickly enough, otherwise, long cycles hinder a feasible experimental implementation due to lack of stability for long time scales (typically the experiments carried on in our platform don't last more than 200 ms). Nonetheless, the attempts at implementing the primitive operations demonstrated here were the first step, performed in a simple fashion. Further optimization using OCT techniques and alternative ways of performing the desired tasks are still to be explored. As an example, the coupling between atom clouds for energy exchange purposes might only require a small decrease in the barrier strength instead of the full removal.

Even if the implementation of a QFM cycle is deemed infeasible, this platform is still interesting to tackle interesting problems from a quantum thermodynamics point of view. The strong coupling of two initially uncorrelated condensates is an example. To the best of our knowledge, there isn't a model that describes this type of strong, finite, local coupling. Furthermore, attempts at computing information-theoretic quantities for a quantum many-body system have been successfully attempted [109]. This shows how versatile this platform can be and how it gathers a physical system that allows to explore complex and rich physics in regimes usually not available experimentally or not tackled theoretically.

Appendix A

Details on the QFM numerical study

In this appendix we provide details on the implementation of the numerical simulations of the QFM, presented in chapter 4 . Although the next sections offer enough information to understand how the TLL model was simulated, some of the details were left out for the sake of simplicity. Some of these technicalities are out of the scope of this work, however, they can be found in the appendices of reference [29] .

A.1 Gaussian models in simulations of primitive operations

The continuous Hamiltonian given in eq. (2.45) can be appropriately discretized, which we explain in Section . The system can then be described in terms of quadrature operators, in particular, one can describe the quantum states and dynamics with the Gaussian framework of covariance matrices and symplectic transformations. In this section, we present a short summary of the formalism of Gaussian quantum information, see, e.g., references [125, 126] for more complete reviews on the subject.

We consider bosonic systems of N bosonic modes, associated with quadratures

$$\hat{\mathbf{X}} := (\hat{q}_1, \hat{q}_2, \ldots, \hat{q}_N, \hat{p}_1, \hat{p}_2, \ldots, \hat{p}_N)^T \tag{A.1}$$

that can be seen as the N position and momentum operators, respectively. The canonical commutation relations can be captured as $[\hat{X}_l, \hat{X}_m] = i\Omega_{l,m}$ for $l, m = 1, \ldots, N$, giving rise to the symplectic form

$$\Omega = \begin{pmatrix} 0 & \mathbb{1} \\ -\mathbb{1} & 0 \end{pmatrix} . \tag{A.2}$$

Given a density matrix $\hat{\gamma}$, we define the vector of mean values $\bar{\mathbf{X}} := \hat{\mathbf{X}}_{\hat{\gamma}} = \mathrm{tr}(\hat{\gamma}\hat{\mathbf{X}})$: these are the first moments of the set of quadrature operators $\hat{X}$ corresponding to the quantum state. The second moments can be collected in the covariance matrix with entries

$$\Gamma_{i,j} := \hat{X}_i\hat{X}_j + \hat{X}_j\hat{X}_{i\hat{\gamma}} - 2\hat{X}_{i\hat{\gamma}}\hat{X}_{j\hat{\gamma}} \ . \tag{A.3}$$

For a single mode, namely $N = 1$, the diagonal elements of Γ are simply the two variances $\Gamma_{1,1} = 2(\Delta\hat{q}_1)^2_{\hat{\gamma}}$ and $\Gamma_{2,2} = 2(\Delta\hat{p}_1)^2_{\hat{\gamma}}$. The single constraint for the real-valued matrix to correspond to a physical state is given by the Heisenberg uncertainty relation, which can be concisely written as a semi-definite constraint as

$$\Gamma + i\Omega \geq 0. \tag{A.4}$$

A general Gaussian state of N modes is fully described by the vector of mean values and the covariance matrix corresponding to all modes. Gaussian states are ubiquitous in physical systems. For example, thermal states $\hat{\gamma}_\beta[\hat{H}] = \exp\Big(-\beta\hat{H}\Big) / \operatorname{tr}\left[\exp\Big(-\beta\hat{H}\Big)\right]$ are Gaussian whenever the Hamiltonian $\hat{H}$ is quadratic in the field operators, which again is a very common situation in many physical settings. In condensed matter physics and in quantum field theory, such a situation would be referred to as being non-interacting. Generally, every Gaussian state with full support [1] can be written in a form resembling thermal states of quadratic Hamiltonians, namely there exists a H such that

$$\hat{\gamma}[H] = \frac{1}{Z}\exp\left(-\tfrac{1}{2}(\hat{\mathbf{X}} - \bar{\mathbf{X}})^T H(\hat{\mathbf{X}} - \bar{\mathbf{X}})\right), \qquad H = \begin{pmatrix} H_{qq} & H_{qp} \\ H_{pq} & H_{pp} \end{pmatrix}, \tag{A.5}$$

where H is a real positive semi-definite $2N \times 2N$ matrix written in block form for clarity and

$$Z = \operatorname{tr}\left[\exp\left(-\tfrac{1}{2}(\hat{\mathbf{X}} - \bar{\mathbf{X}})^T H(\hat{\mathbf{X}} - \bar{\mathbf{X}})\right)\right] = \sqrt{\det((\Gamma + i\Omega)/2)} \tag{A.6}$$

is the normalization, which can be fully determined by the covariance matrix of the Gaussian state Γ. The relation between Γ and the matrix H appearing in the expression above is

$$H = 2i\Omega\ \operatorname{arcoth}(i\Gamma\Omega), \qquad \Gamma \ = i\Omega\coth(i\Omega H/2). \tag{A.7}$$

In turn, any generic quadratic (Hermitian) Hamiltonian can be written similarly as above, i.e., with H being a real positive-semi-definite $2N \times 2N$ matrix. The (Gaussian) unitary evolution corresponding to the time-independent quadratic Hamiltonian translates into the symplectic transformation acting on the covariance matrix, given by

$$G(t) = \exp(\Omega H t), \tag{A.8}$$

such that the evolved covariance matrix is $\Gamma(t) = G(t)\Gamma(0)G(t)^T$. A similar relation holds for the evolution with time-dependent Hamiltonians, see for example the discussion on the QTP primitives in section . Thus, in the framework of Gaussian states and operations one can work directly with just the mean vector and the covariance matrix, since they jointly contain all the information that characterizes the Gaussian state.

A.2 Details of the numerical simulations

Before diving in the detailed implementation of each primitive, let us provide some details on the lattice discretization scheme and write the discrete Hamiltonian explicitly.

---

[1] This means that the density matrix has no zero eigenvalue.

We define a lattice version of the phononic Hamiltonian, obtained by discretising the interval $[-L, L]$ into N pixels, each of size $\Delta z = 2L/N$ [41, 127]. This is particularly important to make numerical calculations, especially for the case of non-homogeneous external potentials. Fixing N, for $i = 1, \ldots, N+1$ the coordinates of the discretization lattice read $z_i = -L + 2L\frac{i-1}{N}$, and we define discretization pixels which are the closed intervals $p_i = [z_i, z_{i+1}]$ for $i = 1, \ldots, N$. We then introduce the discretized version of density and phase operators as the integration of the field operators via

$$\hat{\phi}_i^{(N)} = \frac{1}{\Delta z}\int_{p_i} \mathrm{d}z\ \phi(z), \qquad \delta\hat{\rho}_i^{(N)} = \frac{1}{\Delta z}\int_{p_i} \mathrm{d}z\ \delta\rho(z), \tag{A.9}$$

with $|p_i| = \Delta z = 2L/N$. These discretized operators yields a vector of canonical coordinates

$$\hat{\mathbf{X}} = \left(\delta\hat{\rho}_1^{(N)} \ldots \delta\hat{\rho}_N^{(N)}, \hat{\phi}_1^{(N)}, \ldots \hat{\phi}_N^{(N)}\right)^T, \tag{A.10}$$

satisfying (re-scaled) bosonic canonical commutation relations

$$[\hat{X}_j, \hat{X}_k] = i\Omega_{j,k}/\Delta z\ , \tag{A.11}$$

where Ω is defined in equation (A.2). As explained in reference [85], in the continuum limit $N \to \infty$, the right-hand side will yield a Dirac delta because $\Delta z \to 0$.

To discretise the model, we follow reference [41] and consider the geometric mean

$$\eta_i = \sqrt{\rho_0(z_i)\rho_0(z_{i+1})} \tag{A.12}$$

for $i = 1, \ldots, N$. The discretization of the effective model will be a quadratic operator in the discretised modes $\hat{\phi}_i^{(N)}$ and $\delta\hat{\rho}_i^{(N)}$. At the lowest order approximation, one obtains

$$\hat{H} \approx \Delta z \sum_{i=1}^{N-1} \frac{\hbar^2\eta_i}{2m}\left[\frac{\hat{\phi}_i^{(N)} - \hat{\phi}_{i+1}^{(N)}}{\Delta z}\right]^2 + \Delta z \sum_{i=1}^{N} \frac{g(z_i)}{2}\left(\delta\hat{\rho}_i^{(N)}\right)^2 =: \hat{H}_N. \tag{A.13}$$

Note that so far in the main text, we have suppressed for simplicity the possible spatial dependence of the coupling constant g, which is true for a homogeneous quasi-condensate and in general has little influence. In general g depends on the GP profile,

$$g(z) = \hbar\omega_\perp a_s(2 + 3a_s\rho_0(z))/(1 + 2a_s\rho_0(z))^{3/2} \tag{A.14}$$

where $\omega_\perp$ is the radial trapping frequency and a_s is the scattering length [22, 51] . This dependency on the spatial coordinate z has been included in our numerical simulations. From this, we obtain the matrix representation of the above Hamiltonian

$$H = \frac{1}{2}\cdot \hat{\mathbf{X}}^\top \left(H_{\rho\rho}[g, \Delta z] \oplus H_{\phi\phi}[\rho_0, \Delta z]\right) \hat{\mathbf{X}}\ , \tag{A.15}$$

$$H_{\rho\rho}[\Delta z] = \Delta z \cdot \mathrm{diag}\big(g(z_1), g(z_2), \cdots, g(z_{N_c})\big)\ , \tag{A.16}$$

$$\begin{aligned} H_{\phi\phi}[\rho_0, \Delta z] = \frac{\hbar^2}{m\Delta z} &\begin{pmatrix} \eta_1 & -\eta_1 & & & \\ -\eta_1 & \eta_1 + \eta_2 & -\eta_2 & & \\ & & \ddots & & \\ & & -\eta_{N-2} & \eta_{N-2} + \eta_{N-1} & -\eta_{N-1} \\ & & & -\eta_{N-1} & \eta_{N-1} \end{pmatrix} \\ &+ 2\hbar\ \mathrm{diag}\left(J(z_1)\eta(z_1), \ldots, J(z_N)\eta(z_N)\right), \end{aligned} \tag{A.17}$$

where we have used the functional notation $H_{\phi\phi}[\rho_0, \Delta z]$ to emphasize that these couplings depend on the mean-field density profile and the size of the pixels. We additionally added a small term $\propto J$ which is meant to regularize the zero-mode. This way, all computations are made with fully-supported Gaussian states so that numerical instabilities do not occur. Physically, it can be interpreted as adding a small mass term of the type $\hat{H}_J = hJ \int \mathrm{d}z \rho_0(z) \hat{\phi}(z)^2$ and we have checked that, as long as the coupling is chosen to be around $J \approx 0.01$ the dynamics is not affected in the times scales of 300 ms that we have in mind. See also section below for a more extended discussion.

We now porvide the details on the implementation on the merging primitive. Since the splitting primitive is a mere inversion of the mergin process, the technical details of one apply to the other as well.

A.2.1 Compression/expansion primitive

While performing the compression/expansion primitive, we assume the number of particles to be conserved and that the process ocurrs in a slow fashion (adiabatically). Under these assumptions, the Hamiltonian reads

$$\hat{H}(t) = \int_0^{L(t)} \mathrm{d}z \left[\frac{\hbar^2 \rho_0(z,t)}{2m} \left(\partial_z \hat{\phi} \right)^2 + \frac{g}{2} \delta\hat{\rho}^2 \right], \tag{A.18}$$

where the upper limit is time dependent.

We now describe how this process works in an infinitesimal stepwise fashion. The infinitesimal length change is

$$L \to L_\epsilon = (1+\epsilon)L, \tag{A.19}$$

and, correspondingly, a homogeneous GP profile ρ_0 changes to $\rho_0(\epsilon) = (1+\epsilon)^{-1}\rho_0$. Then, the Hamiltonian after the size change reads

$$\hat{H}_\epsilon = \int_0^{L_\epsilon} \mathrm{d}z \left[\frac{\hbar^2 \rho_0}{2m(1+\epsilon)} \left(\partial_z \hat{\phi} \right)^2 + \frac{g}{2} \delta\hat{\rho}^2 \right]. \tag{A.20}$$

Thus we observe that if a GP profiles changes slowly in length then the phonons are described by a similar Hamiltonian, only with modified couplings.

In the lattice model, we perform a similar procedure, but work fully in real space, this time with the Hamiltonian as a functional of both mean-field density and the small-distance cutoff. Starting from the discretized Hamiltonian $\hat{H}[\rho_0, \Delta z]$ of a single condensate with pixels, length $L = \Delta z$, and density ρ_0, we perform at each step a small length change $L \mapsto L_\epsilon = \Delta\zeta$, corresponding to a renormalization

$$H[\rho_0, \Delta z] \mapsto H[\rho_0(\epsilon), \Delta\zeta] = H_{\rho\rho}(1+\epsilon) \oplus H_{\phi\phi}/(1+\epsilon)^2 \ , \tag{A.21}$$

where we have used that $\rho_0(\epsilon) = \rho_0/(1+\epsilon)$ and $\Delta\zeta = (1+\epsilon)\Delta z$. Thus, we see that we are implementing a discretized version of the Hamiltonian (A.20).

Then, in order to complete the full length change ΔL in a time $t_{\mathrm{comp}} = N_t \Delta t$, where Δt is a small time interval and N_t is the total number of Trotter steps, at each discrete time step we perform an inifinitesimal length change, such that

$$\epsilon = \Delta L / N_t. \tag{A.22}$$

What we get is the state of the phonons after compressing by a finite amount. This assumes that the phonons always see a quasi-static background metric, that is their dynamical time-scales are much faster than how we compress the condensate. We observe that a sufficiently slow compression will not mix much between the modes and there will be thermal squeezing of the phonons. We also see that the energy will in fact change.

Let us now discuss a technical detail mentioned already in the main text. An implicit difference between the initial and final Hamiltonians of a compression/expansion step is that the continuous field theory should be defined in the time-dependent line $[0, L(t)]$. In principle, we can also make a change of the integration variable $z \mapsto \zeta = zL(0)/L(t)$, such that the theory is defined with a constant length. However, a subtle issue arises: the field commutation relations $[\delta\hat{\rho}(z), \hat{\phi}(z')] = \text{ß}\delta(z - z')$ depend on the coordinate z; thus a rescaling of the coordinate must be compensated by a corresponding rescaling of the density fluctuation field, in order to maintain the correct commutation relations. Then, calling $\lambda(t) = L(0)/L(t)$ we define the transformation

$$\begin{aligned} \zeta &= \lambda(t) z, \\ \delta\hat{\nu} &= \delta\hat{\rho}/\lambda(t), \end{aligned} \tag{A.23}$$

such that Hamiltonian (A.18) becomes

$$\hat{H} = \int_0^{L(0)} \mathrm{d}\zeta \left[\frac{\hbar^2(z,0)\lambda^2(t)}{2m} \left(\partial_\zeta \hat{\phi}\right)^2 + \frac{g}{2}\lambda(t)\delta\hat{\nu}^2 \right], \tag{A.24}$$

which effectively amounts to a renormalization of the line differential as

$$\mathrm{d}z \mapsto \mathrm{d}\zeta = \lambda(t)\,\mathrm{d}z, \tag{A.25}$$

at the same time ensuring that the fields satisfy the correct commutation relations:

$$[\delta\hat{\rho}(\zeta), \hat{\phi}(\zeta')] = i\delta(\zeta - \zeta')/\lambda(t) \;\Rightarrow\; [\delta\hat{\nu}(\zeta), \hat{\phi}(\zeta')] = i\delta(\zeta - \zeta'). \tag{A.26}$$

A.2.2 Merging/splitting primitive

The merging primitive involves two condensates A and B with lengths L_A and L_B and densities ρ_0^A and ρ_0^B. We have the following time dependent Hamiltonian

$$\hat{H}_{A-B}(0) = \hat{H}_{N^A}[\rho_0^A] + \hat{H}_{N^B}[\rho_0^B], \tag{A.27}$$

where our Hamiltonians are given by the lattice model in equation (A.13) and (keeping constant the small distance cutoff Δz) are functionals of the initial mean-field density profiles of the two condensates. Note that since we would like to couple the two systems, we require them to have a consistent momentum cutoff $(\Delta z)^A = (\Delta z)^B = \Delta z$ (so that waves traveling across quasi-condensates with same atom density in the simulation should not change in speed due to the different discretization), and consequently their number of pixels will be in the same proportion as their lengths, i.e.,

$$\frac{N^A}{L_A} = \frac{N^B}{L_B} = \Delta z. \tag{A.28}$$

The coupling matrix of the uncoupled Hamiltonian in equation (A.27) is given by

$$H_{\rho\rho,A|B} = H_{\rho\rho,A} \oplus H_{\rho\rho,B}, \qquad H_{\phi\phi,A|B} = H_{\phi\phi,A} \oplus H_{\phi\phi,B}\ . \tag{A.29}$$

To merge the condensates, an interaction Hamiltonian is switched on, so that the joint Hamiltonian as in equation (A.15) has a matrix representation given by

$$\begin{aligned} H_{\rho\rho,AB} &= H_{\rho\rho,A} \oplus H_{\rho\rho,B}, \\ H_{\phi\phi,AB} &= H_{\phi\phi,A} \oplus H_{\phi\phi,B} + \frac{t}{t_{\mathrm{merge}}} H_{\mathrm{int}}, \end{aligned} \tag{A.30}$$

where the interaction matrix is given by

$$(H_{\mathrm{int}})_{i,j} = \frac{\hbar^2}{2m\Delta z}\eta_{N^A}\left(\delta_{N^A,i}\delta_{N^A,j} + \delta_{N^A+1,i}\delta_{N^A+1,j} - \delta_{N^A,i}\delta_{N^A+1,j} - \delta_{N^A+1,i}\delta_{N^A,j}\right)\ . \tag{A.31}$$

with $\eta_{N^A} := \sqrt{\rho^A(N^A)\cdot\rho^B(1)}$. Note that this interaction contains also the local terms in the boundary region $[N^A, N^A+1]$. We hence see that the couplings during the merging are given by

$$H_{A-B}(t) = (1 - \tfrac{t}{t_{\mathrm{merge}}})H_{A|B} + \tfrac{t}{t_{\mathrm{merge}}}H_{AB}. \tag{A.32}$$

For the numerical implementation, we also discretize the time evolution so that we divide the $[0, t_{\mathrm{merge}}]$ time interval into N_t steps of duration $\Delta t = t_{\mathrm{merge}}/N_t$. Then, the symplectic evolution matrix reads

$$G_{\mathrm{merge}}(t_{\mathrm{merge}}) = \prod_{j=1}^{N_t} \exp\left(\Omega H_{A-B}(t_j)/\Delta z\right), \tag{A.33}$$

where $H_{A-B}(t) = H_{N^A} + H_{N^B} + (j/N_t)H_{\mathrm{int}}$.

Appendix B

Notes on local coupling

To include the influence of a barrier centered at $z = 0$ we follow reference [95], as we did in section . We consider a rectangular barrier that separates two adjacent condensates in a head-to-tail configuration, Consider a perturbation in the quasicondensate at wavenumber k. Given that the influence of the barrier spreads over a distance Δz_B, we write a wavefunction for such a qusiparticle and assume that it appreoaches the barrier from the left.

$$\eta_k(z) \propto \left\{ \begin{array}{ll} e^{ikz} + \tilde{r}_k e^{-ikz}, & z < -\Delta z_B \\ \tilde{t}_k e^{ikz}, & z > \Delta z_B. \end{array} \right. \tag{B.1}$$

The properties of transmission and reflection amplitudes ($\tilde{t}_k$ and $\tilde{r}_k$, respectively) are as follows

1. $|\tilde{t}_k|^2 + |\tilde{r}_k|^2 = 1$
2. $\tilde{t}_k$ and $\tilde{r}_k$ are orthogonal, i.e., $|\tilde{t}_k \pm \tilde{r}_k| = 1$
3. In general, $\tilde{t}_k - \tilde{r}_k \neq 1$, since the wave is a phonon in a quasicondensate and not a free particle. In other words, $|\tilde{t}_k - \tilde{r}_k| = 1$ but $\arg(\tilde{t}_k - \tilde{r}_k) \neq 0$

Assuming a very thin barrier , we can define even and odd eigenfunctions

$$\eta_{ck}(z) = \cos(kz + \text{sign}(z) \cdot \chi_{ck}) \tag{B.2}$$

$$\eta_{sk}(z) = \cos(kz + \text{sign}(z) \cdot \chi_{sk}), \tag{B.3}$$

where $\chi_{ck} = \frac{1}{2} \arg\left(\bar{t}_k + \bar{r}_k\right)$ and $\chi_{sk} = \frac{1}{2} \arg\left(\bar{t}_k - \bar{r}_k\right)$. Here $\text{sign}(z)$ is the sign function defined as

$$\text{sign}(z) = \begin{cases} -1, & \text{if } z < 0 \\ 0, & \text{if } z = 0 \\ 1, & \text{if } z > 0 \end{cases} \tag{B.4}$$

The arguments $\chi_{c,sk}$ can only be computed numerically. Instead of doing that, we can make some observations about these coefficients.

Since $\bar{t}_k \to 1$ for $k \to 0$, for very small k, we have $\arg(\bar{t}_k) \simeq 2\alpha k$ (linear dependence). As long as $1 - |\bar{t}_k| \ll 1$, we have $\chi_{ck} \simeq \chi_{sk} \simeq \alpha k$. On the regime of vey low tranmission, $|\bar{t}_k| \ll 1$, leads to $\chi_{ck} \simeq -\chi_{sk}$. Note that the low transmission regime can still be achieved in the phononic regime.

To compute the phase correlation function under the influence of the barrier, the term multiplying the expectation values of ϕ_k in equation (2.30) should be replaced by

$$\begin{aligned}(1-\cos(kz)) \to \frac{1}{2}\Big[&\cos^2(kz + \mathrm{sign}(z)\chi_{ck}) + \cos^2(kz' + \mathrm{sign}(z')\chi_{ck}) \\ &-2\cos(kz + \mathrm{sign}(z)\chi_{ck})\cos(kz' + \mathrm{sign}(z')\chi_{ck}) \\ &+\sin^2(kz + \mathrm{sign}(z)\chi_{sk}) + \sin^2(kz' + \mathrm{sign}(z')\chi_{sk}) \\ &-2\sin(kz + \mathrm{sign}(z)\chi_{sk})\sin(kz' + \mathrm{sign}(z')\chi_{sk})\Big]\end{aligned} \tag{B.5}$$

The analysis simplifies for low enough temperatures ($k \leq \lambda_T^{-1}$) where $|\tilde{t}_k| \simeq 1$ is a good approximation. We are thus in the regime where $\chi_{ck} \simeq \chi_{sk}$. Using the new basis functions, simple integration leads to

$$\langle e^{i\phi(z)-i\phi(z')}\rangle = \exp\left(-\frac{2}{\lambda_T}(|z-z'| + |\mathrm{sign}(z) - \mathrm{sign}(z')|\alpha)\right). \tag{B.6}$$

Now we analyze the role of α to get a better understanding of the barrier influence.

If we consider a barrier considerably larger than the healing length (in the experiment the barrier is approximately 1 µm, while the healing length is $l_h = 0.3\,\mu\mathrm{m}$), we can neglect the effect of the quantum pressure everywhere. Thus, we can apply the equation of phonon propagation in an homogeneous medium

$$k^2\eta_k = -\frac{\partial}{\partial z}\left[\tilde{c}^2(z)\frac{\partial}{\partial z}\eta_k\right], \tag{B.7}$$

where $\tilde{c}(z) = c(z)/c(\infty)$ is the ratio of the speeds of sound at point z and in the bulk, respectively.

Using the new variable

$$\tilde{z} = \int_0^z \mathrm{d}z' \frac{1}{\tilde{c}^2(z)}, \tag{B.8}$$

we can reduce equation (B.7) to a Schrödinger-like equation

$$-\frac{\partial}{\partial z}\phi_k + k^2\{1 - \tilde{c}^2(\tilde{z})\}\phi_k = k^2\phi_k. \tag{B.9}$$

Since we are interested in long wavelengths, the potential term can be replaced by a short-ranged potential $k^2 a\delta(\tilde{z})$, where

$$a = \int_{-\infty}^{\infty} \mathrm{d}\tilde{z}(1 - \tilde{c}^2(\tilde{z})) = \int_{-\infty}^{\infty} \mathrm{d}z\left(\frac{1}{\tilde{c}^2(z)} - 1\right), \tag{B.10}$$

then, the scattering problem can be solved.

We find the following expression for η_k

$$\phi_k = e^{ik\tilde{z}} + \frac{e^{ik|\tilde{z}|}}{2ik} k^2 a \eta_k(0), \tag{B.11}$$

where $\eta_k(0) = 1/(1+i\frac{ka}{2})$. Simplifying further, we obtain the expression for the wavefunction before and after the barrier

$$\eta_k(\tilde{z}) = \begin{cases} e^{ik\tilde{z}} - \frac{\frac{ika}{2} e^{-ik\tilde{z}}}{1+i\frac{ka}{2}} \\ \frac{e^{-ik\tilde{z}}}{1+i\frac{ka}{2}} \end{cases} \tag{B.12}$$

The argument of the complex transmission amplitude is a sum of two contributions: the denominator defined by the wavefunction at the barrier position and the exponential dependent on $\tilde{z}$.

In total, we obtain $\tilde{t} = e^{2i\alpha k}$, where α is given by

$$\alpha = \frac{1}{4} \int_{-\infty}^{\infty} \mathrm{d}z \left[\frac{1}{\tilde{c}^2(z)} - 1 \right] > 0. \tag{B.13}$$

A positive α corresponds to a Wigner delay of phonons propagating through a barrier. Figure B.1 illustrates how the phase correlation behaves in the presence of the barrier. In reality, the jump is not discontinuous, but has a finite width due to the variation of the speed of sound.

It is interesting to observe that for higher temperatures, the jump in the correlation function becomes smaller. This is due to the fact that the phase shifht introduced by the barrier happens at a point where the correlations are already lowe compared to condensates at lower temperatures. The correlation will decrease after the barrier, however, since it is lower bounded at 0, the decrease is smaller.

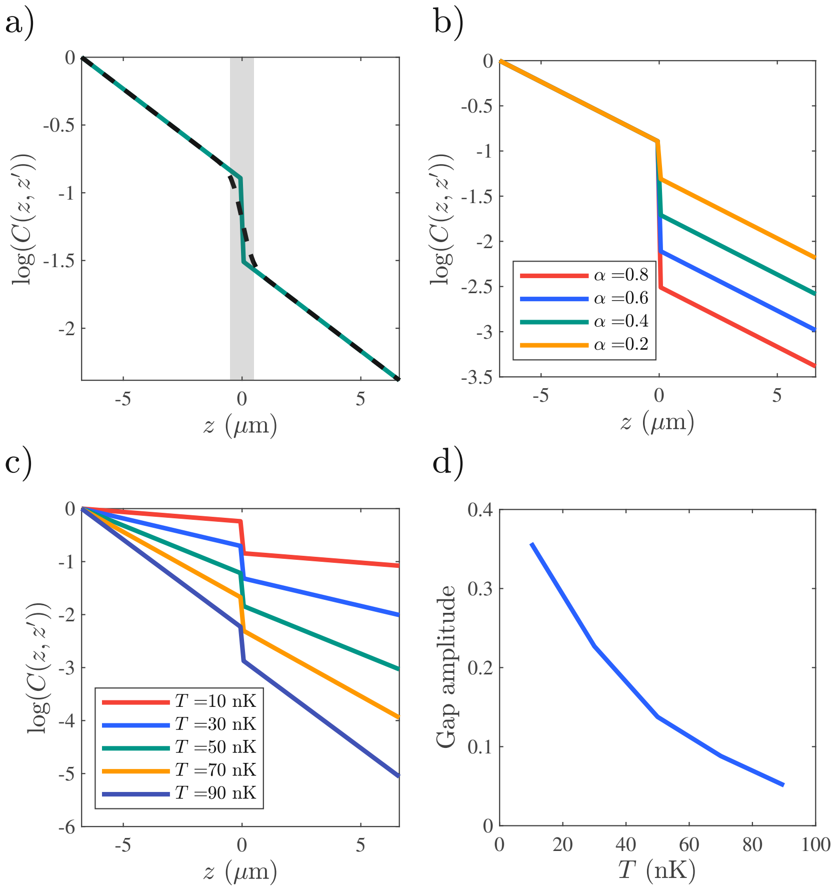

Figure B.1: **Effects of the barrier in the phase correlation function:** a) The green line shows the curve given by the analytical solution (B.6) together with the effective smooth decay (dashed black line) due to the change of the speed of sound around the barrier. The gray shade indicates the position of a 1 µm wide barrier. b) Different phase correlation functions of a condensate at $T = 40\,\mathrm{nK}$ for several barrier strengths, characterized by the parameter α. c) Behaviour of the phase correlation function of condensates at different temperatures when a barrier with $\alpha = 0.3$ is used. d) Height of the jump seen in c) for the different temperatures. The gap decreases as the temperature increases. A confidence level of 95% was used to compute the errors.

Appendix C

Distribution of the local phase variance

To apply the local thermometry method described in 5.1, we need to compute the phase variance within the region where we want to measure the temperature. Although some theoretical calculations can be done on this subject, here it will suffice to briefly introduce the main equations and focus on numerical and experimental results.

We start by noting that the phase variance is computed over many different experimental realizations. Let us then consider N phase measured profiles, each one denoted by $\theta_i(z)$, where $i = 1, ..., N$. The variance over a region R that spans between points z_1 and z_M reads

$$\sigma_R^2 = \langle \frac{1}{M} \sum_{j=1}^{M} (\theta_i(z_j) - \{\theta_i(z_1, z_M)\})^2 \rangle, \tag{C.1}$$

where the angled brackets denote the average over the N realizations, the curly brackets denote the mean value of the phase over the points z_j, which belong to the region of space defined by z_1 and z_M. In more detail, we have

$$\begin{aligned}
\{\theta_i(z_1, z_M)\} &= \frac{1}{M} \sum_j \theta_i(z_j) \\
&= \frac{1}{M} \sum_j \frac{1}{\sqrt{2\rho_0}} \sum_k -i f_k^- b_k^i e^{ikz_j} + \text{H.c.} \\
&= \frac{1}{L} \int_{z_1}^{z_M} \mathrm{d}z \frac{1}{\sqrt{2\rho_0}} \sum_k -i f_k^- b_k^i e^{ikz_j} + \text{H.c.} \\
&= \frac{1}{\sqrt{2\rho_0}} \sum_k -i f_k^- b_k^i \left\{ \frac{1}{L} \int_{z_1}^{z_M} \mathrm{d}z e^{ikz} \right\} + \text{H.c.} \\
&= \frac{1}{\sqrt{2\rho_0}} \sum_k -i f_k^- b_k^i I_m + \text{H.c.},
\end{aligned} \tag{C.2}$$

where I_m is a compact notation for the term in curly brackets on the fourth line of equation (C.2) and $L = z_M - z_1$ is the region's length.

We can now use this expression in equation (C.1) and write everything as a function of the basis functions and the creation/anihilation operators

$$\begin{aligned}\sigma_R^2 &= \frac{1}{N}\sum_i \frac{1}{M}\sum_j (\theta_i(z_j) - \{\theta_i(z_j)\})^2 \\ &= \frac{1}{2\rho_0}\frac{1}{N}\sum_i \frac{1}{M}\sum_j \left[(\sum_k -i f_k^- b_k^i e^{ikz_j} + \text{H.c.}) - (\sum_p -i f_b^- b_p^i I_p + \text{H.c.}) \right]^2 .\end{aligned} \tag{C.3}$$

If the state is considered to be thermal, the operators b_k can be sampled as a Gaussian complex random variable that depends on the Bose-Einstein distribution [128]. In the context of this work, we compare the values of σ_R^2 obtained experimentally to the ones computed using thermal states generated thorugh the Ornstein-Uhlenbeck process [110]. This way, we can consider the effects of the imaging system on the calculation of σ_R^2. Figure C.1 shows the distribution of σ_R^2 for two distinct temperatures. The distributions are exponential and the mean values computed for numerical and experimental data are in agreement.

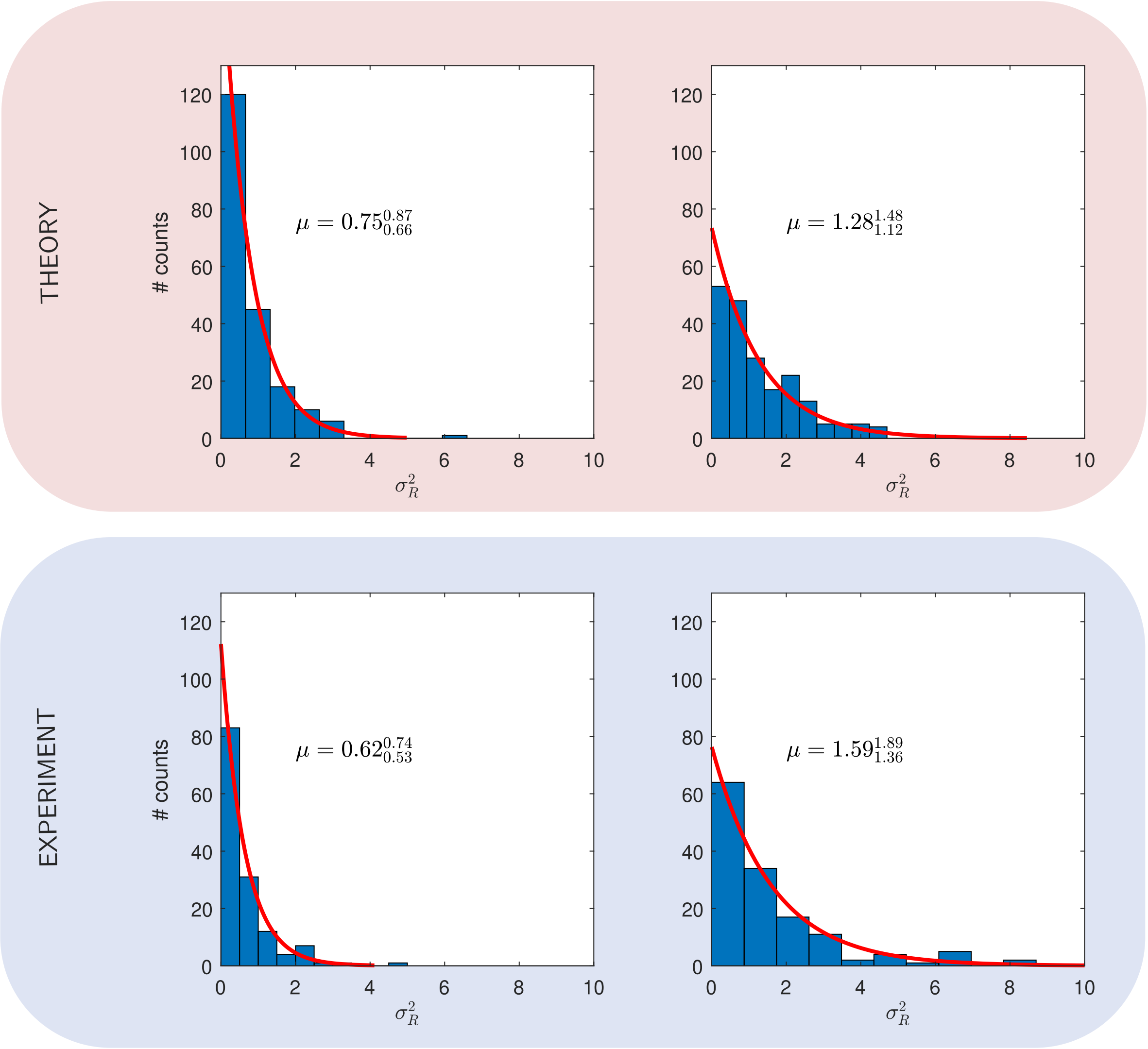

Figure C.1: **Local phase distribution:** The histograms show the phase variance distributions for two different temperatures, $\sim 50\,\mathrm{nK}$ for the left column and $\sim 100\,\mathrm{nK}$ for the right column. A region $12\,\mu\mathrm{m}$ was chosen. The red lines show the fitted exponential distributions with the respective mean values indicated by μ. The errors were computed with a confidence level of $95\,\%$.

Appendix D

Full box basis

Here we present a detailed calculation of how to project the modes of each individual adjacent box in the basis of the full, merged box. We work under the Classical Fields Approximation [79]. The density fluctuations and phase fields of a thermal box of length L can be written as

$$\delta\rho(z) = \frac{1}{\sqrt{L}} \sum_p \left(\frac{\epsilon_p}{E_p}\right)^{-\frac{1}{2}} \cos\left(\frac{\pi p}{L} z\right) (b_p + b_p^\dagger) \tag{D.1}$$

$$\phi(z) = \frac{-i}{\sqrt{L}} \sum_p \left(\frac{\epsilon_p}{E_p}\right)^{\frac{1}{2}} \cos\left(\frac{\pi p}{L} z\right) (b_p - b_p^\dagger) \tag{D.2}$$

In the initial state, we have two uncoupled thermal boxes of lengths $L_1 = L_2 = L/2$, each one at a specific temperature T_1 and T_2. From now onwards, we will assume $T_1 < T_2$. We can write the density fluctuations of each box using the previous equations

$$\delta\rho_1(z) = \frac{1}{\sqrt{L}} \sum_p \left(\frac{\epsilon_p}{E_p}\right)^{-\frac{1}{2}} \cos\left(\frac{2\pi p}{L} z\right) (b_p + b_p^\dagger), \tag{D.3}$$

$$\delta\rho_2(z) = \frac{1}{\sqrt{L}} \sum_q \left(\frac{\epsilon_q}{E_q}\right)^{-\frac{1}{2}} \cos\left(\frac{2\pi q}{L} \left(z - \frac{L}{2}\right)\right) (b_q + b_p^\dagger), \tag{D.4}$$

where the energies ϵ_j and E_j are the same as defined in 2.1.2, and the $b_{p,q}$ are the anihilation operators of the different modes for the different boxes. For the sake of simplicity and clarity, we will always associate the index p with the Box 1 and the index q with Box 2. Notice the extra term $L/2$ subtracted in the argument of the co-sine used to decompose Box2. This factor accounts for the fact that the modes of this box are oscillating in the second half of the full box of lengh L.

After merging the boxes by quickly removing the barrier, we project the joint state of the two uncorrelated boxes in the basis of the full box with length L. We keep in mind that the end goal is the computation of the phase correlation functions. To achieve that, we are interested in calculating the quasiparticle correlations $\langle b_m^\dagger b_m \rangle$ and $\langle b_m b_m \rangle$ given by [46]

$$\langle b_m^\dagger b_m \rangle = \frac{1}{2} \int \int \mathrm{d}z \, \mathrm{d}z' \left[\frac{f_m^-(z) \bar{f}_n^-(z') \langle \delta\rho(z) \delta\rho(z') \rangle}{n_0} + \frac{f_m^+(z) \bar{f}_n^+(z') \langle \phi(z) \phi(z') \rangle}{n_0^{-1}} \right], \tag{D.5}$$

$$\langle b_m b_m \rangle = \frac{1}{2} \int \int \mathrm{d}z \, \mathrm{d}z' \left[\frac{\bar{f}_m^-(z) \bar{f}_n^-(z') \langle \delta\rho(z) \delta\rho(z') \rangle}{n_0} - \frac{\bar{f}_m^+(z) \bar{f}_n^+(z') \langle \phi(z) \phi(z') \rangle}{n_0^{-1}} \right]. \tag{D.6}$$

Since the space we are integrating over is divided in two distinct regions, we can break the integrals from equations (D.5) and (D.6) in four parts

$$\begin{aligned} \langle b_m^\dagger b_m \rangle = \int_0^L \int_0^L \mathrm{d}z \, \mathrm{d}z' (\ldots) = & \\ \int_0^{\frac{L}{2}} \int_0^{\frac{L}{2}} \mathrm{d}z \, \mathrm{d}z' (\ldots) + \int_0^{\frac{L}{2}} \int_{\frac{L}{2}}^{L} \mathrm{d}z \, \mathrm{d}z' (\ldots) + & \\ \int_{\frac{L}{2}}^{L} \int_0^{\frac{L}{2}} \mathrm{d}z \, \mathrm{d}z' (\ldots) + \int_{\frac{L}{2}}^{L} \int_{\frac{L}{2}}^{L} \mathrm{d}z \, \mathrm{d}z' (\ldots). & \end{aligned} \tag{D.7}$$

Since the two initial boxes hold no correlations between them, the second and third terms correlating the these boxes vanish, remaining the first and last terms of the sum. These are the quantities that need to be computed next. Since for the specific case of the square box the basis functions are co-sines. the expressions for the non-vanishing integrals in equation (D.7) simplify significantly. We will show the calculations explicitly for the part of the integral regarding the density. The result is the same for the phase field, apart from the multiplication by n_0.

The first integral on the second line of equation (D.7) reads

$$\begin{aligned} & \int_0^{\frac{L}{2}} \int_0^{\frac{L}{2}} \mathrm{d}z \, \mathrm{d}z' \frac{1}{\sqrt{L}} \left(\frac{\epsilon_m}{E_m} \right)^{-\frac{1}{2}} \cos\left(\frac{\pi m}{L} z \right) \cdot \frac{1}{\sqrt{L}} \left(\frac{\epsilon_n}{E_n} \right)^{-\frac{1}{2}} \cos\left(\frac{\pi n}{L} z \right) \\ & \qquad \sum_{p,p'} \left[\sqrt{\frac{2}{L}} \left(\frac{\epsilon_m}{E_m} \right)^{-\frac{1}{2}} \cos\left(\frac{2\pi p}{L} z \right) \sqrt{\frac{2}{L}} \left(\frac{\epsilon_p'}{E_p'} \right)^{-\frac{1}{2}} \cos\left(\frac{2\pi p'}{L} z \right) \right] \langle b_p^\dagger b_p' \rangle \\ & \qquad + \text{phase term} \end{aligned} \tag{D.8}$$

The sum running the mode indexes of the small box reduces to a sum over a single index due to the modes' orthogonality. We can thus write a more simplified expression, separating the two spactial coordinates in two different integrals. We have

$$\begin{aligned} & \frac{2}{\sqrt{L^2}} \sum_p \int_0^{\frac{L}{2}} \sqrt{\frac{E_m E_p}{\epsilon_m \epsilon_p}} \int_0^{\frac{L}{2}} \mathrm{d}z \cos\left(\frac{\pi m}{L} z \right) \cos\left(\frac{2\pi p}{L} z \right) \cdot \\ & \qquad \sqrt{\frac{E_n E_p}{\epsilon_n \epsilon_p}} \int_0^{\frac{L}{2}} \int_0^{\frac{L}{2}} \mathrm{d}z' \cos\left(\frac{\pi n}{L} z' \right) \cos\left(\frac{2\pi p}{L} z' \right) \langle b_p^\dagger b_p \rangle. \end{aligned} \tag{D.9}$$

It is now convenient to calculate each integral by performing the calculation for even and odd modes separately. For even modes, the calculation becomes a simple integration over the basis of a box of size $L/2$ as in the beginning. As such, the first integral simply yields the value of $\delta_{m/2,p}$, with the same happening for the second integral for the z' coordinate with index n.

For the odd modes, we simplify the integral by using the trignometric identity

$$\cos(\alpha)\cos(\beta) = \frac{\cos(\alpha-\beta)+\cos(\alpha+\beta)}{2}. \tag{D.10}$$

Each of the integrals in equation (D.9) can, then, be calculated as follows

$$\begin{aligned}
&\int_0^{\frac{L}{2}}\int_0^{\frac{L}{2}} \mathrm{d}z \cos\left(\frac{\pi m}{L}z\right)\cos\left(\frac{2\pi p}{L}z\right) = \\
&\qquad = \int_0^{\frac{L}{2}} \mathrm{d}z \frac{\cos\left(\frac{\pi}{L}(m-2p)z\right)+\cos\left(\frac{\pi}{L}(m+2p)z\right)}{2} \\
&\qquad = \frac{1}{2}\left[\frac{L}{\pi(m-2p)}\sin\left(\frac{\pi}{2}(m-2p)\right)+\frac{L}{\pi(m+2p)}\sin\left(\frac{\pi}{2}(m+2p)\right)\right] \\
&\qquad = I_{m,p}.
\end{aligned} \tag{D.11}$$

The quantity $I_{m,p}$ is merely a way of condensing the notation for the integral's result. The integral corresponding to the phase term can be computed in a similar way.

The only integral left to compute is the last term in equation (D.7), accounting for the contributions of Box 2. Notice that this integral is similar to the one we just computed, the only difference being the shift of $L/2$ in space. Since the integral is computing the same quantity in Box 2 as the same integral we computed for Box 1, it can be solved in the same way, yielding the same result but using the Bogoliubov operators for the second box. Therefore, we can write the complete expressions for the mode decomposition in the full box

$$\langle b_m^\dagger b_n\rangle = \frac{1}{L^2}\sum_{j=p,q}\sum_{j=1}^{\infty}\left(\frac{E_j}{\epsilon_j}\sqrt{\frac{E_mE_n}{\epsilon_m\epsilon_n}}+\frac{\epsilon_j}{E_j}\sqrt{\frac{\epsilon_m\epsilon_n}{E_mE_n}}\right)I_{m,j}I_{n,j}\langle b_j^\dagger b_j\rangle \tag{D.12}$$

$$\langle b_m^\dagger b_n\rangle = \frac{1}{L^2}\sum_{j=p,q}\sum_{j=1}^{\infty}\left(\frac{E_j}{\epsilon_j}\sqrt{\frac{E_mE_n}{\epsilon_m\epsilon_n}}-\frac{\epsilon_j}{E_j}\sqrt{\frac{\epsilon_m\epsilon_n}{E_mE_n}}\right)I_{m,j}I_{n,j}\langle b_j^\dagger b_j\rangle \tag{D.13}$$

Bibliography

[1] Ted Jacobson. Thermodynamics of spacetime: the einstein equation of state. *Physical Review Letters*, 75(7):1260–1263, 1995.

[2] Paul Skrzypczyk, Anthony J. Short, and Sandu Popescu. Work extraction and thermodynamics for individual quantum systems. *Nature Communications*, 5(1):4185, 2014.

[3] Ronnie Kosloff. Quantum thermodynamics: A dynamical viewpoint. *Entropy*, 15(6):2100–2128, 2013.

[4] Jacob D. Bekenstein. Black holes and entropy. *Physical Review D*, 7(8):2333–2346, 1973.

[5] Markus Heusler. The four laws of black hole physics. *Black Hole Uniqueness Theorems*, 170:102–121, 2010.

[6] John Goold, Marcus Huber, Arnau Riera, Lídia del Rio, and Paul Skrzypczyk. The role of quantum information in thermodynamics-a topical review. *Journal of Physics A: Mathematical and Theoretical*, 49(14):143001, 2016.

[7] Max Karl Ernst Ludwig Planck. Zur Theorie des Gesetzes der Energieverteilung im Normalspectrum. *Verhandl. Dtsc. Phys. Ges.*, 2:237, 1900.

[8] A. Einstein. Über einen die erzeugung und verwandlung des lichtes betreffenden heuristischen gesichtspunkt. *Annalen der Physik*, 322(6):132–148, 1905.

[9] Jörg Schmiedmayer. *One-Dimensional Atomic Superfluids as a Model System for Quantum Thermodynamics*, pages 823–851. Springer International Publishing, Cham, 2018.

[10] L. Boltzmann. Weitere studien über das wärmegleichgewicht unter gasmolekülen. *Sitzungsberichte Akademie der Wissenschaften*, pages 275–370, 1872.

[11] I. A. Sadovskyy M. V. Suslov V. M. Vinokur G. B. Lesovik, A. V. Lebedev. H-theorem in quantum physics. *Scientific Reports*, 6:32815, 2016.

[12] G. Lindblad. On the generators of quantum dynamical semigroups. *Communications in Mathematical Physics*, 48(2):119–130, 1976.

[13] Timothy C. Berkelbach and Michael Thoss. Special topic on dynamics of open quantum systems. *The Journal of Chemical Physics*, 152(2):020401, 2020.

[14] Susana F. Huelga Angel Rivas. *Open Quantum Systems*. Oxford Univeristy Press, 2012.

[15] Marco Pezzutto, Mauro Paternostro, and Yasser Omar. Implications of non-markovian quantum dynamics for the landauer bound. *New Journal of Physics*, 18(12):123018, 2016.

[16] M. Perarnau-Llobet, H. Wilming, A. Riera, R. Gallego, and J. Eisert. Strong coupling corrections in quantum thermodynamics. *Phys. Rev. Lett.*, 120:120602, Mar 2018.

[17] M. H. Anderson, J. R. Ensher, M. R. Matthews, C. E. Wieman, and E. A. Cornell. Observation of bose-einstein condensation in a dilute atomic vapor. *Science*, 269(5221):198–201, 1995.

[18] Immanuel Bloch, Jean Dalibard, and Wilhelm Zwerger. Many-body physics with ultracold gases. *Reviews of Modern Physics*, 80(3):885–964, 2008.

[19] Immanuel Bloch, Jean Dalibard, and Sylvain Nascimbène. Quantum simulations with ultracold quantum gases. *Nature Physics*, 8(4):267–276, 2012.

[20] D. Adu Smith, M. Gring, T. Langen, M. Kuhnert, B. Rauer, R. Geiger, T. Kitagawa, I. Mazets, E. Demler, and J. Schmiedmayer. Prethermalization revealed by the relaxation dynamics of full distribution functions. *New Journal of Physics*, 15:0–31, 2013.

[21] M. Gring, M. Kuhnert, T. Langen, T. Kitagawa, B. Rauer, M. Schreitl, I. Mazets, D. Adu Smith, E. Demler, and J. Schmiedmayer. Relaxation and prethermalization in an isolated quantum system. *Science*, 337(6100):1318–1322, 2012.

[22] Bernhard Rauer, Sebastian Erne, Thomas Schweigler, Federica Cataldini, Mohammadamin Tajik, and Jörg Schmiedmayer. Recurrences in an isolated quantum many-body system. *Science*, 360(6386):307–310, 2018.

[23] Thomas Schweigler, Marek Gluza, Mohammadamin Tajik, Spyros Sotiriadis, Federica Cataldini, Si-Cong Ji, Frederik S. Møller, João Sabino, Bernhard Rauer, Jens Eisert, and Jörg Schmiedmayer. Decay and recurrence of non-gaussian correlations in a quantum many-body system. *Nature Physics*, 17(5):559–563, 2021.

[24] Marek Gluza, Thomas Schweigler, Mohammadamin Tajik, João Sabino, Federica Cataldini, Frederik Skovbo Møller, Si-Cong Ji, Bernhard Rauer, Jörg Schmiedmayer, Jens Eisert, and Spyros Sotiriadis. Mechanisms for the emergence of gaussian correlations. *SciPost Physics*, 12(3):113, 2022.

[25] David Gelbwaser-Klimovsky, Wolfgang Niedenzu, and Gershon Kurizki. Thermodynamics of Quantum Systems Under Dynamical Control. *Advances in Atomic, Molecular and Optical Physics*, 64:329–407, 2015.

[26] Marco Pezzutto, Mauro Paternostro, and Yasser Omar. An out-of-equilibrium non-markovian quantum heat engine. *Quantum Science and Technology*, 4(2):025002, 2019.

[27] Wolfgang Niedenzu, Igor Mazets, Gershon Kurizki, and Fred Jendrzejewski. Quantized refrigerator for an atomic cloud. *Quantum*, 3(nil):155, 2019.

[28] D. Gelbwaser-Klimovsky and G. Kurizki. Heat-machine control by quantum-state preparation: From quantum engines to refrigerators. *Physical Review E*, 90(2):022102, 2014.

[29] Marek Gluza, João Sabino, Nelly H.Y. Ng, Giuseppe Vitagliano, Marco Pezzutto, Yasser Omar, Igor Mazets, Marcus Huber, Jörg Schmiedmayer, and Jens Eisert. Quantum field thermal machines. *PRX Quantum*, 2:030310, Jul 2021.

[30] Vladan Vuletić Jakob Reichel. *Atom Chips*. []. Wiley-VCH Verlag GmbH & Co. KGaA, 2011.

[31] Thierry Giamarchi. *Quantum Physics in One Dimension*. Oxford Univeristy Press, 2004.

[32] N. D. Mermin and H. Wagner. Absence of ferromagnetism or antiferromagnetism in one- or two-dimensional isotropic heisenberg models. *Physical Review Letters*, 17(22):1133–1136, 1966.

[33] P. C. Hohenberg. Existence of long-range order in one and two dimensions. *Physical Review*, 158(2):383–386, 1967.

[34] C. J. Pethick and H. Smith. *Bose-Einstein Condensation in Dilute Gases*. Bose-Einstein Condensation in Dilute Gases. Cambridge University Press, 2008.

[35] A. D. Steck. Rubidium 87 d line data.

[36] Jean-Sébastien Caux and Jorn Mossel. Remarks on the notion of quantum integrability. *Journal of Statistical Mechanics: Theory and Experiment*, 2011(02):P02023, 2011.

[37] Toshiya Kinoshita, Trevor Wenger, and David S. Weiss. A quantum Newton's cradle. *Nature*, 440(7086):900–903, 2006.

[38] Elliott H Lieb and Werner Liniger. Exact Analysis of an Interacting Bose Gas. I. The General Solution and the Ground State. *Phys. Rev.*, 130(4):1605–1616, may 1963.

[39] Elliott H Lieb. Exact Analysis of an Interacting Bose Gas. II. The Excitation Spectrum. *Phys. Rev.*, 130(4):1616–1624, may 1963.

[40] Bernhard Rauer. Non-equilibrium dynamics beyond dephasing : Recurrences and loss induced cooling in one-dimensional Bose gases. (September 2018):127, 2018.

[41] Christophe Mora and Yvan Castin. Extension of bogoliubov theory to quasicondensates. *Phys. Rev. A*, 67:053615, May 2003.

[42] Sin-itiro Tomonaga. Remarks on Bloch's Method of Sound Waves applied to Many-Fermion Problems. *Progress of Theoretical Physics*, 5(4):544–569, 1950.

[43] J M Luttinger. An Exactly Soluble Model of a Many-Fermion System. *Journal of Mathematical Physics*, 4(9):1154–1162, 1963.

[44] N. N. Bogoliubov, V. V. Tolmachev, D. V. Shirkov, and R. Bruce Lindsay. A new method in the theory of superconductivity. *Physics Today*, 13(5):44–44, 1960.

[45] Nicholas K. Whitlock and Isabelle Bouchoule. Relative phase fluctuations of two coupled one-dimensional condensates. *Physical Review A*, 68(5):053609, 2003.

[46] Sebastian Erne. *Far-From-Equilibrium Quantum Many-Body Systems From Universal Dynamics to Statistical Mechanics*. PhD thesis, 2018.

[47] T Langen, T Schweigler, E Demler, and J Schmiedmayer. Double light-cone dynamics establish thermal states in integrable 1d bose gases. *New Journal of Physics*, 20(2):023034, 2018.

[48] Kerson Huang. *Statistical Mechanics*. 1991.

[49] Michael Gring. *Prethermalization in an Isolated Many Body System*. PhD thesis, TU Wien, 2012.

[50] A. Görlitz, J. M. Vogels, A. E. Leanhardt, C. Raman, T. L. Gustavson, J. R. Abo-Shaeer, A. P. Chikkatur, S. Gupta, S. Inouye, T. Rosenband, and W. Ketterle. Realization of bose-einstein condensates in lower dimensions. *Physical Review Letters*, 87(13):130402, 2001.

[51] L. Salasnich, A. Parola, and L. Reatto. Effective wave equations for the dynamics of cigar-shaped and disk-shaped bose condensates. *Physical Review A*, 65(4):043614, 2002.

[52] F Gerbier. Quasi-1D Bose-Einstein condensates in the dimensional crossover regime. *Europhysics Letters (EPL)*, 66(6):771–777, jun 2004.

[53] M. Olshanii. Atomic scattering in the presence of an external confinement and a gas of impenetrable bosons. *Physical Review Letters*, 81(5):938–941, 1998.

[54] Elmar Haller, Manfred J. Mark, Russell Hart, Johann G. Danzl, Lukas Reichsöllner, Vladimir Melezhik, Peter Schmelcher, and Hanns-Christoph Nägerl. Confinement-induced resonances in low-dimensional quantum systems. *Phys. Rev. Lett.*, 104:153203, Apr 2010.

[55] J. Armijo, T. Jacqmin, K. Kheruntsyan, and I. Bouchoule. Mapping out the quasi-condensate transition through the dimensional crossover from one to three dimensions. *Phys. Rev. A*, 83:021605, Feb 2011.

[56] Luca Salasnich. Generalized nonpolynomial schrödinger equations for matter waves under anisotropic transverse confinement. *Journal of Physics A: Mathematical and Theoretical*, 42(33):335205, jul 2009.

[57] P Pitaevskii and Sandro Stringari. *Bose-Einstein Condensation*. 2003.

[58] L. Salasnich, A. Parola, and L. Reatto. Dimensional reduction in bose-einstein-condensed alkali-metal vapors. *Phys. Rev. A*, 69:045601, Apr 2004.

[59] Tim Langen. *Non-equilibrium dynamics of one-dimensional Bose gases.* PhD thesis, TU Wien, 2013.

[60] Maximilian Kuhnert. *Thermalization and Prethermalization in an ultracold Bose Gas.* PhD thesis, TU Wien, 2013.

[61] Martin Göbel. *Low-Dimensional Traps for Bose-Fermi Mixtures.* PhD thesis, TU Wien, 2008.

[62] Y. Castin, J. Dalibard, and C. Cohen-Tannoudji. *Laser Cooling and Trapping of Neutral Atoms*, pages 173–201. Bose-Einstein Condensation. Cambridge University Press, 1995.

[63] Mohammadamin Tajik. Arbitrary One-Dimensional Optical Dipole Potentials on an Atom Chip, 2017.

[64] J. Dalibard and C. Cohen-Tannoudji. Laser cooling below the doppler limit by polarization gradients: Simple theoretical models. *Journal of the Optical Society of America B*, 6(11):2023, 1989.

[65] K. B. Davis, M. O. Mewes, and W. Ketterle. An analytical model for evaporative cooling of atoms. *Applied Physics B Laser and Optics*, 60(2-3):155–159, 1995.

[66] O. J. Luiten, M. W. Reynolds, and J. T. M. Walraven. Kinetic theory of the evaporative cooling of a trapped gas. *Physical Review A*, 53(1):381–389, 1996.

[67] Thorsten Schumm. *Bose-Einstein condensates in magnetic double well potentials.* PhD thesis, Universit¨at Heidelberg, 2005.

[68] I. Lesanovsky, T. Schumm, S. Hofferberth, L. M. Andersson, P. Krüger, and J. Schmiedmayer. Adiabatic radio-frequency potentials for the coherent manipulation of matter waves. *Physical Review A*, 73(3):033619, 2006.

[69] C. Figl J.-B. Trebbia C. Aussibal H. Nguyen D. Mailly I. Bouchoule C. I. Westbrook A. Aspect T. Schumm, J. Estève. Atom chips in the real world: the effects of wire corrugation. *Eur. Phys. J. D*, 32:171–180, 2005.

[70] J. Estève, C. Aussibal, T. Schumm, C. Figl, D. Mailly, I. Bouchoule, C. I. Westbrook, and A. Aspect. Role of wire imperfections in micromagnetic traps for atoms. *Physical Review A*, 70(4):043629, 2004.

[71] T. Schumm, S. Hofferberth, L. M. Andersson, S. Wildermuth, S. Groth, I. Bar-Joseph, J. Schmiedmayer, and P. Krüger. Matter-wave interferometry in a double well on an atom chip. *Nature Physics*, 1(1):57–62, 2005.

[72] Rudolf Grimm, Matthias Weidemüller, and Yurii B. Ovchinnikov. *Optical Dipole Traps for Neutral Atoms*, pages 95–170. Advances In Atomic, Molecular, and Optical Physics. Elsevier, 2000.

[73] Mohammadamin Tajik, Bernhard Rauer, Thomas Schweigler, Federica Cataldini, João Sabino, Frederik S. Møller, Si-Cong Ji, Igor E. Mazets, and Jörg Schmiedmayer. Designing arbitrary one-dimensional potentials on an atom chip. *Optics Express*, 27(23):33474, 2019.

[74] W. Rohringer, D. Fischer, F. Steiner, I. E. Mazets, J. Schmiedmayer, and M. Trupke. Non-equilibrium scale invariance and shortcuts to adiabaticity in a one-dimensional bose gas. *Scientific Reports*, 5(1):9820, 2015.

[75] Martino Calzavara-Jörg Schmiedmayer Tommaso Calarco Andreas Kugi Andreas Deutschmann-Olek, Mohammadamin Tajik. Iterative shaping of optical potentials for one-dimensional bose-einstein condensates. *arXiv:2208.00706v1*, 2022.

[76] D.M. Stamper-Kurn W. Ketterle, D.S. Durfee. Making, probing and understanding bose-einstein condensates. *arXiv:cond-mat/9904034*, 1999.

[77] Yuri D. van Nieuwkerk, Jörg Schmiedmayer, and Fabian H. L. Essler. Projective phase measurements in one-dimensional Bose gases. *SciPost Phys.*, 5:046, 2018.

[78] David A. Smith, Simon Aigner, Sebastian Hofferberth, Michael Gring, Mauritz Andersson, Stefan Wildermuth, Peter Krüger, Stephan Schneider, Thorsten Schumm, and Jörg Schmiedmayer. Absorption imaging of ultracold atoms on atom chips. *Optics Express*, 19(9):8471, 2011.

[79] Thomas Schweigler. Correlations and dynamics of tunnel-coupled one-dimensional Bose gases. 2019.

[80] D. S. Petrov V. Gritsev S. Manz S. Hofferberth T. Schumm Demler E A. Imambevok, I. E. Mazets and J Schmiedmayer. Density ripples in expanding low-dimensional gases as a probe of correlations. pages 1–14, 2009.

[81] S. Manz, R. Bücker, T. Betz, Ch Koller, S. Hofferberth, I. E. Mazets, A. Imambekov, E. Demler, A. Perrin, J. Schmiedmayer, and T. Schumm. Two-point density correlations of quasicondensates in free expansion. *Physical Review A - Atomic, Molecular, and Optical Physics*, 81(3):1–4, 2010.

[82] W Rohringer. *Dynamics of One-Dimensional Bose Gases in Time-Dependent Traps.* PhD thesis, TU Wien, 2014.

[83] S. Hofferberth, I. Lesanovsky, B. Fischer, T. Schumm, and J. Schmiedmayer. Non-equilibrium coherence dynamics in one-dimensional bose gases. *Nature*, 449(7160):324–327, 2007.

[84] Tim Langen, Sebastian Erne, Remi Geiger, Bernhard Rauer, Thomas Schweigler, Maximilian Kuhnert, Wolfgang Rohringer, Igor E. Mazets, Thomas Gasenzer, and Jörg Schmiedmayer. Experimental observation of a generalized gibbs ensemble. *Science*, 348(6231):207–211, 2015.

[85] M. Gluza, T. Schweigler, B. Rauer, C. Krumnow, J. Schmiedmayer, and J. Eisert. Quantum read-out for cold atomic quantum simulators. *Communications Physics*, 3(1):12, 2020.

[86] M. Klimesh. Inequalities that collectively completely characterize the catalytic majorization relation. *arXiv:0709.3680*, 2007.

[87] N H Y Ng, L Mančinska, C Cirstoiu, J Eisert, and S Wehner. Limits to catalysis in quantum thermodynamics. *New Journal of Physics*, 17(8):085004, 2015.

[88] S Turgut. Catalytic transformations for bipartite pure states. *Journal of Physics A: Mathematical and Theoretical*, 40(40):12185–12212, sep 2007.

[89] M. Lewenstein and L. You. Quantum phase diffusion of a bose-einstein condensate. *Phys. Rev. Lett.*, 77:3489–3493, Oct 1996.

[90] Juha Javanainen and Martin Wilkens. Phase and phase diffusion of a split bose-einstein condensate. *Phys. Rev. Lett.*, 78:4675–4678, Jun 1997.

[91] A. J. Leggett and F. Sols. Comment on “phase and phase diffusion of a split bose-einstein condensate”. *Phys. Rev. Lett.*, 81:1344–1344, Aug 1998.

[92] Juha Javanainen and Martin Wilkens. Javanainen and wilkens reply:. *Phys. Rev. Lett.*, 81:1345–1345, Aug 1998.

[93] Marine Pigneur, Tarik Berrada, Marie Bonneau, Thorsten Schumm, Eugene Demler, and Jörg Schmiedmayer. Relaxation to a phase-locked equilibrium state in a one-dimensional bosonic josephson junction. *Phys. Rev. Lett.*, 120:173601, Apr 2018.

[94] Marine Pigneur and Jörg Schmiedmayer. Analytical pendulum model for a bosonic josephson junction. *Phys. Rev. A*, 98:063632, Dec 2018.

[95] Yu. Kagan, D. L. Kovrizhin, and L. A. Maksimov. Anomalous tunneling of phonon excitations between two bose-einstein condensates. *Phys. Rev. Lett.*, 90:130402, Apr 2003.

[96] Vladimir Gritsev, Anatoli Polkovnikov, and Eugene Demler. Linear response theory for a pair of coupled one-dimensional condensates of interacting atoms. *Phys. Rev. B*, 75:174511, May 2007.

[97] C. Menotti, J. R. Anglin, J. I. Cirac, and P. Zoller. Dynamic splitting of a bose-einstein condensate. *Phys. Rev. A*, 63:023601, Jan 2001.

[98] I. Carusotto, R. Balbinot, A. Fabbri, and A. Recati. Density correlations and analog dynamical casimir emission of bogoliubov phonons in modulated atomic bose-einstein condensates. *The European Physical Journal D*, 56(3):391–404, 2009.

[99] Marios H. Michael, Jörg Schmiedmayer, and Eugene Demler. From the moving piston to the dynamical casimir effect: Explorations with shaken condensates. *Phys. Rev. A*, 99:053615, May 2019.

[100] Thomas Schweigler, Valentin Kasper, Sebastian Erne, Igor Mazets, Bernhard Rauer, Federica Cataldini, Tim Langen, Thomas Gasenzer, Jürgen Berges, and Jörg Schmiedmayer. Experimental characterization of a quantum many-body system via higher-order correlations. *Nature*, 545(7654):323–326, 2017.

[101] Eugene P. Wigner. Lower limit for the energy derivative of the scattering phase shift. *Physical Review*, 98(1):145–147, 1955.

[102] Katharina Schrom. Optimal Control Strategies for Quantum Field Thermal Machines, 2021.

[103] Scaling behavior of interactions in a modular quantum system and the existence of local temperature. *Europhysics Letters*, 65(5):613–619, 2004.

[104] Michael Hartmann, Günter Mahler, and Ortwin Hess. Existence of temperature on the nanoscale. *Physical Review Letters*, 93(8):1–4, 2004.

[105] Michael Hartmann. Minimal length scales for the existence of local temperature. *Contemporary Physics*, 47(2):89–102, 2006.

[106] Arnau Riera Martin Kliesch. *Properties of Thermal Quantum States: Locality of Temperature, Decay of Correlations, and More*, pages 481–502. Springer International Publishing, Cham, 2018.

[107] Thomas M. Stace Antonella De Pasquale. *Quantum Thermometry*, pages 503–527. Springer International Publishing, Cham, 2018.

[108] M. Kliesch, C. Gogolin, M. J. Kastoryano, A. Riera, and J. Eisert. Locality of Temperature. *Physical Review X*, 4(3):1–19, 2014.

[109] Spyros Sotiriadis Bernhard Rauer Thomas Schweigler Federica Cataldini João Sabino Frederik Møller Philipp Schüttelkopf Si-Cong Ji Dries Sels Eugene Demler Jörg Schmiedmayer Mohammadamin Tajik, Ivan Kukuljan. Experimental verification of the area law of mutual information in quantum field theory. *arXiv:2206.10563*, 2022.

[110] H.-P. Stimming, N. J. Mauser, J. Schmiedmayer, and I. E. Mazets. Fluctuations and stochastic processes in one-dimensional many-body quantum systems. *Physical Review Letters*, 105(1):015301, 2010.

[111] S. Dettmer, D. Hellweg, P. Ryytty, J. J. Arlt, W. Ertmer, K. Sengstock, D. S. Petrov, G. V. Shlyapnikov, H. Kreutzmann, L. Santos, and M. Lewenstein. Observation of phase fluctuations in elongated bose-einstein condensates. *Phys. Rev. Lett.*, 87:160406, Oct 2001.

[112] Marine Pigneur, Tarik Berrada, Marie Bonneau, Thorsten Schumm, Eugene Demler, and Jörg Schmiedmayer. Relaxation to a phase-locked equilibrium state in a one-dimensional bosonic josephson junction. *Phys. Rev. Lett.*, 120:173601, Apr 2018.

[113] Henry Poincaret. Sur le problème des trois corps et les équations de la dynamique, par h. poincaré. *Acta Mathematica*, 13:1–270, 1890.

[114] P. Bocchieri and A. Loinger. Quantum recurrence theorem. *Phys. Rev.*, 107:337–338, Jul 1957.

[115] Ian C. Percival. Almost Periodicity and the Quantal H Theorem. *Journal of Mathematical Physics*, 2(2):235–239, March 1961.

[116] T. Hogg and B. A. Huberman. Recurrence phenomena in quantum dynamics. *Phys. Rev. Lett.*, 48:711–714, Mar 1982.

[117] Bruce Ron Carter, Mancini. *Op Amps For Everyone.* 2002.

[118] Marcos Rigol, Vanja Dunjko, Vladimir Yurovsky, and Maxim Olshanii. Relaxation in a completely integrable many-body quantum system: An ab initio study of the dynamics of the highly excited states of 1d lattice hard-core bosons. *Phys. Rev. Lett.*, 98:050405, Feb 2007.

[119] C. L. Kane and Matthew P.A. Fisher. Transport in a One-Channel Luttinger Liquid. *Physical Review*, 68(8), 1992.

[120] Charles Kane, Leon Balents, and Matthew P.A. Fisher. Coulomb interactions and mesoscopic effects in carbon nanotubes. *Physical Review Letters*, 79(25):5086–5089, 1997.

[121] C. L. Kane and Matthew P.A. Fisher. Transmission through barriers and resonant tunneling in an interacting one-dimensional electron gas. *Physical Review B*, 46(23):15233–15262, 1992.

[122] Abhik Kumar Saha and Romain Dubessy. Dynamical phase diagram of a one-dimensional bose gas in a box with a tunable weak link: From bose-josephson oscillations to shock waves. *Phys. Rev. A*, 104:023316, Aug 2021.

[123] A Tononi, F Toigo, S Wimberger, A Cappellaro, and L Salasnich. Dephasing–rephasing dynamics of one-dimensional tunneling quasicondensates. *New Journal of Physics*, 22(7):073020, jul 2020.

[124] Lorenzo Magrini, Philipp Rosenzweig, Constanze Bach, Andreas Deutschmann-Olek, Sebastian G. Hofer, Sungkun Hong, Nikolai Kiesel, Andreas Kugi, and Markus Aspelmeyer. Real-time optimal quantum control of mechanical motion at room temperature. *Nature*, 595:373–377, 2021.

[125] C. Weedbrook, S. Pirandola, R. Garcia-Patron, N. J. Cerf, T. C. Ralph, J. H. Shapiro, and S. Lloyd. Gaussian quantum information. *Rev. Mod. Phys.*, 84:621, 2012.

[126] J. Eisert and M. B. Plenio. Introduction to the basics of entanglement theory in continuous-variable systems. *Int. J. Quant. Inf.*, 1:479, 2003.

[127] A. Carmichael and Juha Javanainen. Mean-field stationary state of a Bose gas at a Feshbach resonance. *Phys. Rev. A*, 77:043616, 2008.

[128] P.B. Blakie†, A.S. Bradley†, M.J. Davis, R.J. Ballagh, and C.W. Gardiner. Dynamics and statistical mechanics of ultra-cold bose gases using c-field techniques. *Advances in Physics*, 57(5):363–455, 2008.